Atomic Structures and Chemical States of Dopants in Ga_2O_3

蔡, 宇華

Atomic Structures and Chemical States of Dopants in Ga_2O_3

TSAI YU-HUA

Kyushu University

2024.06.25

Vita

September 19th, 1994, born in Taichung, Taiwan

2013-2017 Bachelor course, Department of Material Science and Engineering, National Chiao Tung University, Taiwan

2017-2019 Master course, Department of Material Science and Engineering, National Chiao Tung University, Taiwan

2021-present Doctor course at Department of Applied Chemistry, Graduate School of Engineering, Kyushu University

List of Publications

1. Photoelectron Holographic Study for Atomic Site Occupancy for Si Dopants in Si-Doped κ-Ga_2O_3(001)
   Yuhua Tsai, Yusuke Hashimoto, ZeXu Sun, Takuya Moriki, Takashi Tadamura, Takahiro Nagata, Piero Mazzolini, Antonella Parisini, Matteo Bosi, Luca Seravalli, Tomohiro Matsushita, and Yoshiyuki Yamashita, *Nano Letters* **24**, 3978 (2024).
2. Atomic position and the chemical state of an active Sn dopant for Sn-doped β-Ga_2O_3(001)
   Yuhua Tsai, Masaaki Kobata, Tatsuo Fukuda, Hajime Tanida, Toru Kobayashi, and Yoshiyuki Yamashita, *Applied Physics Letters* **124**, 112105 (2024).
3. X-ray Absorption Fine Structural Study of Atomic Structures and Chemical States of Dopants in 4H-SiC(0001)
   Yuhua Tsai, Jingmin Tang, and Yoshiyuki Yamashita, *ACS Applied Electronic Materials* **5**, 3843 (2023).

Table of Contents

Vita i
List of Publications i
Table of Contents ii
Chapter 1 Introduction 1
1.1 General introduction for Ga_2O_3 1
1.2 Polymorphs of Ga_2O_3 3
1.3 Dopants for Ga_2O_3 10
1.4 Current issues of dopants for Ga_2O_3 13
1.5 The purpose of the present thesis 14
1.6 Content Summary 15
References 16
Chapter 2 Experimental 21
2.1 Sample preparation for Sn-doped β-Ga_2O_3 and Si-doped κ-Ga_2O_3 21
2.2 Characterization Methods 23
2.2.1 Secondary Ion Mass Spectrometry (SIMS) 23
2.2.2 Hall effect measurements 26
2.2.3 Photoelectron spectroscopy (PES) 31
2.2.4 Photoelectron holography (PEH) 37
2.2.5 X-ray absorption 40
2.2.5.1 X-ray absorption fine structure (XAFS) 44
2.2.5.2 X-ray absorption near edge structure (XANES) 47
2.2.5.3 Extended X-ray absorption fine structure (EXAFS) 47
References 49
Chapter 3 Atomic position and the chemical state of an active Sn dopant for Sn-doped β-Ga_2O_3(001) 53
3.1 Introduction 53
3.2 Experimental 53
3.3 Results 54
3.4 Discussion 71
3.5 Conclusion 72
References 73
Chapter 4 Photoelectron Holographic Study for Atomic Site Occupancy for Si Dopants in Si-Doped κ-Ga_2O_3(001) 76

4.1 Introduction.....76
4.2 Experimental.....77
4.3 Results.....78
4.4 Discussion.....92
4.5 Conclusion.....99
References.....100
Chapter 5 Conclusions and outlook.....103
5.1 Summary of the important conclusions.....103
5.2 Outlook of the thesis.....104
Acknowledgement.....105

Chapter 1 Introduction

1.1 General introduction for Ga_2O_3

Gallium oxide (Ga_2O_3) has attracted a significant amount of interest due to its excellent properties, such as a large bandgap of 4.5–5.3 eV (depending on the crystal polymorphs), high thermal stability, and high breakdown electric field.[1-22] Ga_2O_3 has six crystal polymorphs, α, β, γ, δ, ε, and κ.[8-10,13,23-26] Among these polymorphs, β-Ga_2O_3 is the most thermodynamically and chemically stable.[8-10,13,23-26] The high-quality β-Ga_2O_3 film can be homoepitaxially grown on the β-Ga_2O_3 substrate.[6,11,13,18]

β-Ga_2O_3 exhibits a theoretical breakdown electric field (E_{cr}) of up to 8.73 MV/cm according to the following equation (1.1),[10,22,27]

$$E_{cr} = a(E_g)^n \tag{1.1}$$

where the coefficient a is 1.73×10^5, the index n is 2.5, and E_g is the bandgap energy of β-Ga_2O_3. The high breakdown electric field may be applied to ultra-high-power devices (>1 MW) such as electrical power transmission, hybrid propulsion systems, and military applications.[1-3,5-12,15,16,22]

The high Baliga's figure of merit (BFOM) for β-Ga_2O_3 indicates that a high breakdown voltage can be achieved with a low on-resistance.[1,2,4-6,11,15,22,28] The BFOM formula is described as,[1,2,4-6,11,15,22,28]

$$BFOM = \varepsilon \cdot \mu_n \cdot {E_{cr}}^3 \tag{1.2}$$

where ε, μ_n, and E_{cr} are the dielectric constant, carrier mobility, and breakdown electric field, respectively. Figure 1.1 shows the on-resistance as a function of breakdown voltage for wide bandgap (WBG) and ultra-wide bandgap (UWBG) semiconductors.

As shown in Fig. 1.1, β-Ga_2O_3 shows a significantly larger breakdown voltage than 4H-SiC and GaN. A higher BFOM offers both higher speed (reducing switching losses) and lower on-resistance (reducing conduction losses).[5,15,16,22,28] As a result, β-Ga_2O_3-based devices are widely studied for the application of high-power devises.[1-3,5-11]

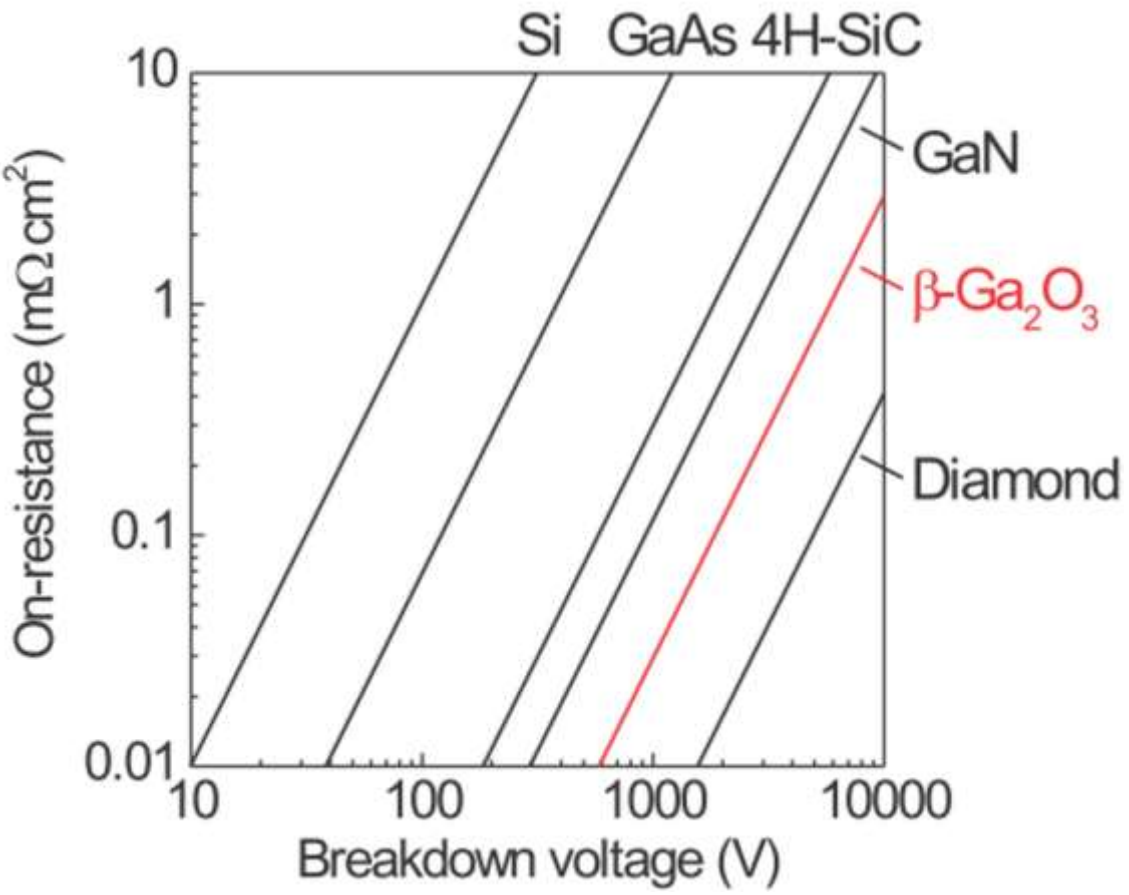

Figure 1.1. BFOM of general WBG and UWBG semiconductors.[16]

The other polymorphs of Ga_2O_3 (α, γ, δ, ε, and κ), on the other hand, are thermodynamically metastable phases. Among the metastable polymorphs, α-Ga_2O_3 has the widest bandgap of 5.3 eV,[3,4,6,8,10,13,14] which is suitable for Schottky barrier diodes with low on-resistance and high breakdown voltage.[20,21,29,30] For γ-Ga_2O_3, Mn-doped γ-Ga_2O_3 exhibits ferromagnetism at room temperature, which is applied to spintronic devices.[31-33] In the case of δ-Ga_2O_3, there has been little investigation because of the difficulty of preparing thin films.[9,20,23] For the ε phase Ga_2O_3 polymorph, it is an excellent candidate for devices with high-mobility two-dimensional electron gas (2DEG) systems and non-volatile memory applications due to its spontaneous polarization property.[1,2,8,9,29] In the case of κ-Ga_2O_3, it was mistakenly regarded as orthorhombic ε-Ga_2O_3.[1,7-10] This was due to their similar XRD patterns.[9,34] κ-Ga_2O_3 is expected to show larger spontaneous polarization along the c-axis compared to ε-Ga_2O_3.[9,19] In addition, κ-Ga_2O_3 shows ferroelectric property among the polymorphs of Ga_2O_3. Thus, κ-Ga_2O_3 is expected to be applied to the devices with 2DEG systems.[34]

Ga_2O_3 has great potential in the field of high-power devices, as described

above. For high-power device applications, Ga_2O_3-based devices are expected to be better than SiC- and GaN-based devices.[1-3,5-12,15,16,22] The electronic properties of Si, 4H-SiC, GaN, and β-Ga_2O_3 are summarized in Table 1.1.

	Si	4H-SiC	GaN	β-Ga_2O_3
Energy bandgap (eV)	1.1	3.3	3.4	4.8
Carrier mobility ($cm^2/V·s$)	1400	1000	1200	200
Breakdown electric field (MV/cm)	0.3	2.5	3.3	8.7
Normalized BFOM	1	340	870	2953
Dielectric constant	11.8	9.7	9.0	10.0

Table 1.1. Electronic properties of β-Ga_2O_3 and the other semiconductors.[1-3,35]

1.2 Polymorphs of Ga_2O_3

As described above, Ga_2O_3 has six crystal polymorphs; corundum structure (α-Ga_2O_3), monoclinic structure (β-Ga_2O_3), cubic defect spinel structure (γ-Ga_2O_3), cubic bixbyite structure (δ-Ga_2O_3), hexagonal structure (ε-Ga_2O_3), and orthorhombic structure (κ-Ga_2O_3). Among them, the most thermodynamically stable is β-Ga_2O_3.[8-10,13,23-26] All other metastable phases can be converted to β-Ga_2O_3 at high temperatures (500–700 °C),[7,9,11,17,23,26] as shown in Fig. 1.2.

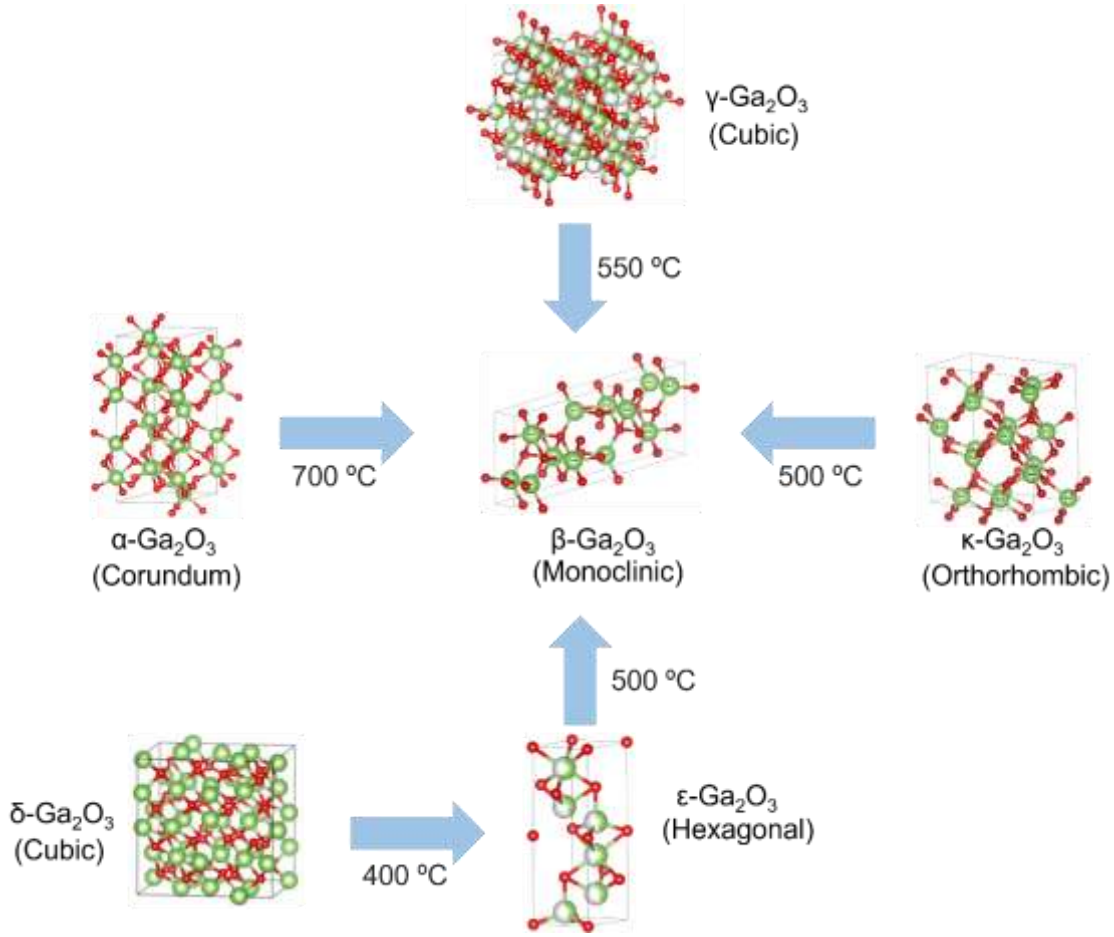

Figure 1.2. Structures of six polymorphs and their phase transition relationships in Ga_2O_3.[9,26,36] Green, and red balls represent Ga and O atoms.

For α-Ga_2O_3, the lattice parameters are a = 4.98 Å and c = 13.43 Å, α = γ = 90°, β = 120°, which is shown in Fig. 1.3.[8-10,26] The space group for α-Ga_2O_3 is $R\bar{3}c$, where the Ga atoms occupy Wyckoff positions 12c (0, 0, z), while the oxygen atoms occupy Wyckoff positions 18e (x, 0, 1/4).[37] The unit cell of α-Ga_2O_3 contains one inequivalent octahedral Ga site.[10,14,17,38] This structure is based on the O ions in the hexagonal closet packing array, with Ga^{3+} cations occupying 2/3 of the octahedral sites.[10,38] Since the α-phase Ga_2O_3 has a similar structure and low lattice mismatch to sapphire, high-quality α-Ga_2O_3 can be prepared on sapphire substrates by using heteroepitaxial methods.[9,11,26]

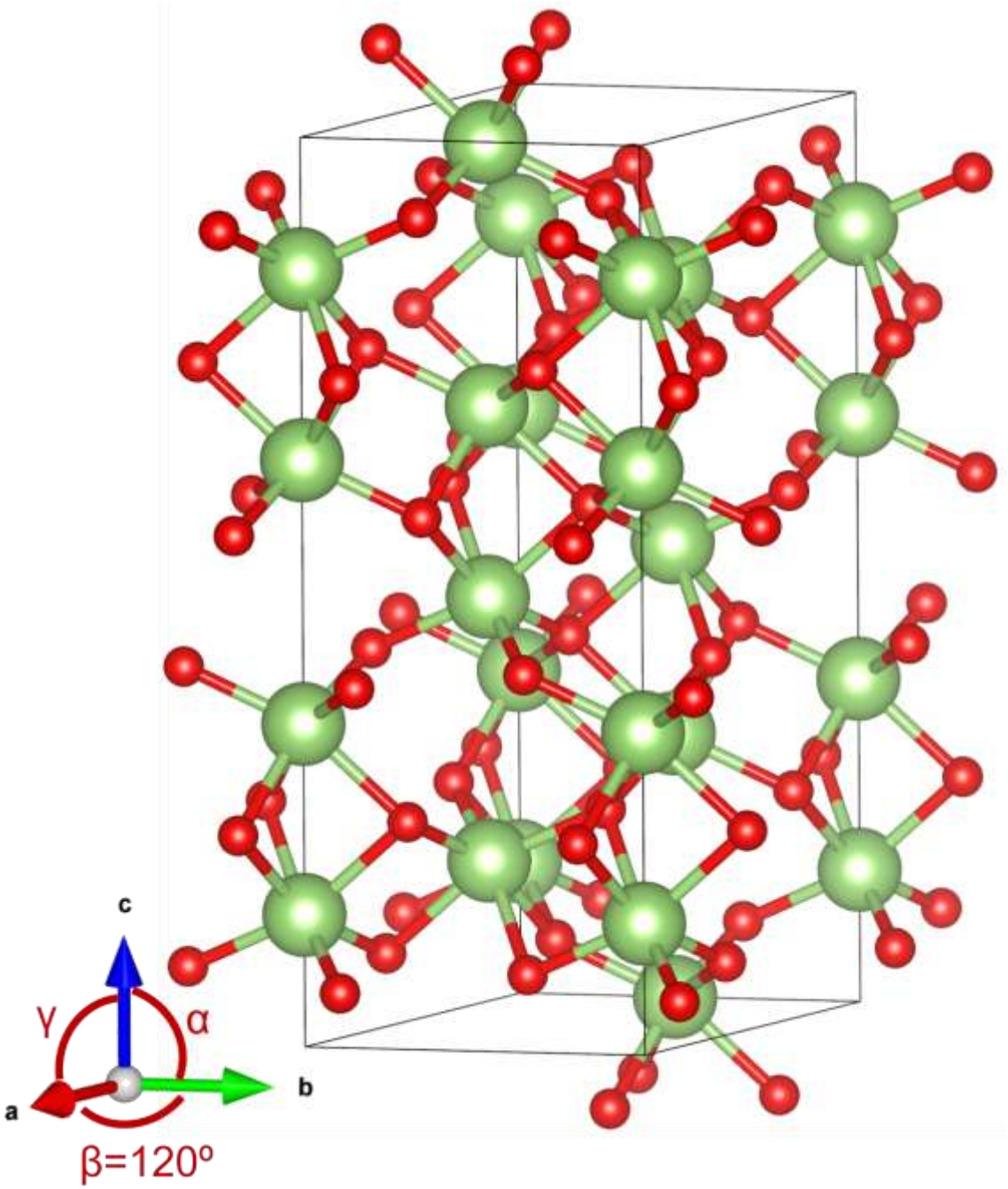

Figure 1.3. The unit cell of α-Ga_2O_3 crystal structures. Green, and red balls represent Ga and O atoms.

β-Ga_2O_3 exhibits a monoclinic crystal structure as shown in Fig. 1.4. The lattice parameters are a = 12.23 Å, b = 3.04 Å, c = 5.80 Å, and β = 103.8°.[8-11] The b-axis is the two-fold rotational axis in the β-Ga_2O_3 unit cell. The unit cell of β-Ga_2O_3 shows the C2/m space group. All of the atoms in β-Ga_2O_3 are located at 4i (x, 0, z) Wyckoff

positions.[37,39] Half of the Ga atoms are in the tetrahedral site (Ga1), and the other half are in the octahedral site (Ga2).[7,10,26] The O anions occupy two distorted trigonal sites (O1 and O3) and one distorted tetrahedral site (O2).[10,26] These structural characteristics lead to low symmetry, resulting in significant anisotropy in physical, optical, and electronic properties.[1,2,7,10,11] For instance, the (-201), (100), (010), and (100) planes exhibit different thermal conductivity.[1,11] These properties were experimentally observed.[9-11]

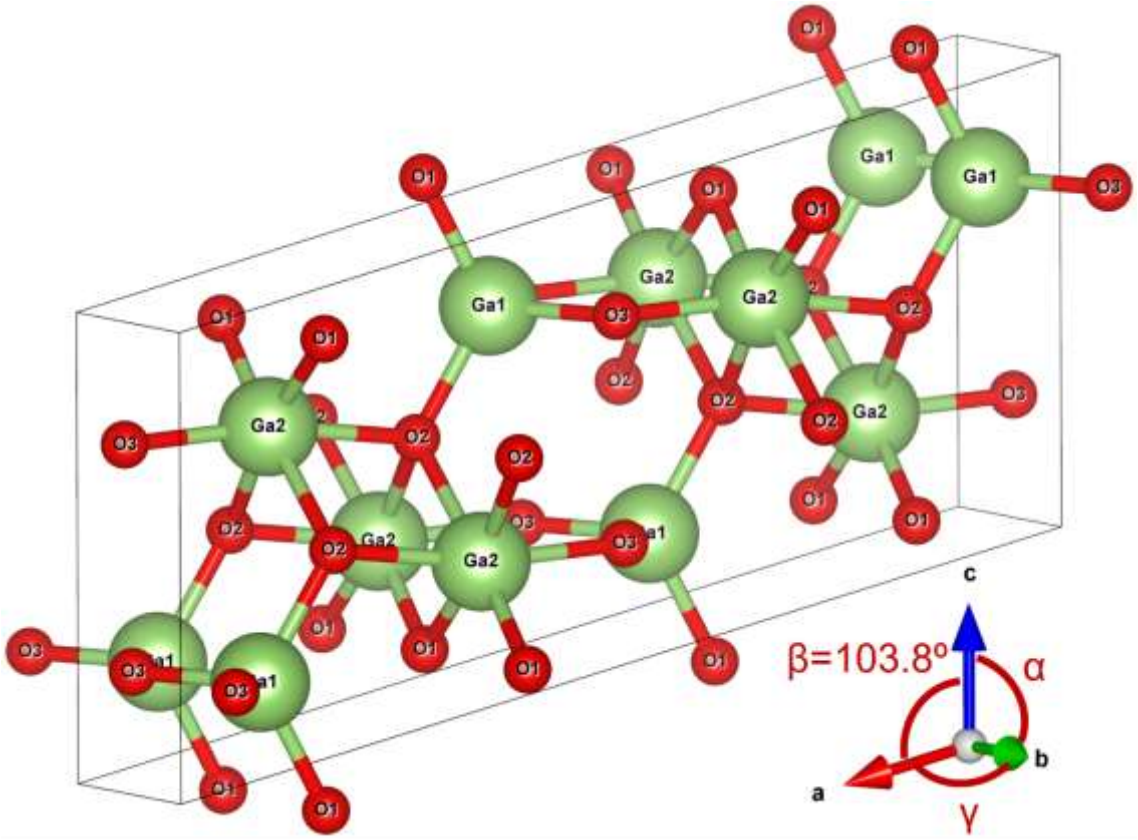

Figure 1.4. The unit cell of monoclinic β-Ga_2O_3 crystal structure. Green, and red balls represent Ga and O atoms.

Figure 1.5 shows the unit cell of γ-Ga_2O_3. Among the six polymorphs, γ-Ga_2O_3 has a cation-deficient structure ($MgAl_2O_4$ cubic spinel type).[40] The lattice parameters are a = b = c = 8.24 Å, α = β = γ = 90°.[8,9,41] The space group of γ-Ga_2O_3 is $Fd\bar{3}m$, where Ga atoms are distributed over four Wyckoff positions; the tetrahedral sites 8a (1/8, 1/8, 1/8), 48f (x, 1/8, 1/8) and the octahedral sites 16c (0, 0, 0), 16d (1/2, 1/2, 1/2). The oxygen atoms occupy Wyckoff positions 32e (x, x, x).[40,41] The γ-phase Ga_2O_3 is composed of octahedral and tetrahedral coordinated Ga sites, and the ratio of octahedral

to tetrahedral sites is 2:1.[10,41]

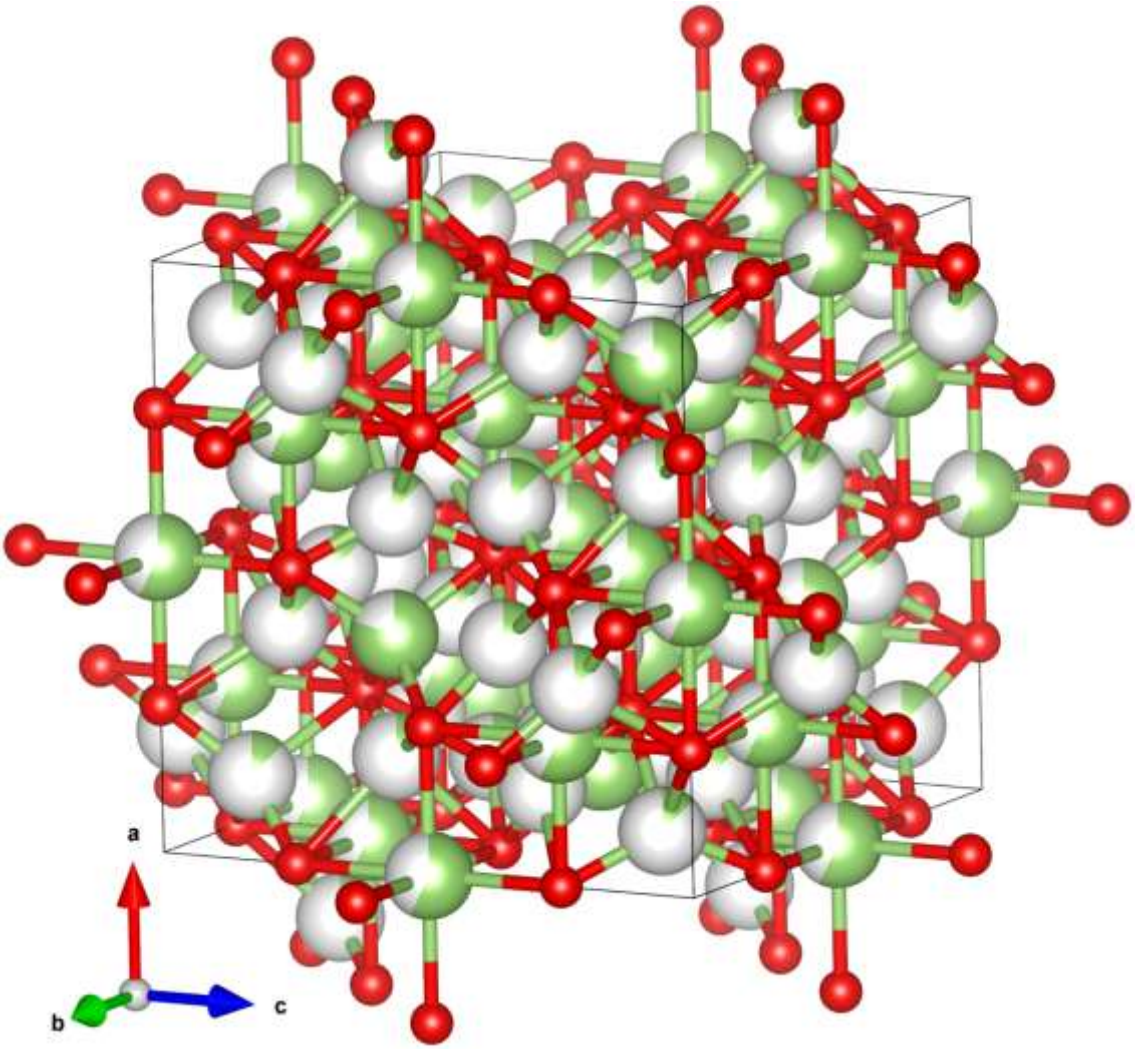

Figure 1.5. The unit cell of γ-Ga_2O_3 crystal structures. Green, and red balls represent Ga and O atoms.

Figure 1.6 shows the unit cell of δ-Ga_2O_3. The δ-Ga_2O_3 phase is a metastable phase with a body-centered cubic structure, and the space group is $Ia\bar{3}$.[8,9,36] The Ga atoms occupy Wyckoff positions 8b (1/4, 1/4, 1/4), 24d (x, 0, 1/4) whereas the oxygen atoms occupy Wyckoff positions 48e (x, y, z).[36,42] This crystal exhibits a similar structure to some bixbyite crystals (e.g., In_2O_3 and Mn_2O_3).[8,9,36] δ-Ga_2O_3 has two inequivalent octahedral Ga sites and one tetrahedral O site.[42,43] The lattice parameters of δ-Ga_2O_3 are a = b = c = 9.52 Å, α = β = γ = 90°.[8,9,36]

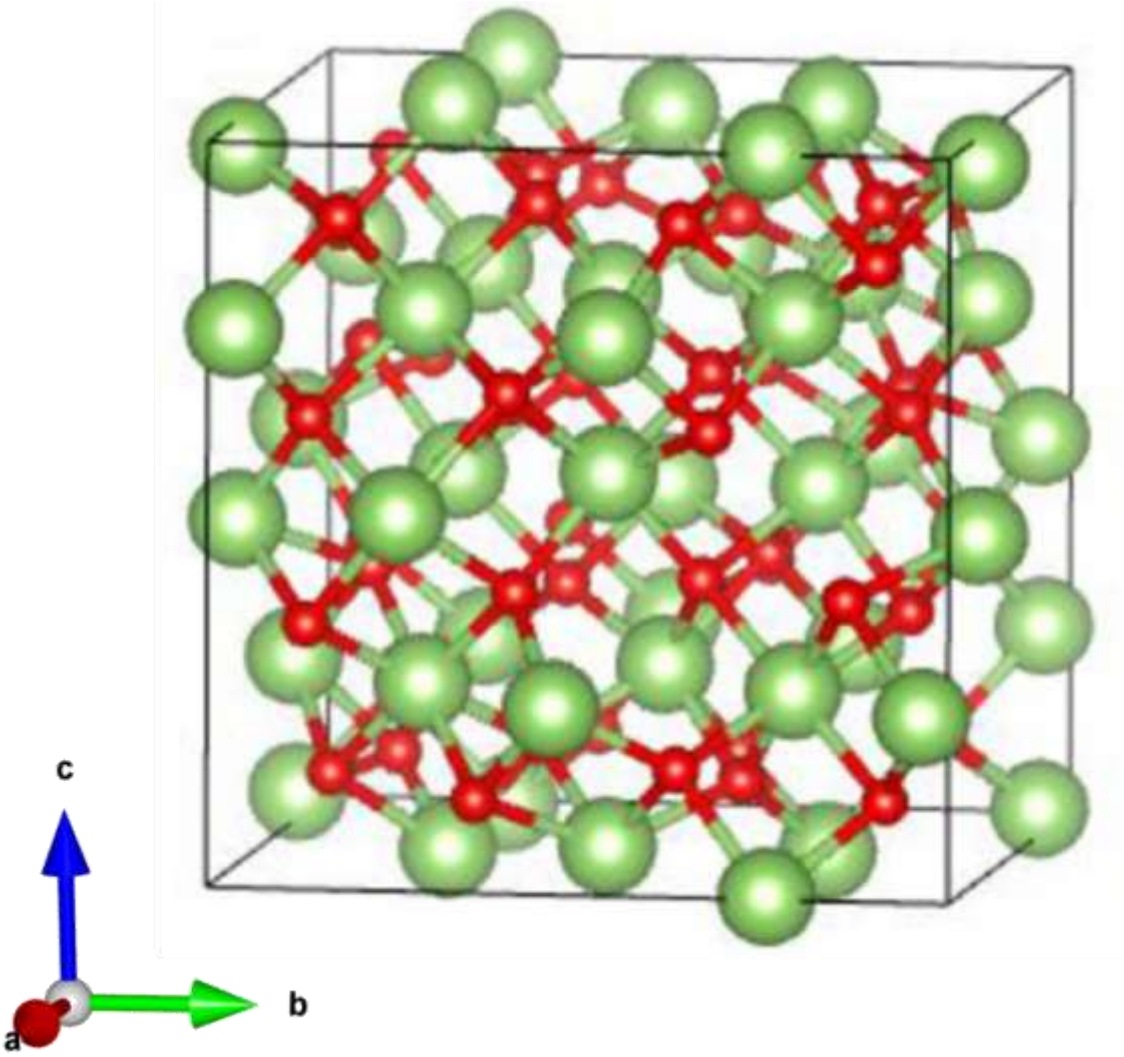

Figure 1.6. The unit cell of δ-Ga_2O_3 crystal structures.[36] Green, and red balls represent Ga and O atoms.

For ε-Ga_2O_3, the lattice parameters are a = b = 2.91 Å and c = 9.26 Å, α = γ = 90°, β = 120°,[9,13,23] which is shown in Fig. 1.7. The space group of ε-Ga_2O_3 is $P6_3mc$; two inequivalent Ga cations are located at Wyckoff positions (2b (2/3, 1/3, z+1/2)), whereas two inequivalent O anions occupy Wyckoff positions ((2a (0, 0, z), 2b (1/3, 2/3, z)).[44] In ε-Ga_2O_3, Ga atoms occupy two inequivalent sites; distorted octahedral and distorted tetrahedral sites.[44,45]

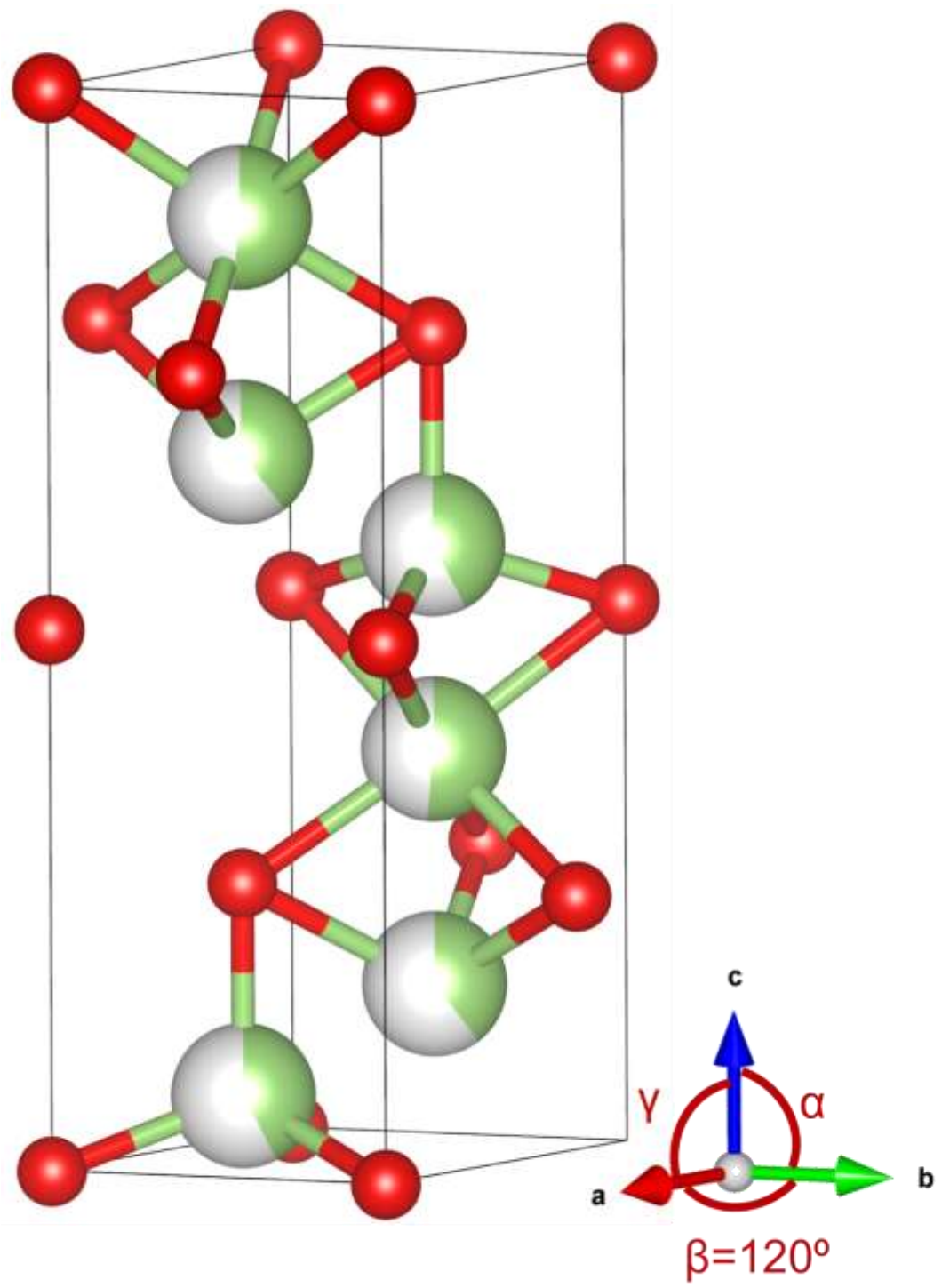

Figure 1.7. The unit cell of ε-Ga_2O_3 crystal structures. Green, and red balls represent Ga and O atoms.

Figure 1.8 shows the unit cell of κ-Ga_2O_3. The lattice parameters of κ-Ga_2O_3 are a = 5.05 Å, b = 8.70 Å, c = 9.28 Å, α = β = γ = 90°.[8-10] κ-Ga_2O_3 exhibits an

orthorhombic crystal structure with a space group of $Pna2_1$. All of the atoms in κ-Ga_2O_3 are located at 4a (x, y, z) Wyckoff positions.[36,46] The unit cell of κ-Ga_2O_3 contains three inequivalent Ga sites and three inequivalent O sites. Half of the Ga cations are in distorted octahedral sites (Ga1 and Ga2), and the other Ga cations are in distorted pentahedral sites (Ga3) and distorted tetrahedral sites (Ga4).[47,48] In-plane 120° rotational directions on the ab-plane are in the orthorhombic domain.[29,49] Therefore, orthorhombic κ-Ga_2O_3 has a larger spontaneous polarization along the (001) direction due to the lack of inversion symmetry with respect to the c-plane.[34,49]

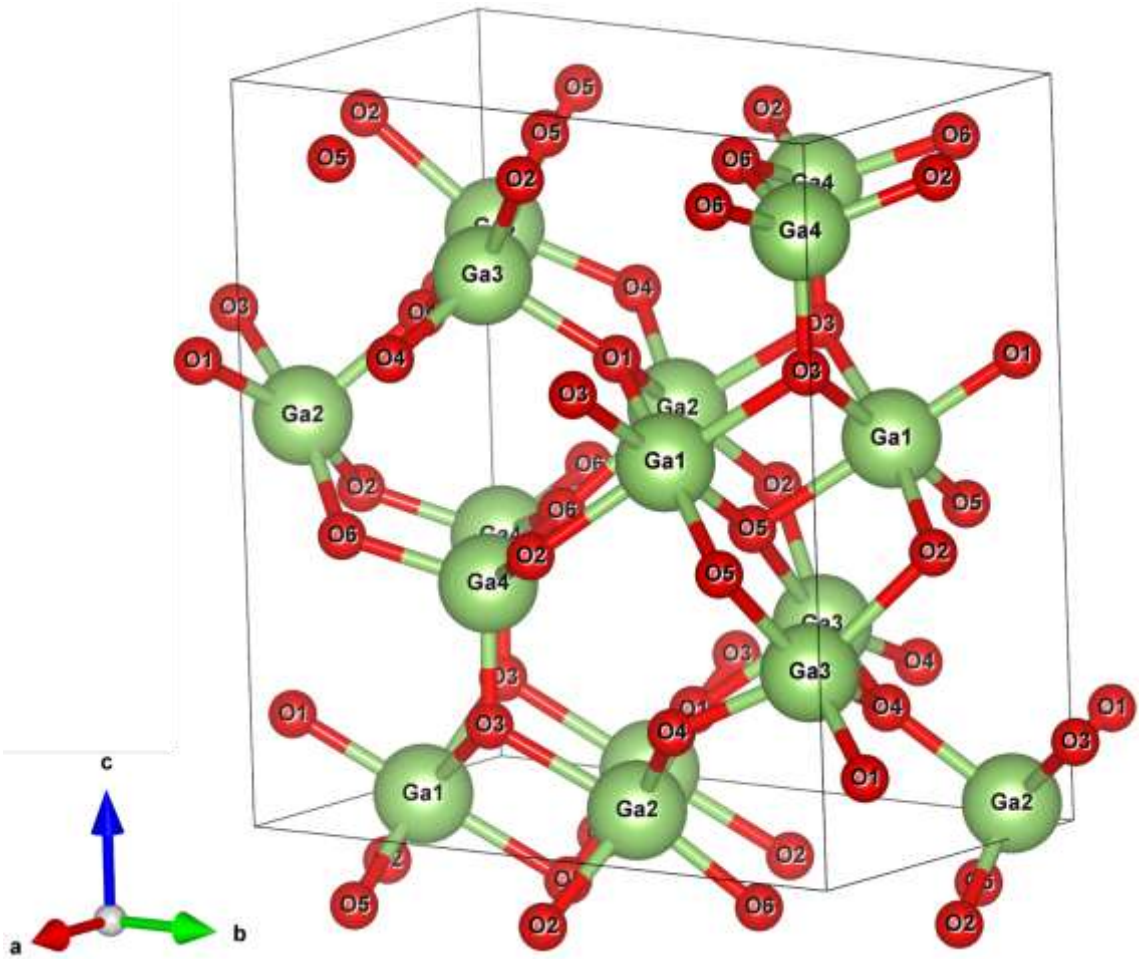

Figure 1.8. The unit cell of κ-Ga_2O_3 crystal structure. Green, and red balls represent Ga and O atoms.

1.3 Dopants for Ga_2O_3

Ga_2O_3 is an insulator because of the wide band gap of 4.5 to 5.3 eV.[9,10] For the electrical conductivity, Si, Sn, Ge, Zn, Nb, Ta and F atoms have been reported as dopants and act as n-type conductivity.[9-11,50-56] The n-type conductivity can also be

controlled by the compensation effect of Mg or Fe atoms doped into the Ga_2O_3.[10,57,58]

For n-type α-Ga_2O_3, Si, Sn, Ge, and F dopants are usually used, and the carrier concentration is around 10^{18}–10^{19} cm^{-3}.[51,54,59-61] In the case of Si-doped α-Ga_2O_3, the Si atoms are uniformly incorporated into the α-Ga_2O_3 films.[51] Furthermore, high quality of single-crystalline Sn-doped α-Ga_2O_3 films are grown by mist chemical vapor deposition (mist-CVD) on c-plane sapphire at atmospheric pressure.[59,62] The carrier concentration of F-doped α-Ga_2O_3 thin films exhibits up to 1.3×10^{19} cm^{-3}. However, the highest mobility of F-doped α-Ga_2O_3 is 4.6 $cm^2/V\cdot s$, which is much lower than that of Si-doped α-Ga_2O_3 (31.5 $cm^2/V\cdot s$) and Sn-doped α-Ga_2O_3 (24 $cm^2/V\cdot s$).[51,60]

In β-Ga_2O_3, Sn and Si are usually used as the n-type dopants due to their low activation energy (7.4 to 60 meV for Sn, 16 to 50 meV for Si).[10] Several melt growth methods for the preparation of n-type β-Ga_2O_3 crystal have been reported; the floating zone (FZ) process, the Czochralski (CZ) process, and the edge-defined film-fed growth (EFG) process.[1,2,63,64] For Si- and Sn-doped β-Ga_2O_3 bulk crystal, the carrier concentration is 10^{16} to 10^{19} cm^{-3}.[9-11]

For epitaxial growth methods such as molecular beam epitaxy (MBE), metal organic vapor phase epitaxy (MOVPE), and pulsed laser deposition (PLD),[65-67] the range of carrier concentration is 10^{19} to 10^{20} cm^{-3} for Si- and Sn-doped β-Ga_2O_3 films.[9,11,65-67] Field-effect transistors (FETs) can be fabricated by the n-type β-Ga_2O_3 channel layers.[65,66] In the case of β-Ga_2O_3 thin film prepared by the MOVPE method, the ohmic contact can be achieved by implanting Si ions.[10,66]

In the case of γ-Ga_2O_3, the Mn dopant acts as a stabilizing agent for the formation of the γ-phase Ga_2O_3.[33,68] For n-type conductivity, Si-doped γ-Ga_2O_3 films can be epitaxially grown on $MgAl_2O_4$ substrates using the PLD method.[50] The Si-doped γ-Ga_2O_3 exhibits a carrier concentration of 1×10^{19} to 2×10^{19} cm^{-3}, and the dopant concentration is $\sim9\times10^{19}$ cm^{-3}. The Hall mobility is 1.6 $cm^2/V\cdot s$.[50] The activation energy of the donor is ~7 meV, whose value is similar to the case of Sn-doped β-Ga_2O_3.[50]

For δ-Ga_2O_3, there are only a few reports on the synthesis of δ-phase Ga_2O_3 structures.[9,69] Recently, Kato et al. reported that the δ-Ga_2O_3 thin film was grown using the mist-CVD method.[20,69] However, for the dopants, it is likely that there are still no reports yet.

In ε-Ga_2O_3, Si and Sn atoms are reported as n-type dopants in ε-Ga_2O_3.[45,70] The Si-doped ε-Ga_2O_3 exhibits a carrier concentration up to 2.1×10^{18} cm^{-3}.[45] In the case of Sn-doped ε-Ga_2O_3, the Sn dopant acts as a stabilizer for the ε phase. However, the sufficient n-type electrical conductivity has not been realized yet.[70]

In the case of κ-Ga_2O_3, Sn and Si dopants are usually used. Sn-doped κ-Ga_2O_3 films can be synthesized using mist-CVD,[47,71] halide vapor phase epitaxy (HVPE),[72] MBE,[73] and PLD[74] on various substrates.[47,71,74] The Sn dopant acts as a stabilizing agent for the formation of the κ-phase Ga_2O_3.[47,71] The carrier concentration is 2.7×10^{17} to 3.8×10^{17} cm^{-3}, and the dopant concentration is up to 10^{19} cm^{-3}.[75] The Hall mobility is 2.3 $cm^2/V\cdot s$ for Sn-doped κ-Ga_2O_3.[75] For the Si-doped κ-Ga_2O_3 film, the most common epitaxial method is MOVPE,[34,75] where SiH_4 is usually used as the dopant source.[19,34,75] The Si dopant forms the shallow donor energy level for the Si-doped κ-Ga_2O_3 thin film. The carrier concentration is ~1×10^{18} to ~5×10^{18} cm^{-3}, and the dopant concentration is up to ~5×10^{20} cm^{-3}. The Hall mobility is 10 $cm^2/V\cdot s$ for Si-doped κ-Ga_2O_3.[34]

Figure 1.9 shows the band dispersion of β-Ga_2O_3. In the figure, almost flat band dispersion is observed near the valence band maximum (VBM) of β-Ga_2O_3. This almost flat band dispersion is attributed to the lone pair electrons of the O 2*p* levels.[2,9,76] Because of the almost flat band dispersion, it is considered not to realize the formation of p-type Ga_2O_3 yet.

There are some density functional theory (DFT) calculations on studies of the formation of p-type Ga_2O_3.[25,77,78] In the DFT calculations, the formation of p-type Ga_2O_3 was predicted when Zn or Cu atom is located at the Ga substitutional site.[77,78] In the DFT calculation, the structure of Ga vacancy bonded with Si_O (O replaced by Si) also showed p-type performance.[25] Kyrtsos et al. used DFT to investigate the possibility of p-type conductivity using Li, Na, K, Be, Mg, Ca, Cu, Au, and Zn as dopants.[76] In their research, all of the dopants show the deep acceptor levels, and the ionization energies are higher than 1 eV.[76] Recently, Chikoidze et al. reported the formation of p-type β-Ga_2O_3 using Zn atom as a dopant.[79] However, in the Hall effect measurements, the dopant energy level was found to be a deep acceptor level and the ionization energy level was 0.77 eV above the VBM, indicating that it needs high temperatures (850 K) to form the electrical conductivity (hole carrier formation).[79] Thus, the realization of p-type conductivity in Ga_2O_3 is still a significant challenge.

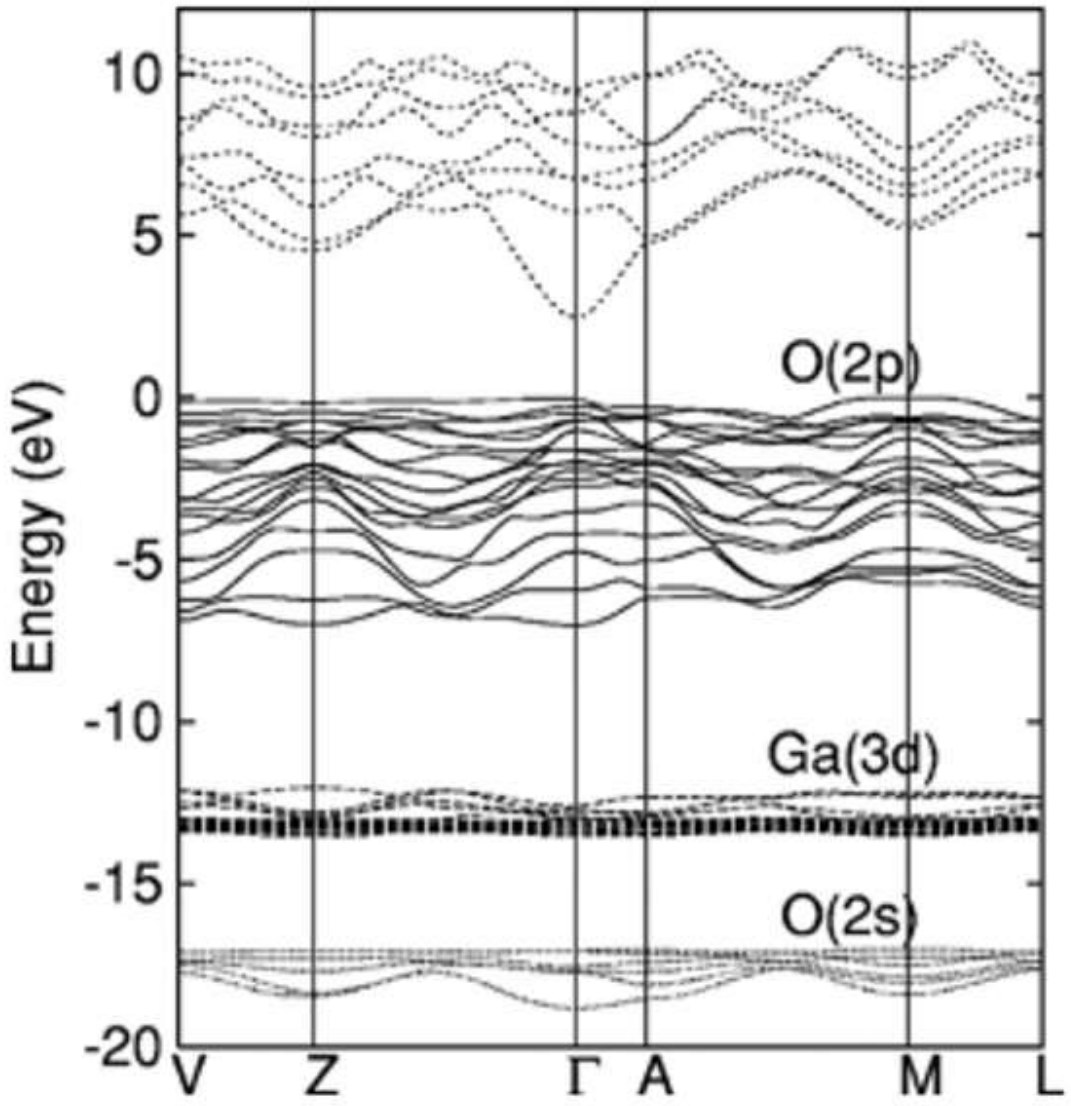

Figure 1.9. The band structure of β-Ga_2O_3. Zero is the Fermi level.[2]

1.4 Current issues of dopants for Ga_2O_3

For the Ga_2O_3-based devices, Sn and Si are mainly used as n-type dopants. However, it has not been clarified how many chemical states exist in Ga_2O_3 and which of the substitutional and/or the interstitial atomic sites is the active dopant one.[34,80,81] In addition, the atomic structures and the chemical states of the inactive dopant sites should be clarified because the inactive dopant sites are the additional carrier scattering sites.[82,83] The additional carrier scattering sites decrease the carrier mobility.[83] Determining the atomic structure and the chemical state of the active and inactive dopant sites in Ga_2O_3 is a necessary step to control the properties of Ga_2O_3-based devices.[34,77,84]

In this thesis, the dopants in β- and κ-phase Ga_2O_3 were selected because they are considered to be suitable for device application among the polymorphs.

For Sn-doped β-Ga_2O_3, there are two inequivalent Ga atomic sites in β-Ga_2O_3; octahedral (Octa) and tetrahedral (Tetra) sites, and three inequivalent O sites.[11,80,85] However, it has not been clarified how many chemical states exist in Sn-doped β-Ga_2O_3 and which is the active or the inactive dopant site.[85,86] Once the atomic structures of the active and inactive dopant sites are revealed, a strategy that increases the activated dopant sites can be developed. As a result, the control of the carrier concentration is possible.

In the case of Si-doped β-Ga_2O_3, the active dopant site is the Tetra Si_{Ga} site (Ga atom is replaced by Si atom).[63] The Si dopant is fully activated, and the carrier concentration is approximately up to 10^{20} cm^{-3},[66] which is sufficiently applied to the devices such as metal oxide field effect transistors (MOSFETs).[11]

For Sn-doped κ-Ga_2O_3, the Sn dopant is the stabilizing agent for the formation of the κ-Ga_2O_3. The carrier concentration is one order lower than that of the Si-doped κ-Ga_2O_3. To achieve the high carrier concentration for κ-Ga_2O_3-based devices, Si dopant is first considered.

In the case of Si-doped κ-Ga_2O_3, the concentration of the carrier is significantly lower than that of the dopants. The previous study showed that the carrier concentration is about a few orders of magnitude less than the dopant concentration.[34] The activation efficiency of the Si dopant in κ-Ga_2O_3 may be affected by the occupation of different reticular Ga sites.[34] Therefore, a method is necessary to clarify the occupation ratio of the different Si dopant sites for the Si-doped κ-Ga_2O_3.

1.5 The purpose of the present thesis

The purpose of the present thesis is to clarify the atomic structures and chemical states of the active and inactive dopant sites of Sn-doped β-Ga_2O_3 and Si-doped κ-Ga_2O_3. Once the atomic structure and the chemical states of the active dopant can be revealed, a strategy can be developed to increase the active dopant sites. As a result, it may be possible to control the carrier concentration. By controlling the carrier concentration, Ga_2O_3 based MOSFETs with high performance could be fabricated. For this purpose, photoelectron spectroscopy (PES), photoelectron holography (PEH), x-ray absorption near-edge structure (XANES), and extended x-ray absorption fine structure spectroscopy (EXAFS) were employed.

1.6 Content Summary

This doctoral thesis is structured into five chapters as follows.

Chapter 1 introduces the general introduction of Ga_2O_3, polymorphs of Ga_2O_3, the dopants for Ga_2O_3, the current issues for Ga_2O_3, and the research purpose of this thesis.

Chapter 2 introduces the sample preparation and characterization methods used in this thesis. The principle of the characterization methods used in this thesis is also explained.

Chapter 3 presents the clarification of the chemical states and the atomic structures of the active dopant sites for the Sn dopants in Sn-doped β-Ga_2O_3 using PES, XANES, and EXAFS.

Chapter 4 presents the clarification of the chemical states and the atomic position occupancy for the Si dopants in Si-doped κ-Ga_2O_3 using PES, chemical state-discriminated PEH, and EXAFS.

Chapter 5 describes the conclusions and the outlook of the thesis.

References

1. C. Wang, J. Zhang, S. Xu, C. Zhang, Q. Feng, Y. Zhang, J. Ning, S. Zhao, H. Zhou, and Y. Hao, *Journal of Physics D: Applied Physics* **54**, 243001 (2021).
2. S.J. Pearton, J. Yang, P.H. Cary, F. Ren, J. Kim, M.J. Tadjer, and M.A. Mastro, *Applied Physics Reviews* **5**, 011301 (2018).
3. E. Ahmadi and Y. Oshima, *Journal of Applied Physics* **126**, 160901 (2019).
4. Y. Oshima and E. Ahmadi, *Applied Physics Letters* **121**, 260501 (2022).
5. M. Higashiwaki, K. Sasaki, H. Murakami, Y. Kumagai, A. Koukitu, A. Kuramata, T. Masui, and S. Yamakoshi, *Semiconductor Science and Technology* **31**, 034001 (2016).
6. S.J. Pearton, F. Ren, M. Tadjer, and J. Kim, *Journal of Applied Physics* **124**, 220901 (2018).
7. A. Kumar, S. Singh, and D. Shukla, *International Journal for Research in Applied Science and Engineering Technology* **10**, 360 (2022).
8. K. Kaneko, K. Uno, R. Jinno, and S. Fujita, *Journal of Applied Physics* **131**, 090902 (2022).
9. Y. Wang, J. Su, Z. Lin, J. Zhang, J. Chang, and Y. Hao, *Journal of Materials Chemistry C* **10**, 13395 (2022).
10. J. Zhang, J. Shi, D. Qi, L. Chen, and K. Zhang, *APL Materials* **8**, 020906 (2020).
11. H. Zhang, L. Yuan, X. Tang, J. Hu, J. Sun, Y. Zhang, Y. Zhang, and R. Jia, *IEEE Transactions on Power Electronics* **35**, 5157 (2020).
12. Y. Qin, Z. Wang, K. Sasaki, J. Ye, and Y. Zhang, *Japanese Journal of Applied Physics* **62**, SF0801 (2023).
13. X. Hou, Y. Zou, M. Ding, Y. Qin, Z. Zhang, X. Ma, P. Tan, S. Yu, X. Zhou, X. Zhao, G. Xu, H. Sun, and S. Long, *Journal of Physics D: Applied Physics* **54**, 043001 (2020).
14. A.Y. Polyakov, V.I. Nikolaev, E.B. Yakimov, F. Ren, S.J. Pearton, and J. Kim, *Journal of Vacuum Science & Technology A* **40**, 020804 (2022).
15. M.A. Mastro, A. Kuramata, J. Calkins, J. Kim, F. Ren, and S.J. Pearton, *ECS Journal of Solid State Science and Technology* **6**, P356 (2017).
16. M. Higashiwaki, K. Sasaki, A. Kuramata, T. Masui, and S. Yamakoshi, *Applied Physics Letters* **100**, 013504 (2012).
17. J. Yang, Y. Xu, X. Wang, X. Zhang, Y. He, and H. Sun, *Applied Physics Express* **17**, 011001 (2023).
18. Z. Fei, Z. Chen, W. Chen, S. Chen, Z. Wu, X. Lu, G. Wang, J. Liang, and Y. Pei, *Journal of Alloys and Compounds* **925**, 166632 (2022).
19. J. Lee, H. Kim, L. Gautam, and M. Razeghi, *Crystals* **11**, 446 (2021).
20. T. Kato, H. Nishinaka, K. Shimazoe, and M. Yoshimoto, *Physica Status Solidi (a)*, 2300582 (2023).

21. K. Kaneko, S. Fujita, T. Shinohe, and K. Tanaka, *Japanese Journal of Applied Physics* **62**, SF0803 (2023).
22. M.D. McCluskey, *Journal of Applied Physics* **127**, 101101 (2020).
23. Z. Galazka, *Semiconductor Science and Technology* **33**, 113001 (2018).
24. I. Cora, F. Mezzadri, F. Boschi, M. Bosi, M. Čaplovičová, G. Calestani, I. Dódony, B. Pécz, and R. Fornari, *CrystEngComm* **19**, 1509 (2017).
25. C.J. Zeman, S.M. Kielar, L.O. Jones, M.A. Mosquera, and G.C. Schatz, *Journal of Alloys and Compounds* **877**, 160227 (2021).
26. D. Guo, Q. Guo, Z. Chen, Z. Wu, P. Li, and W. Tang, *Materials Today Physics* **11**, 100157 (2019).
27. J.L. Hudgins, G.S. Simin, E. Santi, and M.A. Khan, *IEEE Transactions on Power Electronics* **18**, 907 (2003).
28. M.D. Vecchia, S. Ravyts, G. Broeck, and J. Driesen, *Energies* **12**, 2663 (2019).
29. H. Nishinaka, H. Komai, D. Tahara, Y. Arata, and M. Yoshimoto, *Japanese Journal of Applied Physics* **57**, 115601 (2018).
30. M. Oda, R. Tokuda, H. Kambara, T. Tanikawa, T. Sasaki, and T. Hitora, *Applied Physics Express* **9**, 021101 (2016).
31. R. Huang, H. Hayashi, F. Oba, and I. Tanaka, *Journal of Applied Physics* **101**, 063526 (2007).
32. H. Hayashi, R. Huang, H. Ikeno, F. Oba, S. Yoshioka, I. Tanaka, and S. Sonoda, *Applied Physics Letters* **89**, 181903 (2006).
33. H. Hayashi, R. Huang, F. Oba, T. Hirayama, and I. Tanaka, *Journal of Materials Research* **26**, 578 (2011).
34. P. Mazzolini, Z. Fogarassy, A. Parisini, F. Mezzadri, D. Diercks, M. Bosi, L. Seravalli, A. Sacchi, G. Spaggiari, D. Bersani, O. Bierwagen, B.M. Janzen, M.N. Marggraf, M.R. Wagner, I. Cora, B. Pécz, A. Tahraoui, A. Bosio, C. Borelli, S. Leone, and R. Fornari, *Advanced Functional Materials* **33**, 2207821 (2022).
35. R. Sharma, E. Patlick, J. Yang, F. Ren, M. Law and S. Pearton, Electro-Thermal Analysis and Edge Termination Techniques of High Current β-Ga_2O_3 Schottky Rectifiers, in *2019 International Conference on Simulation of Semiconductor Processes and Devices (SISPAD)*, Udine, Italy, 2019, pp. 1-4
36. F. Safieddine, F. Hassan, and M. Kazan, *Journal of Solid State Chemistry* **312**, 123272 (2022).
37. F. Litimein, D. Rached, R. Khenata, and H. Baltache, *Journal of Alloys and Compounds* **488**, 148 (2009).
38. G. Yang, P.R. Romeo, A. Apostoluk, and B. Vilquin, *Journal of Vacuum Science & Technology A* **40**, 052801 (2022).
39. S. Geller, *The Journal of Chemical Physics* **33**, 676 (1960).

40. J. Tang, K. Jiang, C. Xu, M.J. Cabral, K. Xiao, L.M. Porter, and R.F. Davis, *APL Materials* **12**, 011109 (2024).
41. H.Y. Playford, A.C. Hannon, M.G. Tucker, D.M. Dawson, S.E. Ashbrook, R.J. Kastiban, J. Sloan, and R.I. Walton, *The Journal of Physical Chemistry C* **118**, 16188 (2014).
42. M.B. Maccioni, F. Ricci, and V. Fiorentini, *Journal of Physics: Condensed Matter* **28**, 224001 (2016).
43. T. Gake, Y. Kumagai, and F. Oba, *Physical Review Materials* **3**, 044603 (2019).
44. F. Mezzadri, G. Calestani, F. Boschi, D. Delmonte, M. Bosi, and R. Fornari, *Inorganic Chemistry* **55**, 12079 (2016).
45. H.J. von Bardeleben, J.L. Cantin, A. Parisini, A. Bosio, and R. Fornari, *Physical Review Materials* **3**, 084601 (2019).
46. A. Devamanoharan, V. Venkatachalapathy, V. Veerapandy, and P. Vajeeston, *ACS Omega* **9**, 16207 (2024).
47. H. Kang, Y. Choi, K. Pyeon, T. Lee, and R. Chung, *Journal of Materials Science* **57**, 19882 (2022).
48. S. Seacat, J.L. Lyons, and H. Peelaers, *Applied Physics Letters* **119**, 042104 (2021).
49. Y. Oshima, K. Kawara, T. Oshima, and T. Shinohe, *Japanese Journal of Applied Physics* **59**, 115501 (2020).
50. T. Oshima, K. Matsuyama, K. Yoshimatsu, and A. Ohtomo, *Journal of Crystal Growth* **421**, 23 (2015).
51. T. Uchida, K. Kaneko, and S. Fujita, *MRS Advances* **3**, 171 (2018).
52. J. Yan and C. Qu, *Journal of Semiconductors* **37**, 042002 (2016).
53. F. Alema, G. Seryogin, A. Osinsky, and A. Osinsky, *APL Materials* **9**, 091102 (2021).
54. T. Shu, R. Miao, S. Guo, S. Wang, C. Zhao, and X. Zhang, *Chinese Physics B* **29**, 126301 (2020).
55. W. Zhou, C. Xia, Q. Sai, and H. Zhang, *Applied Physics Letters* **111**, 242103 (2017).
56. J. Jesenovec, J. Varley, S.E. Karcher, and J.S. McCloy, *Journal of Applied Physics* **129**, 225702 (2021).
57. M.H. Wong, C.-H. Lin, A. Kuramata, S. Yamakoshi, H. Murakami, Y. Kumagai, and M. Higashiwaki, *Applied Physics Letters* **113**, 102103 (2018).
58. S. Bhandari, M.E. Zvanut, and J.B. Varley, *Journal of Applied Physics* **126**, 165703 (2019).
59. G.T. Dang, T. Kawaharamura, M. Furuta, and M.W. Allen, *IEEE Transactions on Electron Devices* **62**, 3640 (2015).
60. S. Morimoto, H. Nishinaka, and M. Yoshimoto, *Thin Solid Films* **682**, 18 (2019).
61. T. Kawaharamura, G.T. Dang, and M. Furuta, *Japanese Journal of Applied Physics* **51**, 040207 (2012).

62. K. Akaiwa, K. Ota, T. Sekiyama, T. Abe, T. Shinohe, and K. Ichino, *Physica Status Solidi (a)* **217**, 1900632 (2020).
63. E.G. Víllora, K. Shimamura, Y. Yoshikawa, T. Ujiie, and K. Aoki, *Applied Physics Letters* **92**, 202120 (2008).
64. A. Kuramata, K. Koshi, S. Watanabe, Y. Yamaoka, T. Masui, and S. Yamakoshi, *Japanese Journal of Applied Physics* **55**, 1202A2 (2016).
65. K. Sasaki, M. Higashiwaki, A. Kuramata, T. Masui, and S. Yamakoshi, *Journal of Crystal Growth* **378**, 591 (2013).
66. M. Baldini, M. Albrecht, A. Fiedler, K. Irmscher, R. Schewski, and G. Wagner, *ECS Journal of Solid State Science and Technology* **6**, Q3040 (2016).
67. K.D. Leedy, K.D. Chabak, V. Vasilyev, D.C. Look, K. Mahalingam, J.L. Brown, A.J. Green, C.T. Bowers, A. Crespo, D.B. Thomson, and G.H. Jessen, *APL Materials* **6**, 101102 (2018).
68. Y. Huang, Z. Liu, J. Wang, Y. Zhi, D. Guo, X. Wang, X. Wang, Z. Chen, P. Li, and W. Tang, *ECS Journal of Solid State Science and Technology* **9**, 055010 (2020).
69. H. Nishinaka, *Journal of the Society of Materials Science, Japan* **72**, 750 (2023).
70. Y. Cai, K. Zhang, Q. Feng, Y. Zuo, Z. Hu, Z. Feng, H. Zhou, X. Lu, C. Zhang, W. Tang, J. Zhang, and Y. Hao, *Optical Materials Express* **8**, 3506 (2018).
71. H.Y. Kang, H. Kang, E. Lee, G.R. Lee, and R. Chung, *ACS Omega* **6**, 31292 (2021).
72. V.I. Nikolaev, S.I. Stepanov, A.I. Pechnikov, S.V. Shapenkov, M.P. Scheglov, A.V. Chikiryaka, and O.F. Vyvenko, *ECS Journal of Solid State Science and Technology* **9**, 045014 (2020).
73. M. Kracht, A. Karg, J. Schörmann, M. Weinhold, D. Zink, F. Michel, M. Rohnke, M. Schowalter, B. Gerken, A. Rosenauer, P.J. Klar, J. Janek, and M. Eickhoff, *Physical Review Applied* **8**, 054002 (2017).
74. M. Kneiß, A. Hassa, D. Splith, C. Sturm, H. Wenckstern, T. Schultz, N. Koch, M. Lorenz, and M. Grundmann, *APL Materials* **7**, 022516 (2019).
75. A. Parisini, A. Bosio, V. Montedoro, A. Gorreri, A. Lamperti, M. Bosi, G. Garulli, S. Vantaggio, and R. Fornari, *APL Materials* **7**, 031114 (2019).
76. A. Kyrtsos, M. Matsubara, and E. Bellotti, *Applied Physics Letters* **112**, 032108 (2018).
77. C. Li, J. Yan, L. Zhang, and G. Zhao, *Chinese Physics B* **21**, 127104 (2012).
78. C. Zhang, Z. Li, and W. Wang, *Materials* **14**, 5161 (2021).
79. E. Chikoidze, C. Sartel, H. Yamano, Z. Chi, G. Bouchez, F. Jomard, V. Sallet, G. Guillot, K. Boukheddaden, A. Pérez-Tomás, T. Tchelidze, and Y. Dumont, *Journal of Vacuum Science & Technology A* **40**, 043401 (2022).
80. S.C. Siah, R.E. Brandt, K. Lim, L.T. Schelhas, R. Jaramillo, M.D. Heinemann, D. Chua, J. Wright, J.D. Perkins, C.U. Segre, R.G. Gordon, M.F. Toney, and T. Buonassisi, *Applied Physics Letters* **107**, 252103 (2015).

81. C. Wang, B. Lee, F. Shieu, and H. Shih, *Chemical Physics Letters* **753**, 137624 (2020).
82. Y. Kato, D. Tsujikawa, Y. Hashimoto, T. Yoshida, S. Fukami, H. Matsuda, M. Taguchi, T. Matsushita, and H. Daimon, *Applied Physics Express* **11**, 061302 (2018).
83. P. Ščajev, A. Mekys, L. Subačius, S. Stanionytė, D. Kuciauskas, K.G. Lynn, and S.K. Swain, *Scientific Reports* **12**, 12851 (2022).
84. E. Chikoidze, C. Sartel, H. Mohamed, I. Madaci, T. Tchelidze, M. Modreanu, P. Vales-Castro, C. Rubio, C. Arnold, V. Sallet, Y. Dumont, and A. Perez-Tomas, *Journal of Materials Chemistry C* **7**, 10231 (2019).
85. H. Arima-Osonoi, K. Yamazaki, R. Simura, T. Sugawara, K. Yubuta, K. Sugiyama, and A. Yoshiasa, *Journal of Crystal Growth* **570**, 126223 (2021).
86. S. Ohira, N. Suzuki, N. Arai, M. Tanaka, T. Sugawara, K. Nakajima, and T. Shishido, *Thin Solid Films* **516**, 5763 (2008).

Chapter 2 Experimental

2.1 Sample preparation for Sn-doped β-Ga_2O_3 and Si-doped κ-Ga_2O_3

The Sn-doped β-Ga_2O_3(001) substrates were grown using the EFG process. The substrates were purchased from Novel Crystal Technology, Inc.[1,2] The sample preparation for the EFG process is shown in Fig. 2.1.[1] The source material was 5N-grade Ga_2O_3 powder. Tin dioxide (SnO_2) powder was introduced into the Ga_2O_3 to grow doped n-type crystals. The SnO_2 powder concentration is 0.08 mol%.[1] The powder was placed in an iridium crucible combined with an iridium die. The growth pressure was 1 atm. The growth atmosphere contained 98% N_2 and 2% O_2. The powder was heated up to the melting point of β-Ga_2O_3 (1800°C). The molten Ga_2O_3 then ascended by capillary action through a slit to the top of the die. At the top of the die, crystal growth then occurred.[1]

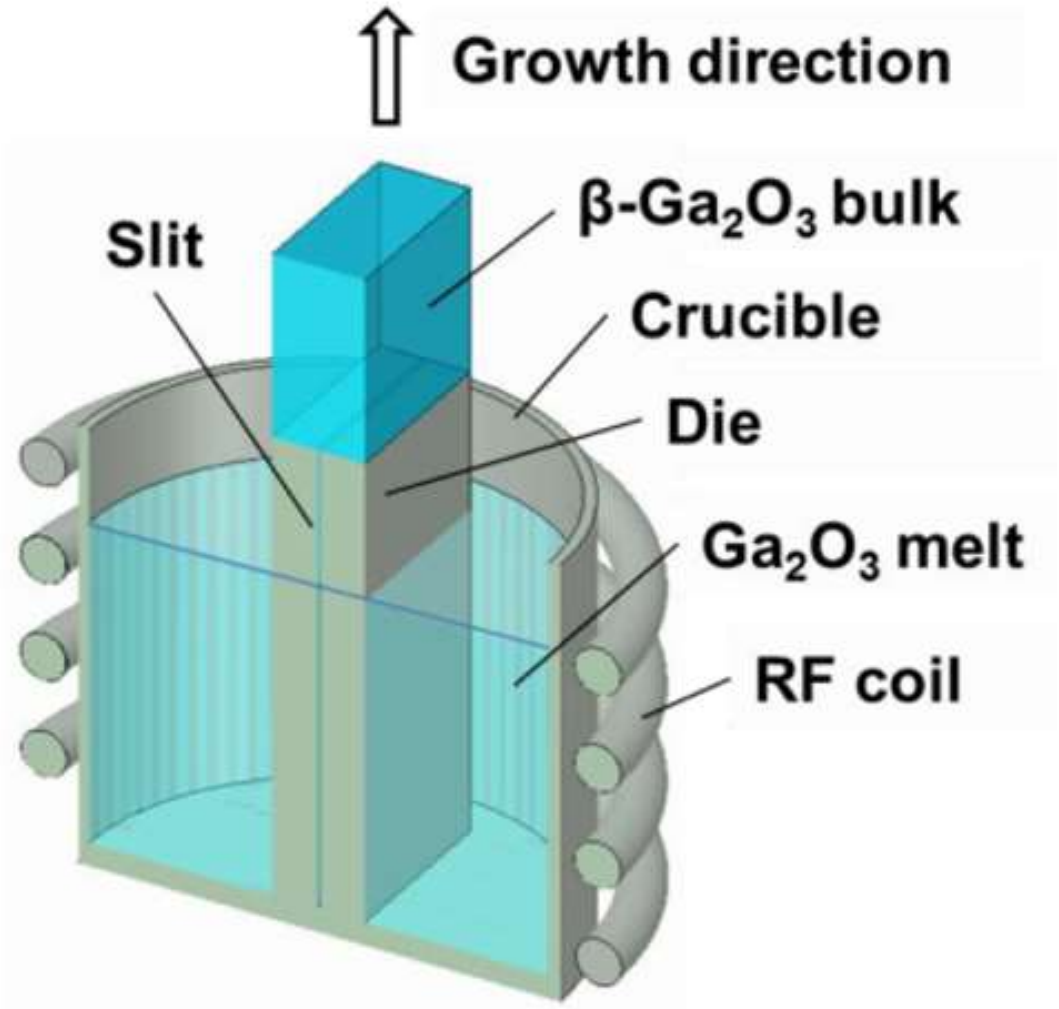

Figure 2.1. Schematic diagram of the EFG process.[1]

The Si-doped κ-Ga_2O_3(001) epitaxial layers prepared by the MOVPE method were used in the present study. Figure 2.2 shows the MOVPE reaction chamber.[3] The Si-doped κ-Ga_2O_3 epitaxial layers were grown on a c-plane sapphire substrate. Trimethylgallium and ultrapure H_2O were used as the metal precursor and the oxidizing gas. H_2 at a flow rate of 2000 standard cubic centimeters per minute (sccm) was used as the gas carrier. The reaction was carried out at an H_2 pressure of 60 mbar in the reaction chamber. The substrate temperature was 610°C. A H_2-diluted mixture of 0.05% SiH_4 was used as the Si dopant source.[4,5] By controlling the flow of SiH_4, it was possible to obtain Si-doped κ-Ga_2O_3 samples with different Si concentrations.

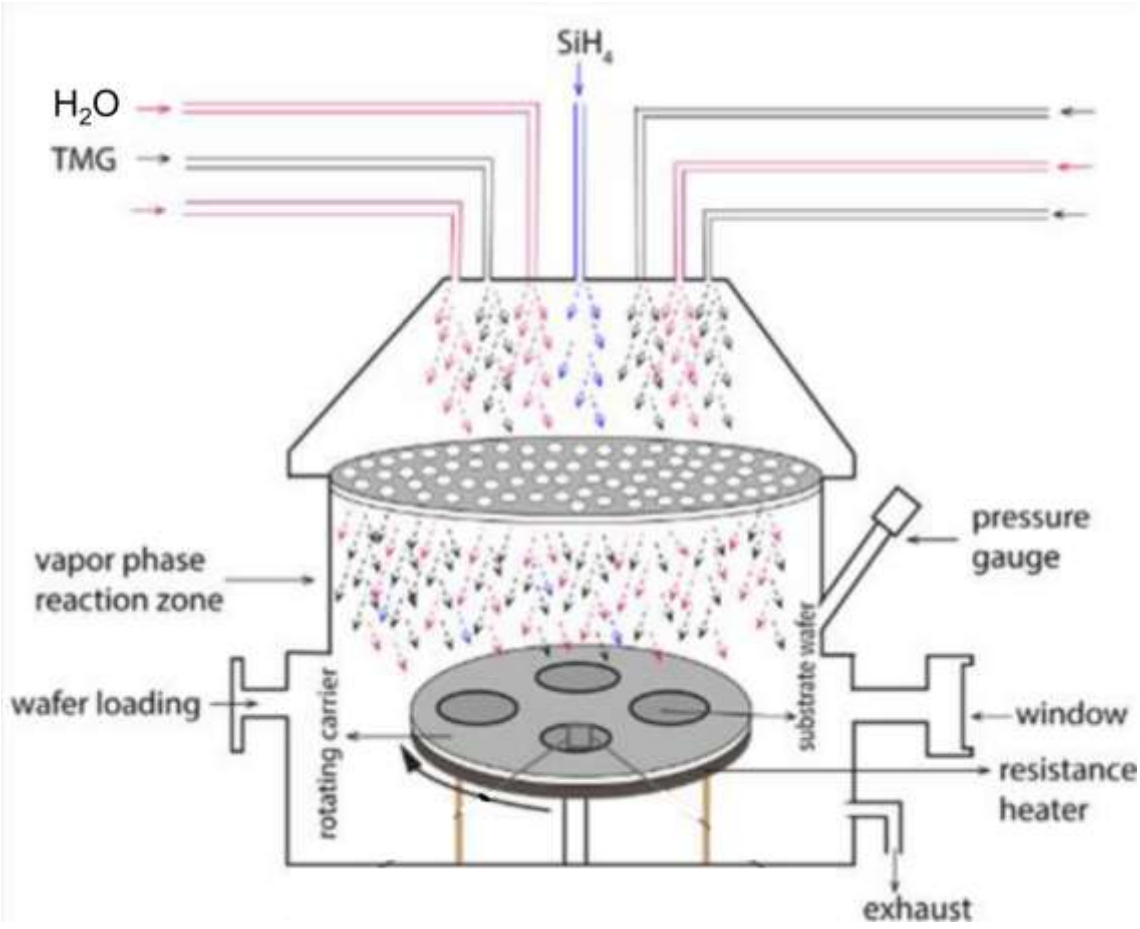

Figure 2.2. A schematic of the MOVPE reaction chamber.[3]

2.2 Characterization Methods

2.2.1 Secondary Ion Mass Spectrometry (SIMS)

SIMS is a well-established analysis method, and it is widely used in various scientific fields. SIMS provides detailed elemental information toward depth.[6-9] Figure 2.3 shows the schematic of the SIMS experiment.[9] As a primary ion beam irradiates a solid sample in a high vacuum environment, SIMS exhibits a sputtering phenomenon that releases secondary ions from the sample surface. These secondary ions are detected by a mass-separated ion detector, providing detailed information on the elemental and molecular composition of the sample.

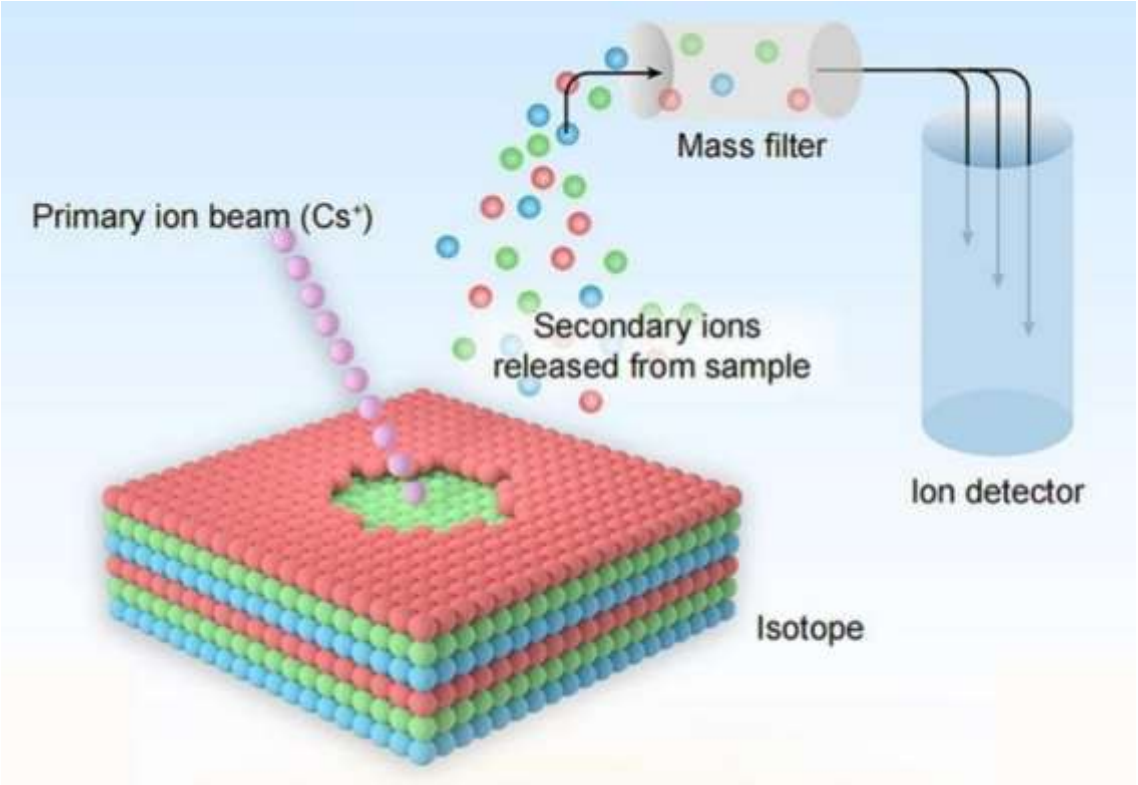

Figure 2.3. The schematic of the SIMS experiment.[9]

For the mass separation of SIMS, three types of methods are usually used; magnetic sector SIMS, quadrupole mass spectrometer (Q-Mass) SIMS, and time-of-flight SIMS (ToF-SIMS). In this thesis, magnetic sector SIMS was employed.

Magnetic sector SIMS uses a double-focusing mass spectrometer based on the coupling of the magnetic sector with an electrostatic sector for efficient mass separation. Figure 2.4 shows the schematics of the double-focusing magnetic mass spectrometers.[10] A magnetic sector spectrometer is based on the separation of secondary ions according to the mass-to-charge ratio.[6,11] As the secondary ions pass through the magnetic field, a force is applied to the particles at 90° angles to both the direction of motion and the magnetic field. The following equations (2.1) to (2.4) show the relationship between the magnetic field (B), the secondary ion acceleration voltage (V), the mass-to-charge ratio (m/q), and the radius of curvature of the ion path (r) in the magnetic field.

Since the potential energy E_p of a charged particle is converted to kinetic energy E_k, qV is described as the following equation,

$$\frac{1}{2}mv^2 = qV \tag{2.1}$$

where v is the secondary ion velocity. When the secondary ions pass through the magnetic field, the Lorentz force is equal to the centrifugal force, which is described as the following equations,

$$\frac{mv^2}{r} = qvB \tag{2.2}$$

$$v = \frac{qBr}{m} \tag{2.3}$$

Substituting the equations (2.1), (2.2), and (2.3), the mass-to-charge ratio is equal to,

$$\frac{m}{q} = \frac{B^2r^2}{2\mathrm{V}} \tag{2.4}$$

The mass-to-charge ratio of the secondary ions and the content of different components can be estimated using the above formula.[6]

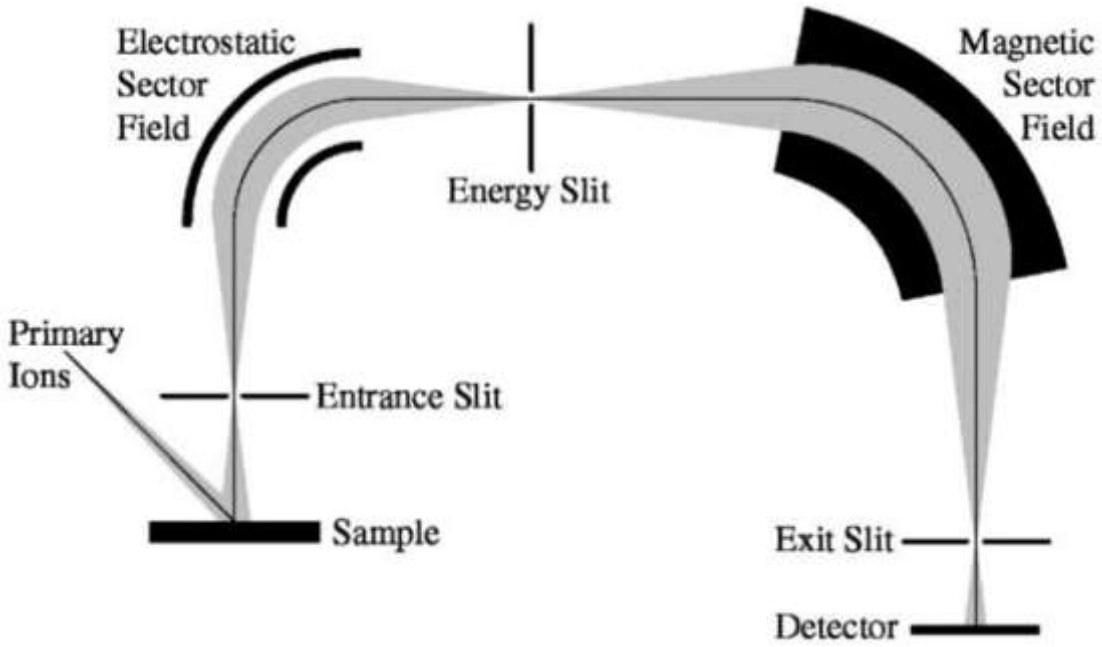

Figure 2.4. The double-focusing magnetic mass spectrometers used to separate ions by mass.[10]

2.2.2 Hall effect measurements

In the present thesis, the Van der Pauw method was employed for the Hall effect measurement of the carrier concentration.[12-16] The Van der Pauw method is a suitable method for measuring the carrier concentration in a homogeneous, flat, uniform-thickness sample. For the Van der Pauw method, four probes are placed on the sample's corners. The apparatus for Hall effect measurements using the Van der Pauw method is shown in Fig. 2.5.

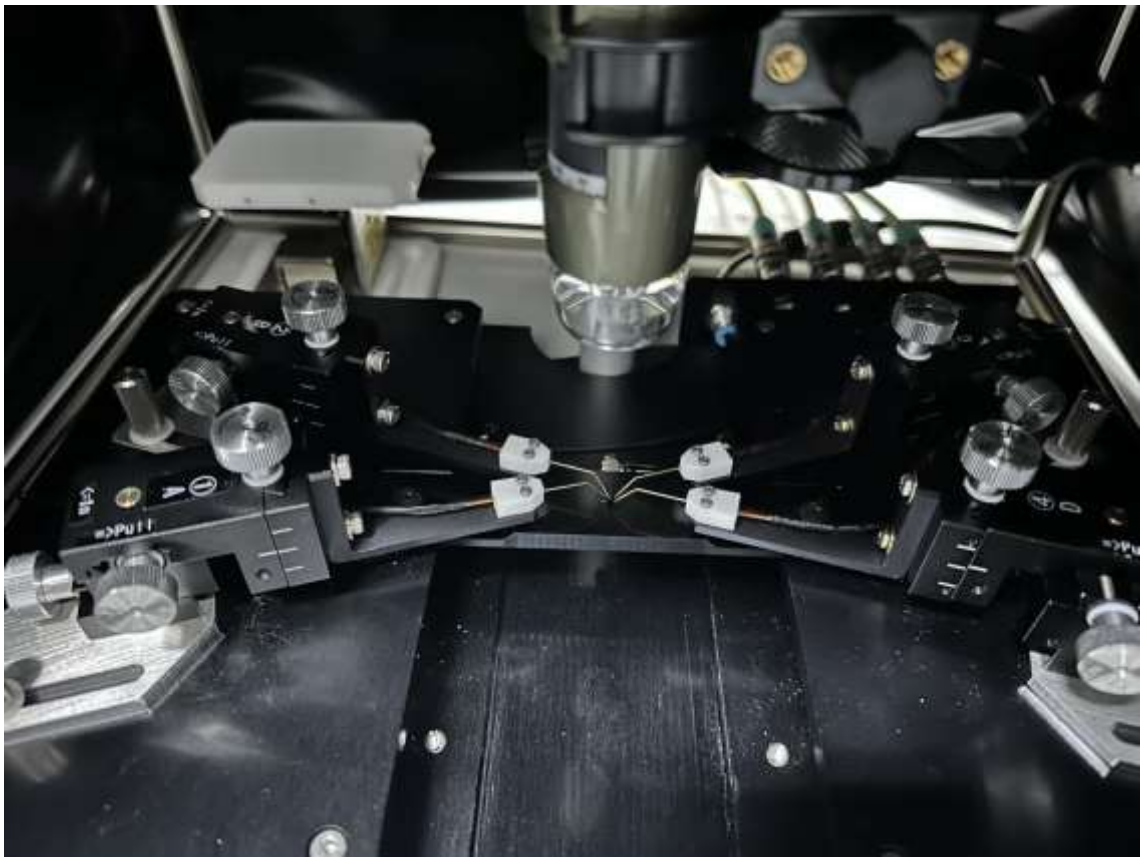

Figure 2.5. Photo of apparatus of Hall effect measurements.

The sheet resistance (R_S) can be obtained from the Van der Pauw formula,[13] thus, the equation (2.5) is described as,

$$e^{\frac{-\pi R_A}{R_S}} + e^{\frac{-\pi R_B}{R_S}} = 1 \tag{2.5}$$

where R_A and R_B are the characteristic resistances. R_A and R_B are described as the following formulas,

$$R_A = \frac{V_{43}}{I_{12}} \tag{2.6}$$

$$R_B = \frac{V_{14}}{I_{23}} \tag{2.7}$$

Figure 2.6 shows the experimental setup for the measurements of R_A and R_B using the Van der Pauw Hall method. From the Van der Pauw equation, R_A and R_B are described as the follow,[13]

$$R_A = \frac{V_{43}}{I_{12}} = \frac{V_{34}}{I_{21}} = R'_A \tag{2.8}$$

$$R_B = \frac{V_{14}}{I_{23}} = \frac{V_{41}}{I_{32}} = R'_B \tag{2.9}$$

It is therefore possible to obtain a more accurate value for the resistances by performing additional measurements of their reciprocal values. Thus, the $R_{vertical}$ and $R_{horizontal}$ can be defined by the following formulas,

$$R_{vertical} = \frac{R_A + R'_A}{2} \tag{2.10}$$

$$R_{horizontal} = \frac{R_B + R'_B}{2} \tag{2.11}$$

Then, the Van der Pauw formula can be expressed as,

$$e^{\frac{-\pi R_{vertical}}{R_S}} + e^{\frac{-\pi R_{horizontal}}{R_S}} = 1 \tag{2.12}$$

By alternately switching the polarities of both the current source and the voltage meter, it is possible to improve the accuracy of the resistance values. All the setup for measuring the resistances using the Van der Pauw Hall method is shown in Fig. 2.7.

Thus, the $R_{vertical}$ and $R_{horizontal}$ are described as the following formulas,

$$R_{vertical} = \frac{\frac{V_{43}}{I_{12}} + \frac{V_{34}}{I_{21}} + \frac{V_{12}}{I_{43}} + \frac{V_{21}}{I_{34}}}{4} \tag{2.13}$$

$$R_{horizontal} = \frac{\frac{V_{14}}{I_{23}} + \frac{V_{41}}{I_{32}} + \frac{V_{23}}{I_{14}} + \frac{V_{32}}{I_{41}}}{4} \quad (2.14)$$

In the case of $R_{vertical} = R = R_{horizontal}$, Rs is described as $\frac{\pi R}{ln2}$.

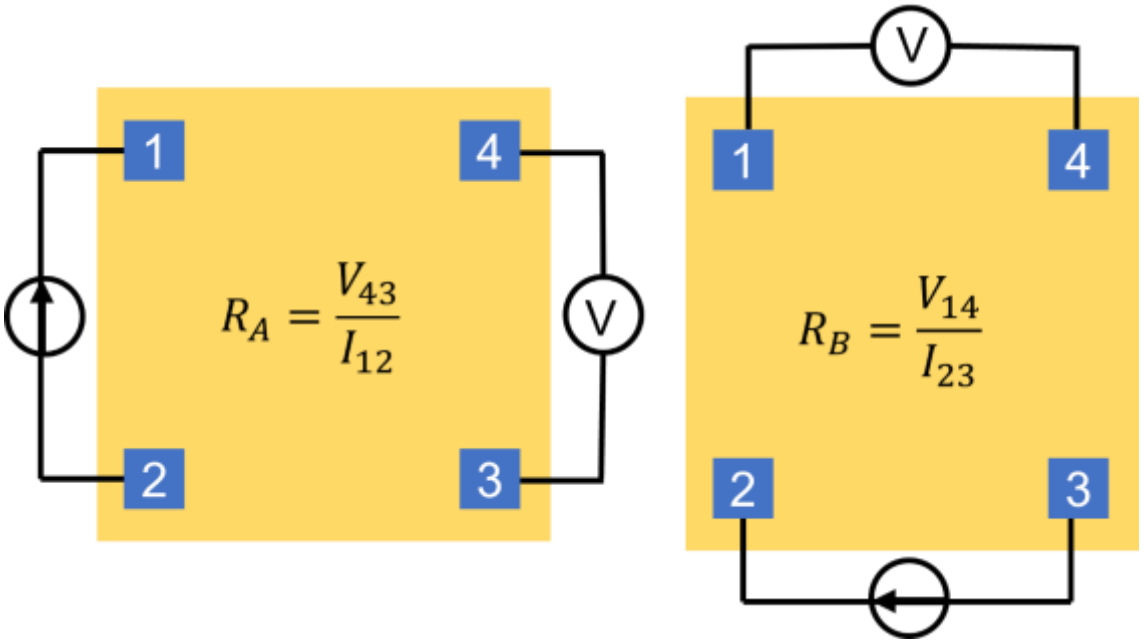

Figure 2.6. Van der Pauw method for measurements of R_A and R_B.

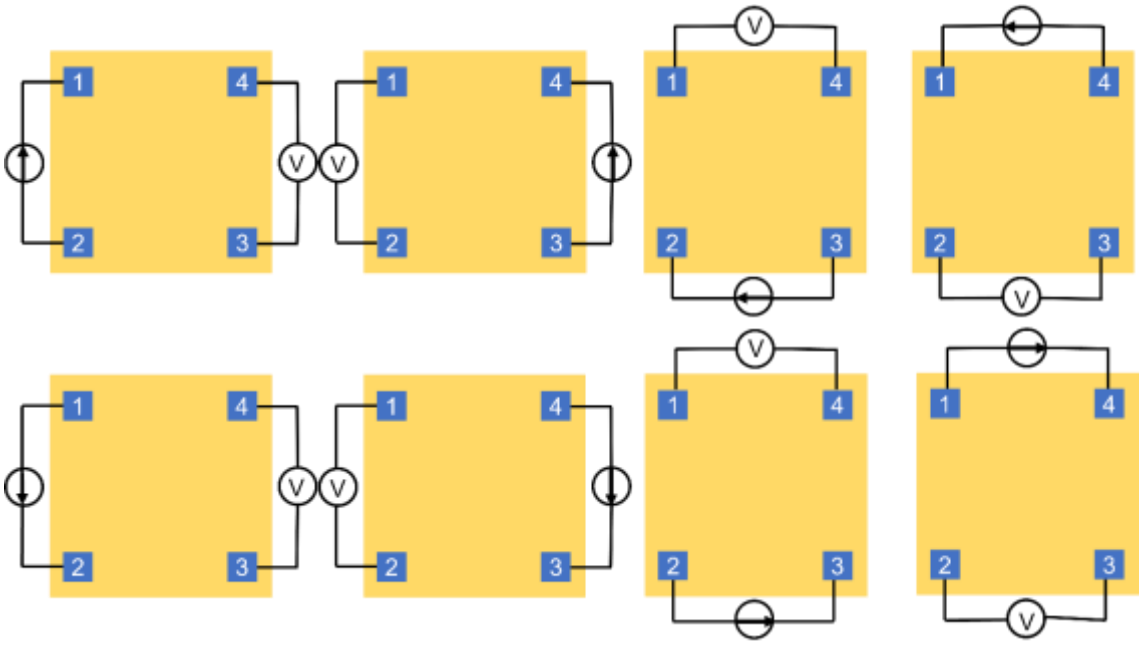

Figure 2.7. The experimental setup in Van der Pauw Hall method for the resistance measurements.

The resistivity of semiconductor material is given by,[17]

$$\rho = \frac{1}{q(n\mu_n + p\mu_p)} \tag{2.15}$$

where q is the elementary charge, n and p are the concentrations of electrons and holes, respectively. μ_n and μ_p are the mobility of the electrons and holes, respectively. For the N-type semiconductors, the resistivity is described as,

$$\rho = \frac{1}{qn\mu_n} \tag{2.16}$$

in the case of P-type semiconductors, the resistivity is described as,

$$\rho = \frac{1}{qp\mu_p} \tag{2.17}$$

Since the sheet resistance R_S is equal to the resistivity divided by the thickness t, R_S is described as,

$$R_S = \frac{\rho}{t} \tag{2.18}$$

the R_S is also described as,

$$R_S = \frac{1}{qn_S\mu_m} \tag{2.19}$$

where n_S is the sheet density, m is the majority carrier type.

The magnitude of the Hall voltage (V_H) is expressed as the follow,

$$V_H = \frac{IB}{q*(n*t)} = \frac{IB}{q*n_S} \tag{2.20}$$

where I is the electric current, B is the magnetic field. Thus, the carrier mobility is described as,

$$\mu_m = \frac{V_H}{R_S IB} \tag{2.21}$$

To obtain V_H by Van der Pauw Hall measurements, another configuration is additionally needed. The setup for measuring the Hall voltage using the Van der Pauw method is shown in Fig. 2.8. Two magnetic field is required for the measurements. One is positive magnetic field, whereas the other is negative magnetic field.[12,15] For the positive magnetic field, $V_{24}^P, V_{42}^P, V_{13}^P, V_{31}^P$ are employed. For the negative magnetic field, $V_{24}^N, V_{42}^N, V_{13}^N, V_{31}^N$ are used.

Then, the differences in the voltages are defined as,

$$V_{24} = V_{24}^P - V_{24}^N \tag{2.22}$$
$$V_{42} = V_{42}^P - V_{42}^N \tag{2.23}$$
$$V_{13} = V_{13}^P - V_{13}^N \tag{2.24}$$
$$V_{31} = V_{31}^P - V_{31}^N \tag{2.25}$$

The averaged V_H is described as the follow,

$$V_H = \frac{V_{24}+V_{42}+V_{13}+V_{31}}{8} \quad (2.26)$$

If the V_H is positive, the polarity of the carriers is positive, that is, P-type. In the V_H is negative, the polarity of the carriers is negative, meaning N-type.[12-15] The carrier concentration can be determined by substituting V_H into equation (2.20). The carrier mobility can be determined by substituting V_H into equation (2.21).

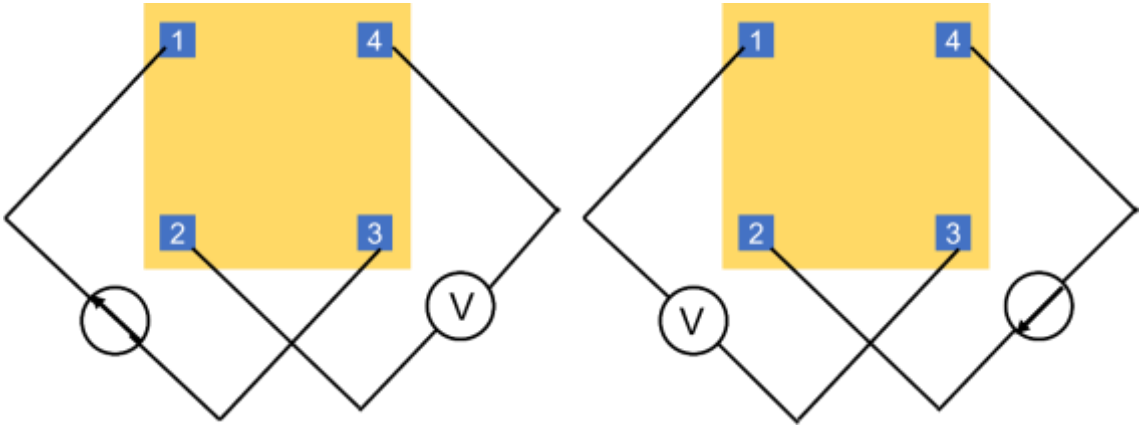

Figure 2.8. Van der Pauw method for measurements of Hall voltage.

2.2.3 Photoelectron spectroscopy (PES)

PES is a powerful technique that is widely used to study the elemental composition, chemical states, and electronic structures of atoms, molecules, and various materials.[18-20] Since PES is based on the photoelectric effect, electrons are ejected from a material when a photon is irradiated. It was first observed by Heinrich Hertz in 1887.[21] In 1905, Albert Einstein provided a rigorous explanation of the photoelectric effect using the quantum hypothesis of light. Later, in 1922, the Nobel Prize in Physics was awarded to Albert Einstein.[22]

The working principle of PES is as follows. When the energy of an incident photon is larger than the sum of the electron binding energy (E_b) and the work function of the material (φ), the electron is excited to a higher energy state above the vacuum energy level. This is called as the photoelectron. The photoelectron with kinetic energy (E_k) is given by the following equation,[23,24]

$$E_k = h\nu - E_b - \varphi \quad (2.27)$$

where hν represents the incident photon energy.[22] The photoelectron spectrum is usually

shown as binding energy, E_b.

PES can be used to determine the chemical states of materials at different depths, according to the different kinetic energies of the photoelectrons. As the excited photoelectron travels to the sample surface, inelastic scattering occurs, losing the energy of the electron.[23,25] This causes the inelastic background of the PES spectra, which is typically observed in PES.[23]

The inelastic mean free path (IMFP) of the electron is typically the order of nanometers. Therefore, PES is a relatively surface-sensitive method. Figure 2.9 shows the IMFP as a function of electron energy for the elements. The minimum IMFP is a few Å at electron energies around 50-100 eV because plasmon loss occurs in this energy range.[18-20] In order to obtain accurate IMFP, the TPP-2M formula developed by Tanuma et al. is usually used.[26]

According to the Beer-Lambert law, the intensity decay of the photoelectrons can be expressed as below,[27]

$$I(x) = I_0 e^{(\frac{-x}{\lambda})} \tag{2.28}$$

where I(x) is the photoelectron intensity at depth x, I_0 is the intensity of the photoelectron at the surface, x is the depth, and λ is the IMFP. The information depth of PES is defined as a = 3λ, where 95% of all signals contribute.[28]

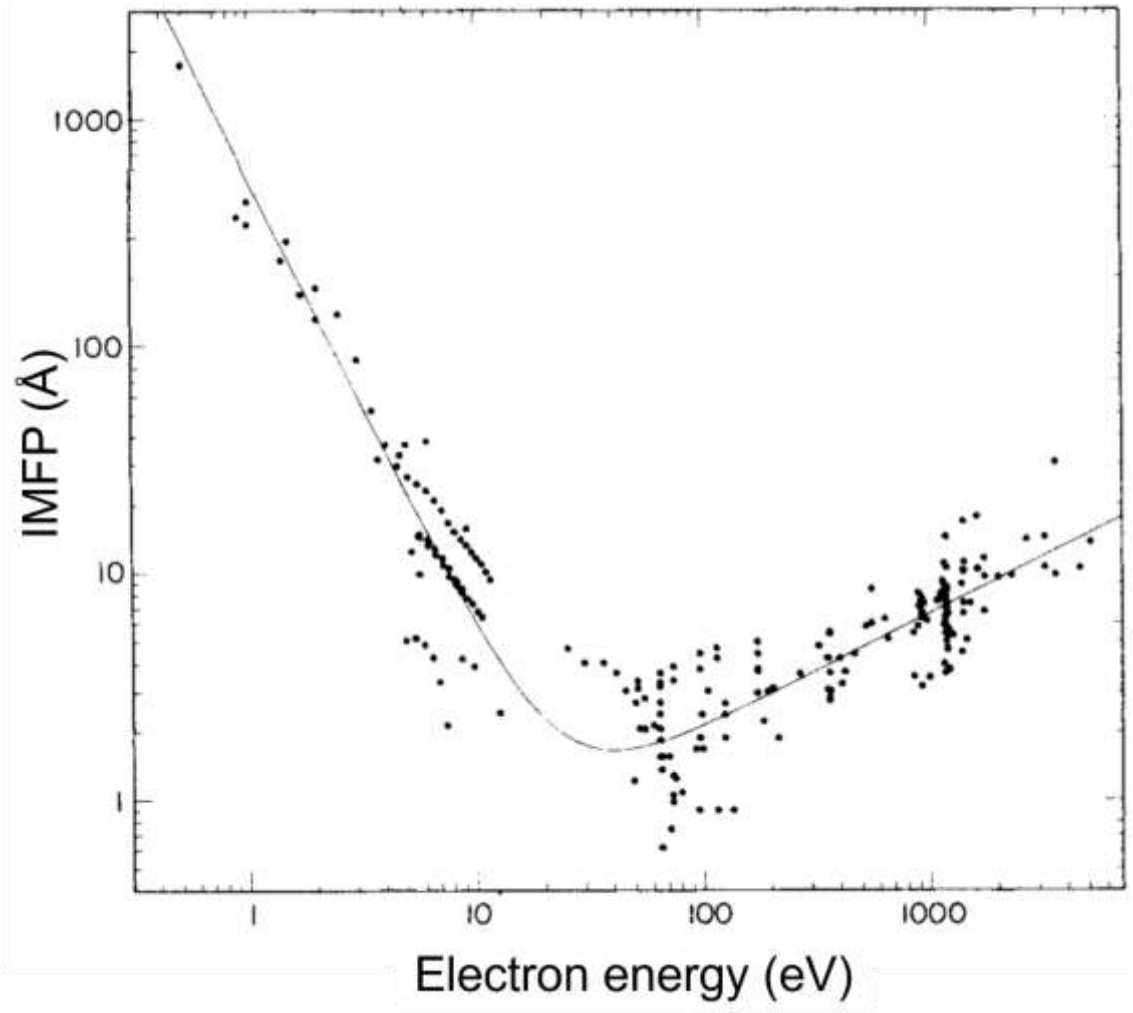

Figure 2.9. Inelastic mean free path (IMFP) as a function of electron kinetic energy.[27]

The PES measurement was first developed by K. Siegbahn et al. in 1956.[29] For PES, the chemical environment of the atom could be estimated from the binding energy of core levels.[29] Hence, Siegbahn named this technique as electron spectroscopy for chemical analysis (ESCA). Since x-ray is used, it is also called as x-ray photoelectron spectroscopy (XPS).[29] K. Siegbahn was awarded the Nobel Prize in Physics in 1981.[30] XPS provides the information on the valence band and the core-levels of elements for materials qualitatively. XPS measurements require an ultra-high vacuum (UHV) environment (< 10^{-8} mbar) to avoid the discharge of the electron analyzer.[25] Typical x-ray sources are Al Kα and Mg Kα, whose energies are 1486.6 and 1253.6 eV, respectively. The IMPF of XPS is several nm, thus it is a relatively surface-sensitive method.[23] The incident x-ray energy can be tuned using a synchrotron radiation source.[25] Figure 2.10 shows the apparatus used in the present study.

Figure 2.10. Photo of apparatus for XPS. The inset shows the electron analyzer inside the chamber.

XPS provides the binding energies of core levels, which depend on the elements and the chemical environment. Thus, XPS can be used to determine the elemental compositions as well as the nature of their local chemical environments. As shown in Fig. 2.11(a), the survey spectrum for Sn-doped Ga_2O_3 before the surface cleaning treatment exhibits several core-level peaks, such as Ga 3*p*, Sn 3*d*, and O 1*s* peaks, indicating that the elemental information of the materials can be obtained. Figure 2.11(b) shows the O 1*s* core-level spectrum for Sn-doped Ga_2O_3 before the surface cleaning treatment. The O 1*s* core-level spectrum can be decomposed into two oxygen components. These components are attributed to different oxidation states. Since the difference in binding energy is due to a different chemical environment, the energy difference is called a chemical shift.[31]

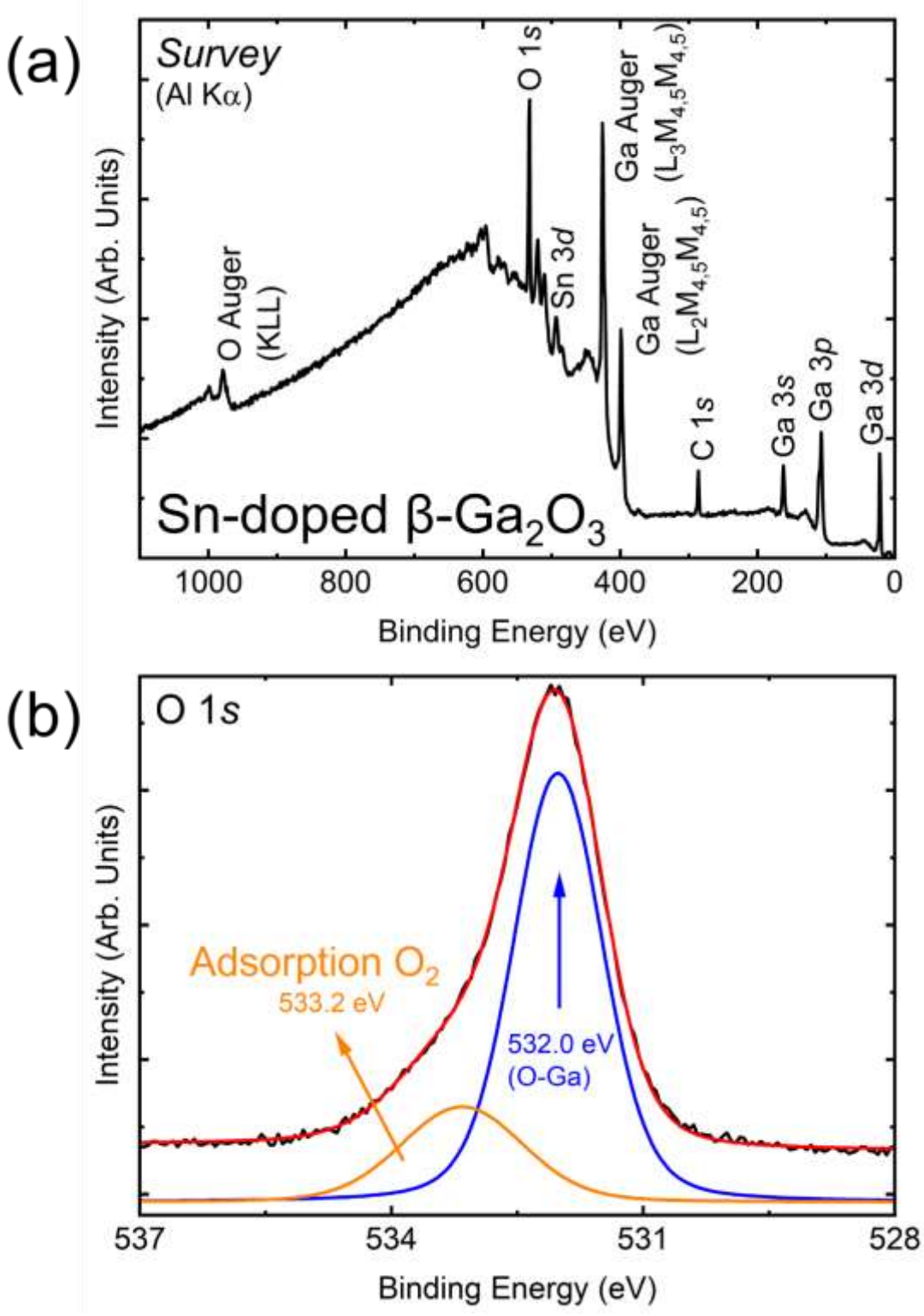

Figure 2.11. (a) Survey XPS spectrum of Sn-doped Ga_2O_3 before the surface cleaning treatment and (b) O 1*s* core level spectrum of Sn-doped Ga_2O_3 before the surface cleaning treatment.

Element quantification analysis by XPS can be performed by determining the areal intensity of a photoelectron peak (I_x) and the sensitivity factor (S_x) of an element x, which is described as,[32]

$$S_x = C\sigma_x\lambda(E_k)AT(E_k) \tag{2.29}$$

where C is the constant, σ_x is the cross section of photoionization for element x, $\lambda(E_k)$ is the IMFP of the electron kinetic energy E_k, A is the analysis sample area, and $T(E_k)$ is the transmission function of the XPS analyzer for the electron kinetic energy E_k. Under the assumption in which the photon flux is fixed and the sample is uniform, the atomic percentage of elements (or species) can be calculated. The concentration of an element, N_x, is described as,[24,32]

$$I_x = N_x S_x \tag{2.30}$$

where I_x is the photoelectron intensity.

Hard x-ray photoelectron spectroscopy (HAXPES) is a bulk-sensitive method due to its large IMFP. Typical hard x-ray energy is from 2 to 10 keV.[25,33] For HAXPES, a high-brilliance source based on third-generation synchrotron radiation (SR) is widely used to measure the electronic states of bulks and interfaces of various materials.[19] Figure 2.12 shows IMFPs as a function of kinetic energy (KE) for several materials. At the KE of 6 keV, the IMFPs are 4 to 15 nm, which is almost five times larger than those at 1 keV (typical XPS).[19] The large probing depth of HAXPES exhibits the electronic states of the bulk without surface influence. Note that the laboratory HAXPES was recently realized.[33] In the present study, Cr Kα source (5414.9 eV) was used as hard x-ray source, and the source is equipped with the XPS apparatus shown in Fig. 2.10.

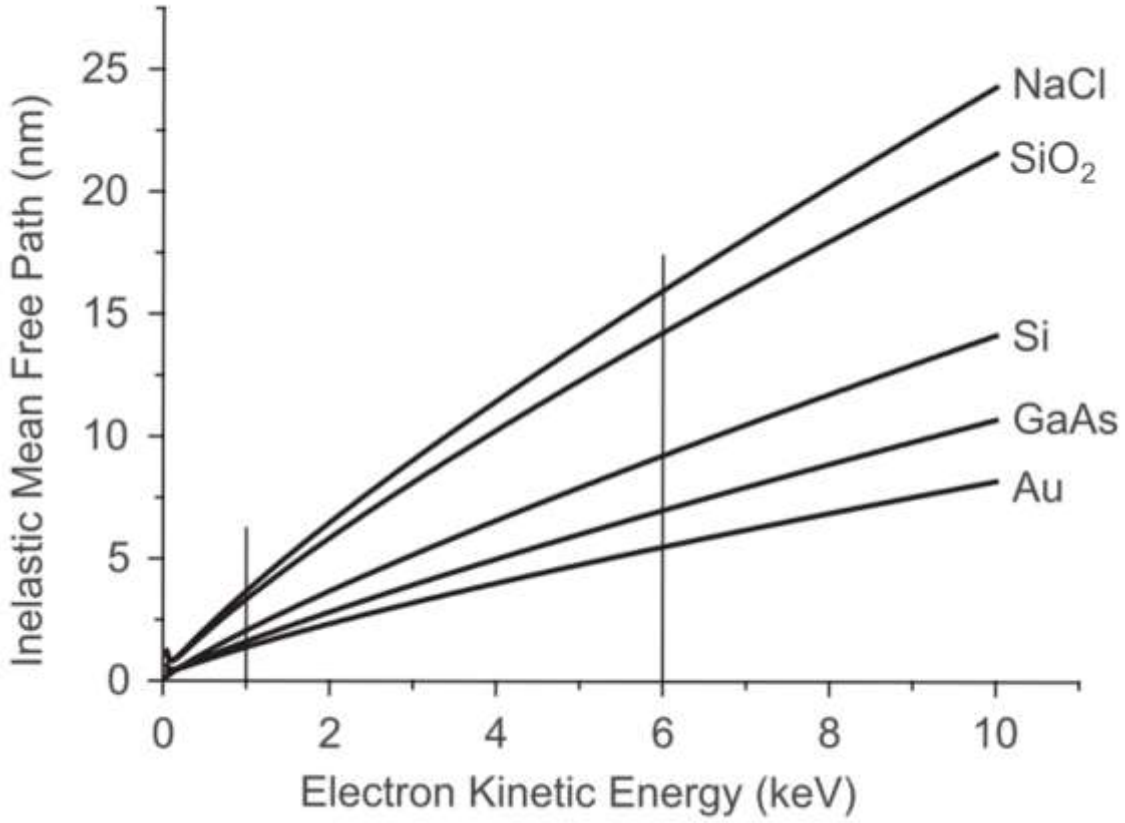

Figure 2.12. IMFPs as a function of electron kinetic energy.[19]

2.2.4 Photoelectron holography (PEH)

Photoelectron holography (PEH) is based on PES. Thus, PEH has the great advantages as follows. Since PEHs are based on the PES, chemical-discriminated PEHs can be performed. In addition, non-periodic atomic structures can be employed in the PEHs. Because the IMFP is small (typically a few nm for solids), the local atomic structure near the surface can be obtained.[34-37]

The process of PEH formation is described in Fig. 2.13. The photoelectrons of the target atoms (e.g., dopants) are excited as emitters under photoirradiation, and then the photoelectron wave emitted by a target atom is scattered by the surrounding atoms. Finally, interference patterns are formed in the photoelectron angular distribution. Because it is a hologram, the three-dimensional (3D) atomic arrangement around the photoelectron emitter atom can be reconstructed. Since the binding energies depend not only on the atom but also on the surrounding atoms, PEHs can reveal the local atomic structure around the target atom.[34-36,38,39]

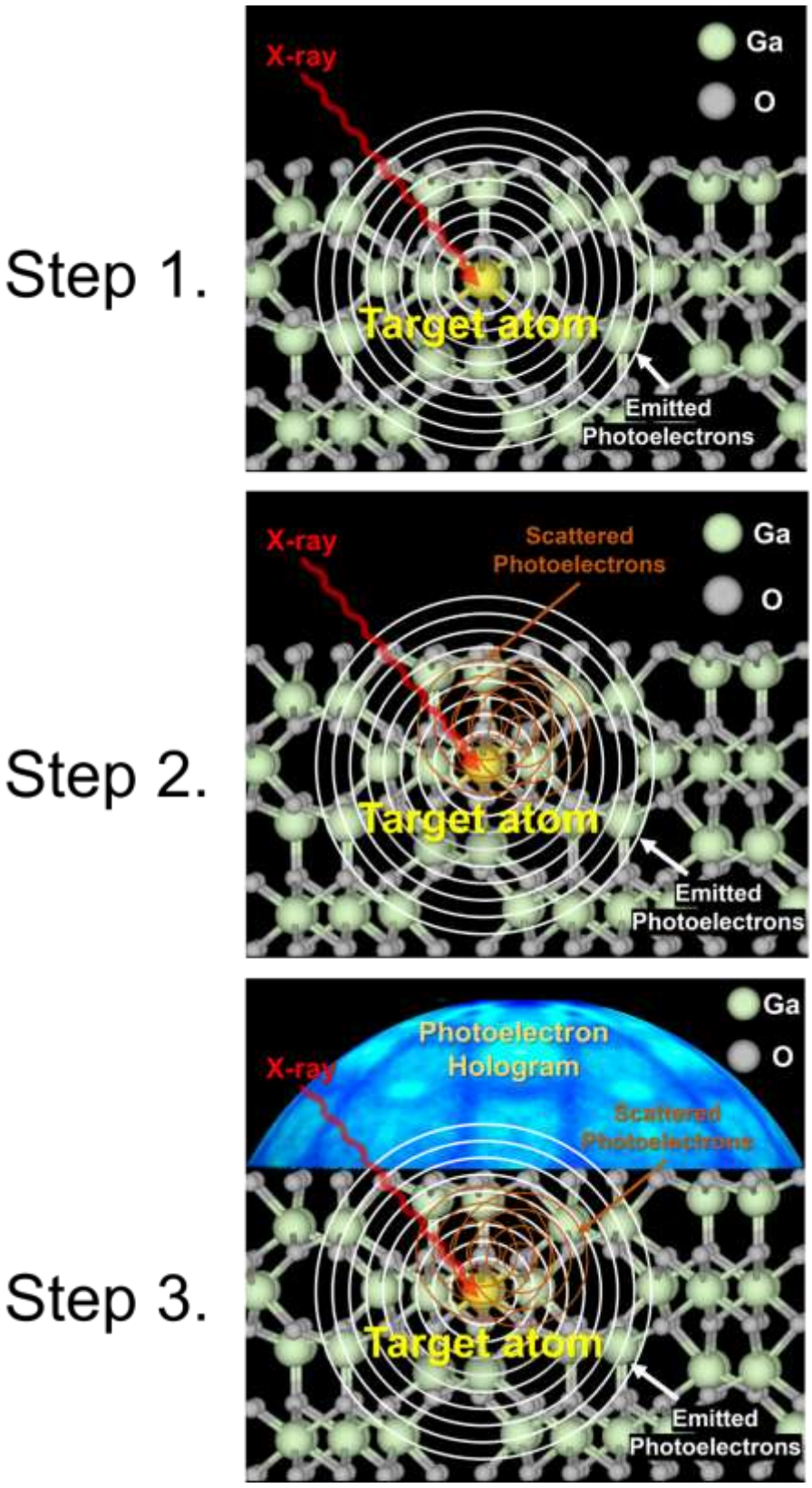

Figure 2.13. The principles of PEH process.

To obtain the PEHs, a display-type analyzer was used in the present study. This analyzer is a retarding field analyzer (RFA) with relatively high energy resolution and wide acceptance angles.[39,40] The schematic of the RFA is shown in Fig. 2.14(a). The RFA contains three spherical grids that act as high-pass filters for the photoelectrons. The highest energy resolution is approximately 0.5 eV.[38] The display-type electron energy analyzer provides a solid angle of ±49° and an angular resolution of 0.5°. The RFA was developed and installed at BL25SU in SPring-8 for PEH experiments.[40] Figure 2.14(b) shows the RFA at the BL25SU at SPring-8 used for the PEH experiments in this study.

In order to reproduce the local atomic structures from the PEH, the simulated PEHs are necessary. In the present thesis, the total analysis multiple scattering pattern (TMSP) simulation code in the 3D-AIR-IMAGE software developed by Matsushita et al. was used to reproduce the experimental holograms. The simulation is based on the partial wave expansion for spherical waves and contains multiple scattering effects.[34,41,42] The simulated PEH reproduces the experimental PEH well using the 3D-AIR-IMAGE software.[42]

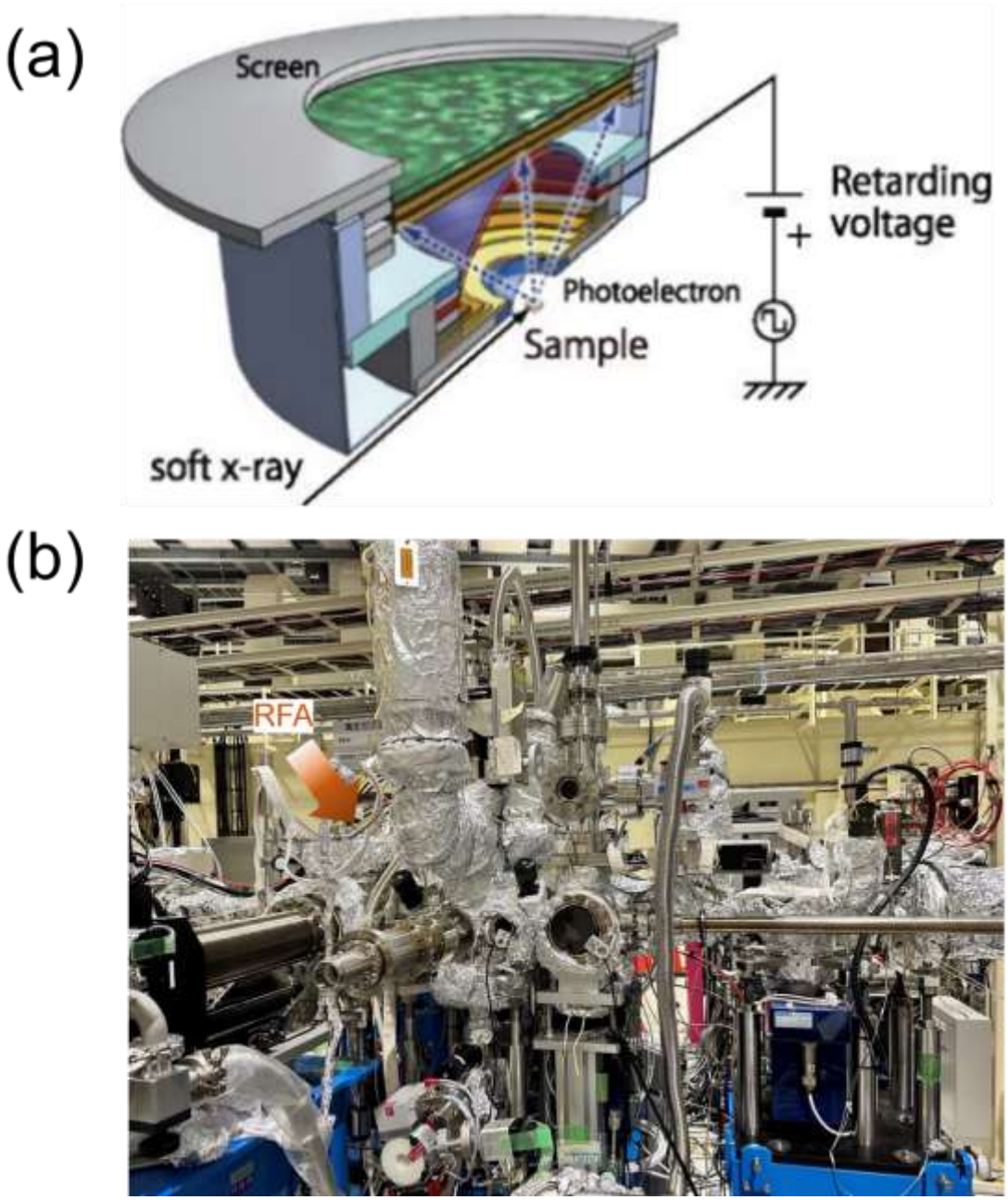

Figure 2.14. (a) Schematic of RFA.[39] (b) Photo of the RFA at BL25SU in SPring-8.

2.2.5 X-ray absorption

When an x-ray with an initial intensity (I_0) penetrates material, the x-ray intensity is decreased exponentially by the absorption coefficient, μ. The intensity, I(t), the thickness, t, and the initial intensity, I_0, are given by the Lambert-Beer law as follows (Fig. 2.15(a)),[43-45]

$$I(t) = I_0 e^{-\mu(E)t} \tag{2.31}$$

The μ shows the probability of x-ray absorption in a material. The probability depends on the electron density ρ, the atomic number Z, the atomic mass A, and the energy of the incident x-ray E, which is described as the following equation,[46]

$$\mu(E) \approx \frac{\rho Z^4}{AE^3} \tag{2.32}$$

When the incident photon is absorbed, the energy is used to excite an electron to an unoccupied or continuum state from a core level.[44] When the incident photon energy is equal to the energy difference between the core level and the unoccupied state, the absorption coefficient is suddenly increased, which is called as the absorption edge.[44,45] Figure 2.15(b) shows the absorption coefficient as a function of energy.

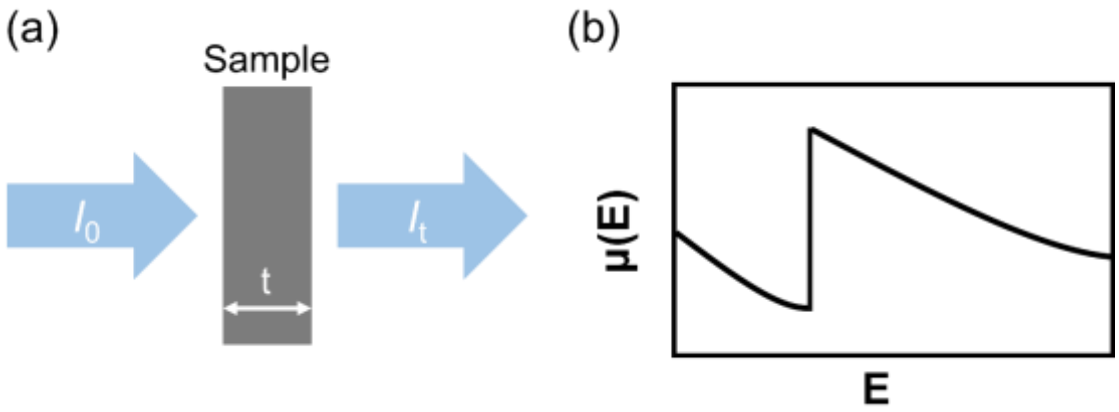

Figure 2.15. (a) X-ray intensity before and after absorption in the case of sample thickness t, and (b) absorption coefficient as a function of energy, μ(E).

For x-ray absorption measurements, a synchrotron radiation source is usually used as the x-ray source.[45,46] Figure 2.16 shows three main types of yield for x-ray absorption measurements; transmission yield (Fig. 2.16(a)), fluorescence yield (Fig. 2.16(b)) and electron yield (Fig. 2.16(c)).[43]

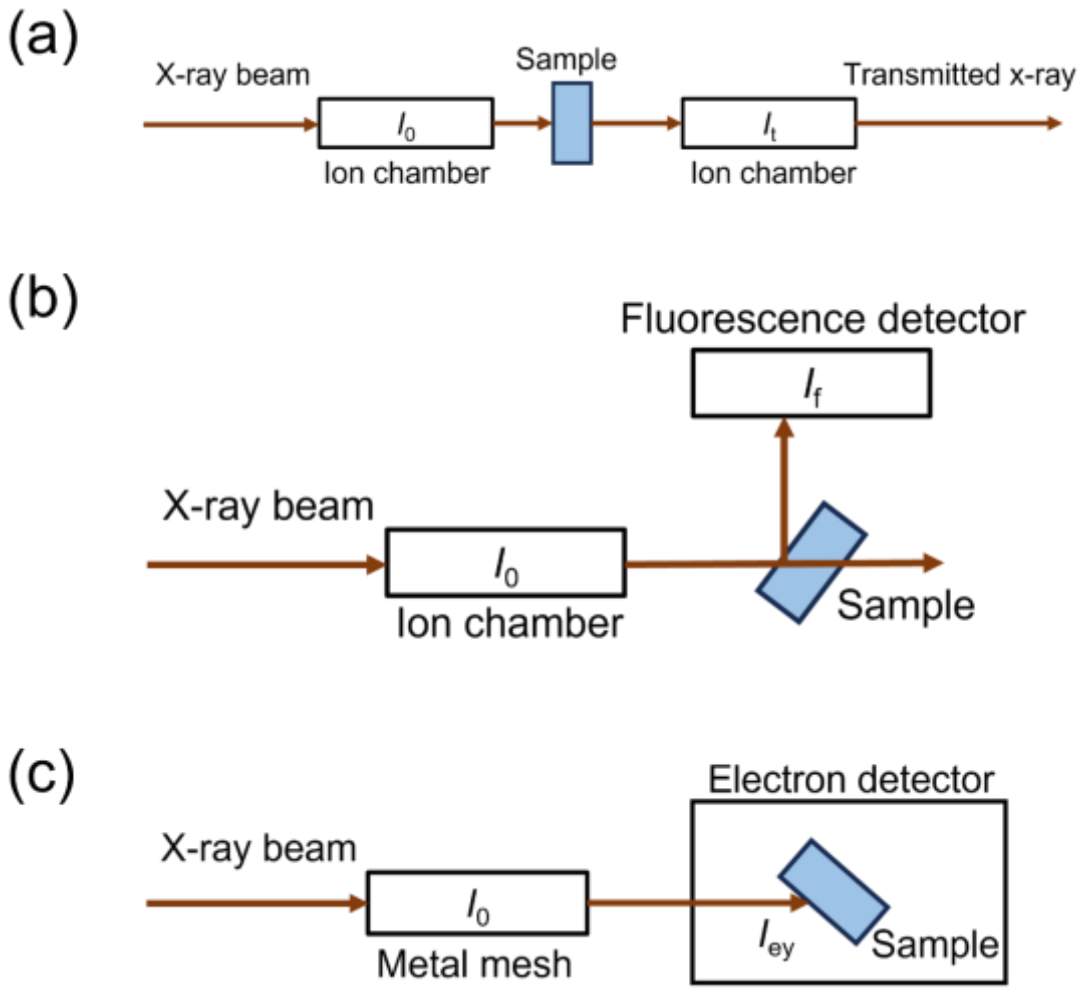

Figure 2.16. Experimental setup for the (a) transmission yield, (b) fluorescence yield, and (c) electron yield in x-ray absorption measurement.

The transmission yield is used when the incident x-ray energy is high.[43] In this yield, the intensity of the transmitted x-ray, I_t, is measured by the drain current in the ion chambers. The μ(E) is determined by the equation (2.31). The transmission yield is ideal for highly concentrated and uniform samples.[43,45]

Fluorescence yield is a powerful method for measuring low-concentration elements, solutions, and ultrathin layers.[47] The detection concentration limit of fluorescence yield (detection limit ~10^{-4} at%) is several orders of magnitude lower than that of the transmission yield (detection limit ~5 at%).[48] However, the fluorescence method is not suitable for light elements due to its low fluorescence probability.[43,45,48] The I_f in fluorescence yield is measured by a solid-state detector (typically Si and Ge).[43] The relationship between the absorption coefficient and I_f can be expressed as follows,[44]

$$\mu(E) \propto \frac{I_f}{I_0} \tag{2.33}$$

The electron yield is often used to probe the surface region because the information depth of the electron yield is around 10 nm.[49,50] A relatively high vacuum is usually needed when using soft x-rays as the incident photon.[51] There are two common methods of electron yields; partial electron yield (PEY) and total electron yield (TEY). For the PEY, an electron detector is used to detect electrons in a specific energy range. For TEY, the drain current of the sample is usually measured.[50,52] Auger electron yield (AEY) is a type of PEY. AEY is detected with the Auger electrons in a specific Auger energy range.[52] For the detection of AEY, an electron analyzer is usually used.[53] The relationship between the absorption coefficient, the initial intensity I_0, and the measured I_{ey} is given by,[54]

$$\mu(E) \propto \frac{I_{ey}}{I_0} \tag{2.34}$$

Under x-ray excitation, an electron from an inner core level is excited, forming a core hole at the core level.[55] There are two kinds of decay processes for the core hole; radiative and non-radiative, namely fluorescence and Auger electron decay processes, respectively.[56,57] Fluorescence and Auger processes are competitive. The probability of the fluorescence (Auger) decay process is increased (decreased) as the atomic number is increased.[57] The probability of fluorescence and Auger decay processes for *K* shell as a function of atomic number is shown in Fig. 2.17. For lighter elements, the Auger electron decay process is dominant, whereas the fluorescence decay process is dominant in the case of heavier elements.[58]

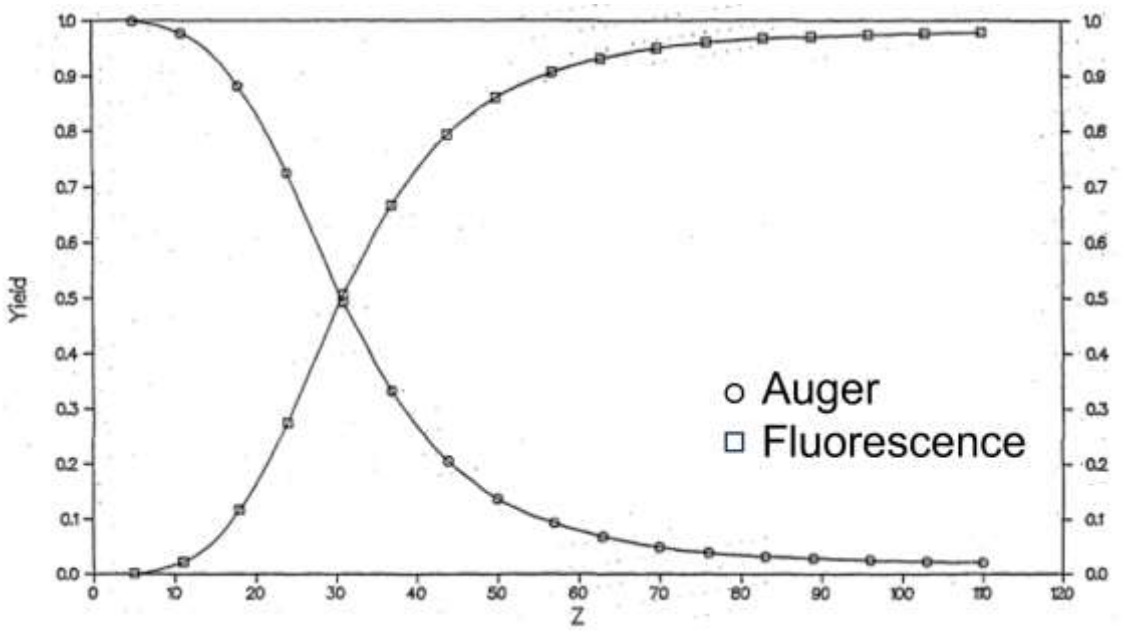

Figure 2.17. The probability of fluorescence and Auger yields for *K* shell as a function of atomic number.[58]

2.2.5.1 X-ray absorption fine structure (XAFS)

X-ray absorption fine structure (XAFS) is a method for studying the local geometric structure of a specific atom in a sample. XAFS experiments are typically performed using synchrotron radiation facilities. Elements with extremely low concentrations (≤ 1 at%) are possible to detect.[46,59] The XAFS is divided into two regions depending on the absorption energy range; the x-ray absorption near edge structure (XANES) and the extended x-ray absorption fine structure (EXAFS). For XANES, the energy range is within 50 eV above the absorption edge.[59,60] For EXAFS, the energy range is about 50 eV to 1000 eV above the absorption edge.[46,59,60] Figure 2.18 shows the typical energy range of XANES and EXAFS in the XAFS. (Sn K-edge of Sn-doped β-Ga_2O_3 as an example)

In the present study, XAFS measurements were performed at the BL22XU in the SPring-8 and the BL6N1 in the Aichi Synchrotron Radiation Center (Aichi SR). Figure 2.19 shows the photos of apparatuses at BL22XU (SPring-8) and BL6N1 (Aichi SR).

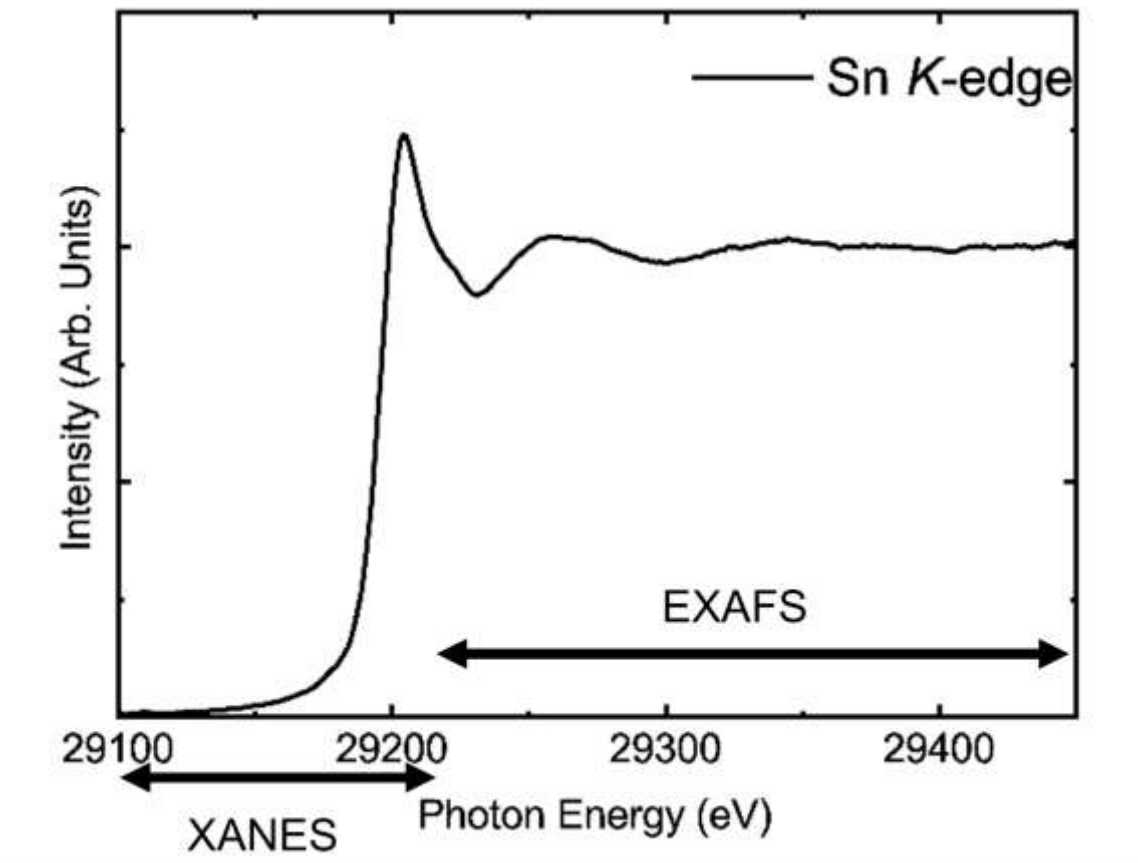

Figure 2.18. Sn K-edge XANES and EXAFS energy regions for Sn-doped β-Ga_2O_3.

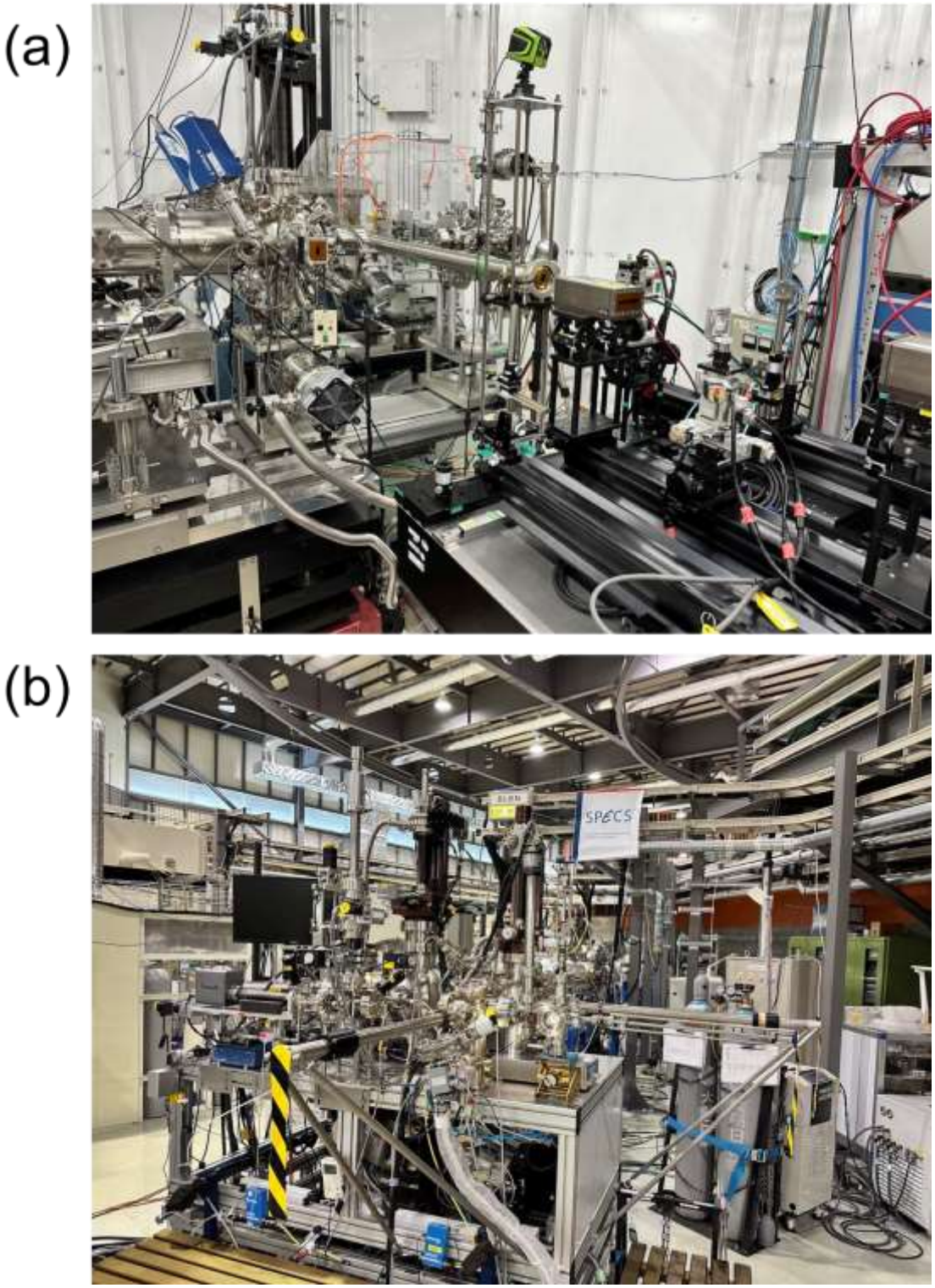

Figure 2.19. Photos of the XAFS stations at (a) BL22XU at the SPring-8 and (b) BL6N1 at the Aichi SR.

2.2.5.2 X-ray absorption near edge structure (XANES)

In XANES, the energy region is relatively close to the absorption edge. XANES is able to provide information about the unoccupied electronic state of the absorbing element, which can study the chemical state, such as the oxidation state. Therefore, XANES is widely used to study oxide materials, dopants, catalysis, etc.[43,59-61] The XANES process is shown in Fig. 2.20(a). Figure 2.20(b) shows V K-edge XANES, showing the different oxidation states of V compounds.[61]

XANES simulations can be used to clarify local atomic structures.[62-65] FEFF was used in the present thesis for the XANES simulations.[63,66,67] The software version of FEFF employed in this thesis is FEFF9.[63,66]

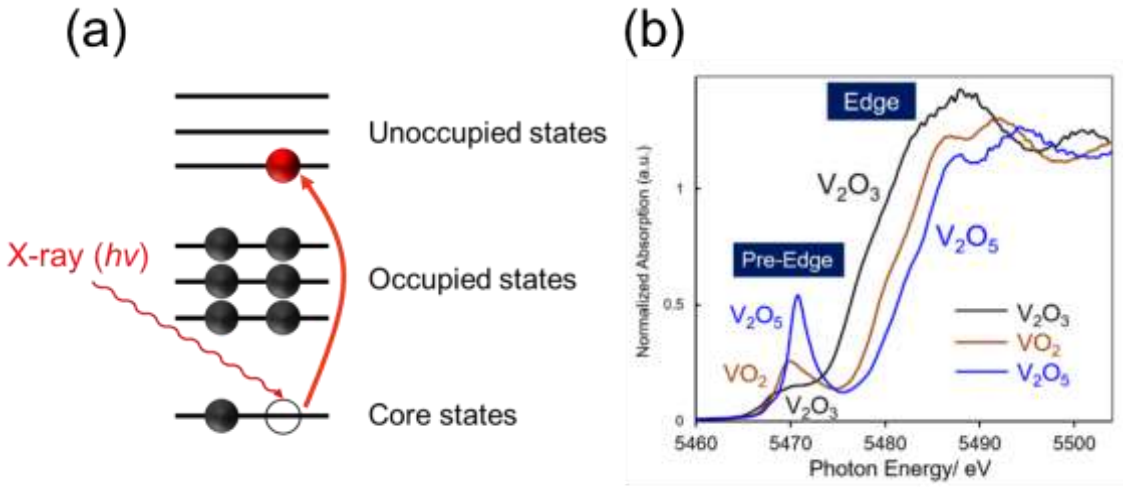

Figure 2.20. (a) Electronic structure after x-ray absorption. (b) V K-edge XANES of V compounds.[61]

2.2.5.3 Extended X-ray absorption fine structure (EXAFS)

EXAFS provides bulk and nanoscale structures for solid, gas and liquid phases of chemical and biological systems.[68,69] The spectrum structure of EXAFS is formed by electron scattering between the absorbing atom and the surrounding atoms. The outgoing electron wave from the absorbing atom travels to the neighboring atom and is backscattered by its incoming wave. EXAFS reveals chemical species, bond distances, and coordination numbers around the neighboring atoms.[43,46,60,69]

The oscillation of EXAFS, $\chi(E)$, is typically shown as a function of the wavenumber $\chi(k)$, which is a summation of the individual contributions $\chi_i(k)$ of the backscattered wave. It is described follow,[43,59,69]

$$\chi(k) = S_0^2 \sum_i N_i F_i(k) e^{-2\sigma_i^2 k^2} e^{\frac{-2R_i}{\lambda(k)}} \frac{\sin[2kR_i + \delta_i(k)]}{kR_i^2} \quad (2.35)$$

where S_0^2 is the overall amplitude reduction factor coming from many-body effects, N_i is the coordination number, $F_i(k)$ is the backscattering amplitude of the photoelectron, σ_i^2 is the Debye-Waller factor, $\lambda(k)$ is the photoelectron mean free path, $\delta_i(k)$ is the photoelectron phase shift,

k^2 is described as follow,[43,59,69]

$$k^2 = \frac{2m_e(E - E_0 + \Delta E_0)}{\hbar} \quad (2.36)$$

where k is wavenumber, ħ is the Planck constant, m_e represents the mass of electron, and E_0 is the theoretical energy of the absorption edge, $\Delta E_0$is the energy difference of photoelectron used to align the E_0 with the measured EXAFS spectrum.

R_i is described as follow,

$$R_i = R_{0_i} + \Delta R_i \quad (2.37)$$

where R_i is the distance between the neighboring atoms,[59,69] ΔR_i is bond length difference relative to the calculated bond length R_{0_i}.

The EXAFS oscillation's magnitude is dependent on the N_i and S_0^2 parameters, which are independent of the k value. The Debye-Waller factor is a dynamic effect of thermal fluctuations. This factor is also affected by the structural disorder for the difference phase. The $\sin[2kR_i + \delta_i(k)]$ term is for the EXAFS oscillation. The $2kR_i$ term relates to the phase shift of the neighboring atoms at distance R_i. The $\delta_i(k)$ term is the phase shift caused by the absorbing atom nuclei interaction with the surrounding atoms in scattering paths.[69]

For the EXAFS data processing, the normalization, the background removal, and the Fourier transformation (FT) of the EXAFS oscillation were performed using *ATHENA* software in the present thesis.[70-72]

To obtain the chemical species, bond distances, and coordination numbers around the neighboring atoms, the EXAFS data fitting was performed using the *ARTEMIS* software in the present thesis.[70-72].

References

1. A. Kuramata, K. Koshi, S. Watanabe, Y. Yamaoka, T. Masui, and S. Yamakoshi, *Japanese Journal of Applied Physics* **55**, 1202A2 (2016).
2. M.J. Tadjer, J.A. Freitas, J.C. Culbertson, M.H. Weber, E.R. Glaser, A.L. Mock, N.A. Mahadik, K. Schmieder, E. Jackson, J.C. Gallagher, B.N. Feigelson, and A. Kuramata, *Journal of Physics D: Applied Physics* **53**, 504002 (2020).
3. A. Hernandez, M.M. Islam, P. Saddatkia, C. Codding, P. Dulal, S. Agarwal, A. Janover, S. Novak, M. Huang, T. Dang, M. Snure, and F.A. Selim, *Results in Physics* **25**, 104167 (2021).
4. P. Mazzolini, Z. Fogarassy, A. Parisini, F. Mezzadri, D. Diercks, M. Bosi, L. Seravalli, A. Sacchi, G. Spaggiari, D. Bersani, O. Bierwagen, B.M. Janzen, M.N. Marggraf, M.R. Wagner, I. Cora, B. Pécz, A. Tahraoui, A. Bosio, C. Borelli, S. Leone, and R. Fornari, *Advanced Functional Materials* **33**, 2207821 (2022).
5. A. Parisini, A. Bosio, V. Montedoro, A. Gorreri, A. Lamperti, M. Bosi, G. Garulli, S. Vantaggio, and R. Fornari, *APL Materials* **7**, 031114 (2019).
6. V. der H. Paul, *Secondary Ion Mass Spectrometry: An Introduction to Principles and Practices*, 1st ed. (John Wiley & Sons, Hoboken, New Jersey, 2014).
7. B. Saha and P. Chakraborty, *Energy Procedia.* **41**, 80 (2013).
8. M. Takeuchi, *Plant Morphology* **26**, 19 (2014).
9. Q. Li, J. Chang, L. Li, X. Lin, and Y. Li, *Science of The Total Environment* **905**, 167257 (2023).
10. T. Stephan, *Planetary and Space Science* **49**, 859 (2001).
11. P. Peres, S. Choi, F. Desse, P. Bienvenu, I. Roure, Y. Pipon, C. Gaillard, N. Moncoffre, L. Sarrasin, and D. Mangin, *Journal of Vacuum Science & Technology B* **36**, 03F117 (2018).
12. M. S. Luz, C. A. M. Santos, C. Y. Shigue, F. J. H. Carvalho Jr, and A. J. S. Machado, *Materials Science-Poland* **27**, 569 (2009).
13. L.J. van der Pauw, *Philips Research Reports* **13**, 1 (1958).
14. G. Rietveld, Ch.V. Koijmans, L.C.A. Henderson, M.J. Hall, S. Harmon, P. Warnecke, and B. Schumacher, *IEEE Transactions on Instrumentation and Measurement* **52**, 449 (2003).
15. H. Castro, J. Galvis, and S. Castro, *IEEE Transactions on Instrumentation and Measurement* **60**, 198 (2011).
16. S. Thirumavalavan, K. Mani, and S.S. Sagadevan, *Journal of Nano- and Electronic Physics* **7**, 04024 (2015).
17. S.M. Sze and M. K. Lee, *Semiconductor Devices: Physics and Technology*, 3rd ed. (John Wiley & Sons, Central Area, Singapore, 2013).
18. F. Reinert and S. Hüfner, *New Journal of Physics* **7**, 97 (2005).
19. Y. Takata, M. Yabashi, K. Tamasaku, Y. Nishino, D. Miwa, T. Ishikawa, E. Ikenaga, K. Horiba, S. Shin, M. Arita, K. Shimada, H. Namatame, M. Taniguchi, H. Nohira, T. Hattori, S. Södergren,

B. Wannberg, and K. Kobayashi, *Nuclear Instruments and Methods in Physics Research Section A: Accelerators, Spectrometers, Detectors and Associated Equipment* **547**, 50 (2005).
20. K. Horiba, *Hyomen Kagaku* **28**, 698 (2007).
21. J.F. Mulligan, *Physics Today* **42**, 50 (1989).
22. A.B. Arons and M.B. Peppard, *American Journal of Physics* **33**, 367 (1965).
23. S. Hüfner, *Photoelectron Spectroscopy: Principles and Applications*, 3rd ed. (Springer Berlin, Heidelberg, Baden-Württemberg, 2013).
24. F.A. Stevie and C.L. Donley, *Journal of Vacuum Science & Technology A: Vacuum, Surfaces, and Films* **38**, 063204 (2020).
25. C.M. Schneider, in *Scattering methods for condensed matter research: towards novel applications at future sources; lecture notes of the 43rd IFF Spring School 2012*, edited by M. Angst, T. Brücker, D. Richter, and R. Zorn (Forschungszentrum Jülich, Jülich, 2012), pp. 2–39.
26. S. Tanuma, C.J. Powell, and D.R. Penn, *Surface and Interface Analysis* **43**, 689 (2011).
27. M.P. Seah and W.A. Dench, *Surface and Interface Analysis* **1**, 2 (1979).
28. C.R. Brundle and B.V. Crist, *Journal of Vacuum Science & Technology A* **38**, 041001 (2020).
29. K. Siegbahn and K. Edvarson, *Nuclear Physics* **1**, 137 (1956).
30. J.M. Hollander and D.A. Shirley, *Science* **214**, 629 (1981).
31. H. Hantsche, *Scanning* **11**, 257 (1989).
32. C.D. Wagner, L.E. Davis, M.V. Zeller, J.A. Taylor, R.H. Raymond, and L.H. Gale, *Surface and Interface Analysis* **3**, 211 (1981).
33. S. Siol, J. Mann, J. Newman, T. Miyayama, K. Watanabe, P. Schmutz, C. Cancellieri, and L.P.H. Jeurgens, *Surface and Interface Analysis* **52**, 802 (2020).
34. T. Matsushita, F. Matsui, H. Daimon, and K. Hayashi, *Journal of Electron Spectroscopy and Related Phenomena* **178–179**, 195 (2010).
35. K. Tsutsui, T. Matsushita, K. Natori, T. Muro, Y. Morikawa, T. Hoshii, K. Kakushima, H. Wakabayashi, K. Hayashi, F. Matsui, and T. Kinoshita, *Nano Letters* **17**, 7533 (2017).
36. J. Tang, S. Takeuchi, M. Tanaka, H. Tomita, Y. Hashimoto, T. Nagata, J. Chen, T. Ohkochi, Y. Kotani, T. Matsushita, and Y. Yamashita, *ACS Applied Electronic Materials* **4**, 4719 (2022).
37. F. Matsui, T. Matsushita, and H. Daimon, *Journal of the Physical Society of Japan* **87**, 061004 (2018).
38. T. Matsushita, Y. Hashimoto, H. Tomita, Z. Sun, S. Kawamura, M.N. Fujii, and J. Mizuno, *e-Journal of Surface Science and Nanotechnology* **21**, 183 (2023).
39. R. Horie, T. Matsushita, S. Kawamura, T. Hase, K. Horigane, H. Momono, S. Takeuchi, M. Tanaka, H. Tomita, Y. Hashimoto, K. Kobayashi, Y. Haruyama, H. Daimon, Y. Morikawa, M. Taguchi, and J. Akimitsu, *Inorganic Chemistry* **62**, 10897 (2023).

40. T. Muro, T. Ohkochi, Y. Kato, Y. Izumi, S. Fukami, H. Fujiwara, and T. Matsushita, *Review of Scientific Instruments* **88**, 123106 (2017).
41. T. Matsushita, T. Muro, T. Yokoya, K. Terashima, Y. Kato, H. Matsui, N. Maejima, Y. Hashimoto, and F. Matsui, *Physica Status Solidi (b)* **257**, 2000117 (2020).
42. M.N. Fujii, M. Tanaka, T. Tsuno, Y. Hashimoto, H. Tomita, S. Takeuchi, S. Koga, Z. Sun, J.I. Enriquez, Y. Morikawa, J. Mizuno, M. Uenuma, Y. Uraoka, and T. Matsushita, *Nano Letters* **23**, 1189 (2023).
43. C.S. Schnohr and M.C. Ridgway, *X-Ray Absorption. Spectroscopy of Semiconductors*, 1st ed. (Springer Berlin, Heidelberg, Baden-Württemberg, 2015), pp. 1–26.
44. A.L. Ulery and R. Drees, *Methods of Soil Analysis: Part 5-Mineralogical Methods*, 1st ed. (Soil Science Society of America, Madison, Wisconsin, 2008), pp. 387–464.
45. M. Wang, L. Árnadóttir, Z.J. Xu, and Z. Feng, *Nano-Micro Letters* **11**, 47 (2019).
46. M. Giorgetti, *International Scholarly Research Notices* **2013**, 938625 (2013).
47. G. Falkenberg, G. Pepponi, C. Streli, and P. Wobrauschek, *Spectrochimica Acta Part B: Atomic Spectroscopy* **58**, 2239 (2003).
48. L. Tröger, D. Arvanitis, K. Baberschke, H. Michaelis, U. Grimm, and E. Zschech, *Physical Review B* **46**, 3283 (1992).
49. N. Isomura, T. Murai, H. Oji, T. Nomoto, Y. Watanabe, and Y. Kimoto, *Applied Physics Express* **9**, 101301 (2016).
50. N. Isomura, T. Murai, H. Oji, T. Nomoto, Y. Watanabe, and Y. Kimoto, *Japanese Journal of Applied Physics* **56**, 081301 (2017).
51. J. Kawai, S. Hayakawa, Y. Kitajima, S. Suzuki, K. Maeda, T. Urai, H. Adachi, M. Takami, and Y. Gohshi, *Proceedings of the Japan Academy, Series B* **69**, 179 (1993).
52. K. Nakanishi and T. Ohta, *Surface and Interface Analysis* **44**, 784 (2011).
53. N. Isomura, T. Nonaka, and Y. Watanabe, *R&D Review of Toyota CRDL* **50**, 11 (2019).
54. A. Erbil, G.S. Cargill III, R. Frahm, and R.F. Boehme, *Physical Review B* **37**, 2450 (1988).
55. Y. Dahman, C. Halim, O. Matos, and L. Chan, *Nanotechnology and Functional Materials for Engineers*, 1st ed. (Elsevier, Amsterdam, Noord-Holland, 2017), pp. 19–45
56. A.M. Ilyin, *Microscopy Methods in Nanomaterials Characterization*, edited by S. Thomas, R. Thomas, A.K. Zachariah, and R.K. Mishra, 1st ed. (Elsevier, Amsterdam, Noord-Holland, 2017), pp. 363–381.
57. D. Briggs and M.P. Seah, *Practical Surface Analysis*, 2nd ed. (John Wiley & Sons, Chichester, West Sussex, 1990).
58. M.O. Krause, *Journal of Physical and Chemical Reference Data* **8**, 307 (1979).
59. M. Newville, *Reviews in Mineralogy and Geochemistry* **78**, 33 (2014).

60. J. Cheng, W. Chu, S. Liu, P. Dong, and Z. Wu, *Journal of Superconductivity and Novel Magnetism* **27**, 9 (2013).
61. K. Nomura, *Catalysts* **9**, 1016 (2019).
62. R. Luo, J. Bao, X. Li, C. Ma, C. Du, J. Zeng, X. Xu, Z. Qian, Z. Mei, and Y. Zhou, *Small* **20**, 2304945 (2023).
63. J. Tang and Y. Yamashita, *ACS Applied Electronic Materials* **3**, 4618 (2021).
64. N. Isomura and Y. Kimoto, *Journal of Synchrotron Radiation* **28**, 1114 (2021).
65. N. Isomura, K. Kataoka, Y. Watanabe, and Y. Kimoto, *Japanese Journal of Applied Physics* **58**, 051007 (2019).
66. J.J. Rehr, J.J. Kas, F.D. Vila, M.P. Prange, and K. Jorissen, *Physical Chemistry Chemical Physics* **12**, 5503 (2010).
67. M. Ohkubo, S. Shiki, M. Ukibe, N. Matsubayashi, Y. Kitajima, and S. Nagamachi, *Scientific Reports* **2**, 831 (2012).
68. A. Filipponi, *Journal of Physics: Condensed Matter* **13**, R23 (2001).
69. B.K. Teo, *Accounts of Chemical Research* **13**, 412 (1980).
70. B. Ravel and M. Newville, *Journal of Synchrotron Radiation* **12**, 537 (2005).
71. B. Ravel and M. Newville, *Physica Scripta* **2005**, 1007 (2005).
72. B. Ravel and M. Newville, *International Tables for Crystallography* **I**, (2020).

Chapter 3 Atomic position and the chemical state of an active Sn dopant for Sn-doped β-Ga_2O_3(001)

3.1 Introduction

Recently, Ga_2O_3 gained an increase in attention as an ultra-wide bandgap semiconductor because of its bandgap of about 5 eV, high thermal stability, and the availability of large-scale Ga_2O_3 single crystal wafers.[1-3] β-Ga_2O_3 is the most thermodynamically and chemically stable among the Ga_2O_3 polymorphs.[3] β-Ga_2O_3 has two inequivalent Ga atomic sites; octahedral (Octa) and tetrahedral (Tetra) sites.[1,2] However, it is still unclear how many chemical states exist and which site is the active dopant site in Sn-doped β-Ga_2O_3. Determining the atomic structures and the chemical states of the active Sn dopant in β-Ga_2O_3 is a necessary step to obtain β-Ga_2O_3-based FETs with high performance.

In this chapter, the atomic positions and the chemical states of the active dopant sites for Sn-doped β-Ga_2O_3 were investigated using HAXPES, XANES, and EXAFS.

3.2 Experimental

The Sn-doped β-Ga_2O_3(001) single crystal was grown using the EFG method. The crystal was annealed in N_2 ambient at 1450 °C for 6 hours to reduce the residual stress in the crystal and to achieve the full activation of the donors.[3]

Sn metal foil (Nilaco Corporation), SnO powder, and SnO_2 powder (Fujifilm Wako Pure Chemical Corp.) were used as the reference samples to clarify the detailed chemical states of the Sn dopant.

SIMS was employed to measure the Sn dopant concentration as a function of depth. The CAMECA IMS-7f was used for the SIMS measurements. Cs^+ ions with 15 keV were employed as the ion source. The absolute concentration of the Sn dopant was estimated by using the reference β-Ga_2O_3 sample. Charge compensation was employed using an electron gun during the measurements.

HAXPES measurements for the reference samples (the Sn metal foil, the SnO powder, and the SnO_2 powder) were carried out using PHI Quantes (ULVAC-PHI). Monochromatic Cr Kα (5414.9 eV) was used as the incident x-ray source. The energy resolution was set to 1.11 eV. The take-off angle was 45° (the surface normal is 90°). Au film was used to estimate the Fermi level and to perform the energy calibration.

HAXPES, XANES, and EXAFS measurements were performed at BL22XU at

SPring-8.[4-7] For the HAXPES measurements on Sn-doped β-Ga_2O_3(001), the incident photon energy was 8 keV, and the energy resolution was set to 340 meV. The Scienta-Omicron EW4000 with a large acceptance angle was used as an electron analyzer.[8] The spot size at the sample position was ~30 μm × ~30 μm (horizontal × vertical) using Kirkpatrick-Baez focusing mirrors.[8] The take-off angle (TOA) was set to 89° (the surface normal is 90°). Au film was used to estimate the Fermi level and perform the energy calibration.

The Sn K-edge XANES and EXAFS measurements were carried out using the fluorescence yield (for Sn-doped β-Ga_2O_3) and the transmission yield (for the reference samples). A 19-element high-purity germanium detector (Mirion Technologies (Canberra) KK) and ionization chambers were used to measure the fluorescence and the transmission yields, respectively.[6] The spot size at the sample position was ~0.4 mm × ~0.5 mm (horizontal × vertical) for XANES and EXAFS measurements.[7] The energy range for XANES measurements was 29,150 eV to 29,300 eV with energy steps of 1.0 eV. The energy range for the EXAFS measurements was 29,000 eV to 29,480 eV with energy steps of 1.0 eV.

Note that the information depth for the HAXPES was estimated to be 7.24 nm for the reference samples and 16.23 nm for Sn-doped β-Ga_2O_3, which was estimated using the TPP-2M formula developed by Tanuma et al.,[9] whereas the information depth for the XANES and EXAFS measurements was estimated to be 3.14 μm using the Lambert-Beer law.[10]

The XANES simulations were performed using FEFF9.[11,12] In the simulations, the cluster size of ~350 atoms, full multiple scattering, a self-consistent field, and the Hedin-Lundqvist (HL) exchange-correlation potential were used. The final-state effect (Z+1 approximation) was taken into consideration.[13,14] In the simulated XANES spectra, the absorption edges were shifted by ~39 eV to correct the edge energy to the experimental value.[15-17]

3.3 Results

Figure 3.1 shows the SIMS for the Sn concentrations in Sn-doped β-Ga_2O_3. It should be noted that in the region from the surface to the depth of around 30 nm, the secondary ion yield is not stable (pre-equilibrium region).[18] Thus, the concentration is not accurate. In the depth of deeper than 30 nm, the concentration is constant (the equilibrium region). The Sn dopant concentration was estimated in the constant concentration region. Thus, the Sn dopant concentration was estimated to be 6.1×10^{18} cm^{-3}. Note that the Sn dopant concentration was also estimated by XPS; from the areal

intensity ratio of the Sn $3p_{3/2}$ and Ga $3p$ XPS spectra, the Sn dopant concentration was estimated to be 8.8×10^{18} cm^{-3}, whose value is close to the value of SIMS. The carrier concentration of the Sn dopant was estimated to be 1.2×10^{19} cm^{-3} using the electrochemical capacitance-voltage measurement.[3] Novel Crystal Technology, Inc. measured the value when purchasing the wafer.

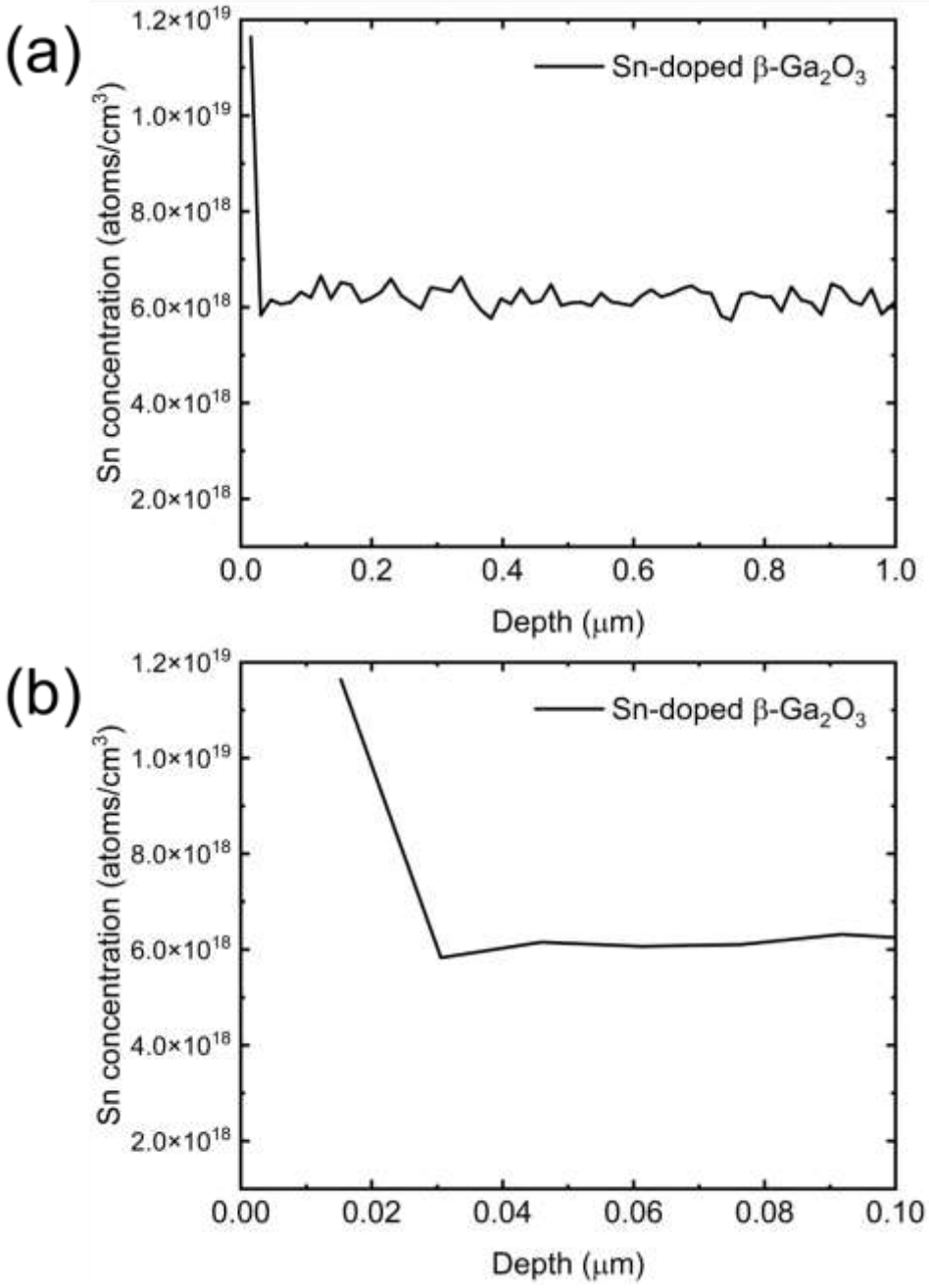

Figure 3.1. (a) SIMS for Sn dopant in Sn-doped β-Ga_2O_3. (b) Magnified the depth range (0 - 0.10 μm) of SIMS for the Sn-doped β-Ga_2O_3.

Figure 3.2 shows the Ga 2*p* HAXPES spectrum for the Sn-doped β-Ga_2O_3(001). The Voight function (convolution of Lorentzian and Gaussian functions) was used for the peak fitting.[19] For the background subtraction, the Shirley function was employed.[20,21] One symmetric peak is observed at 1119.5 eV for the Sn-doped β-Ga_2O_3(001). The peak is attributed to the Ga atom bonded with O atoms.[22,23]

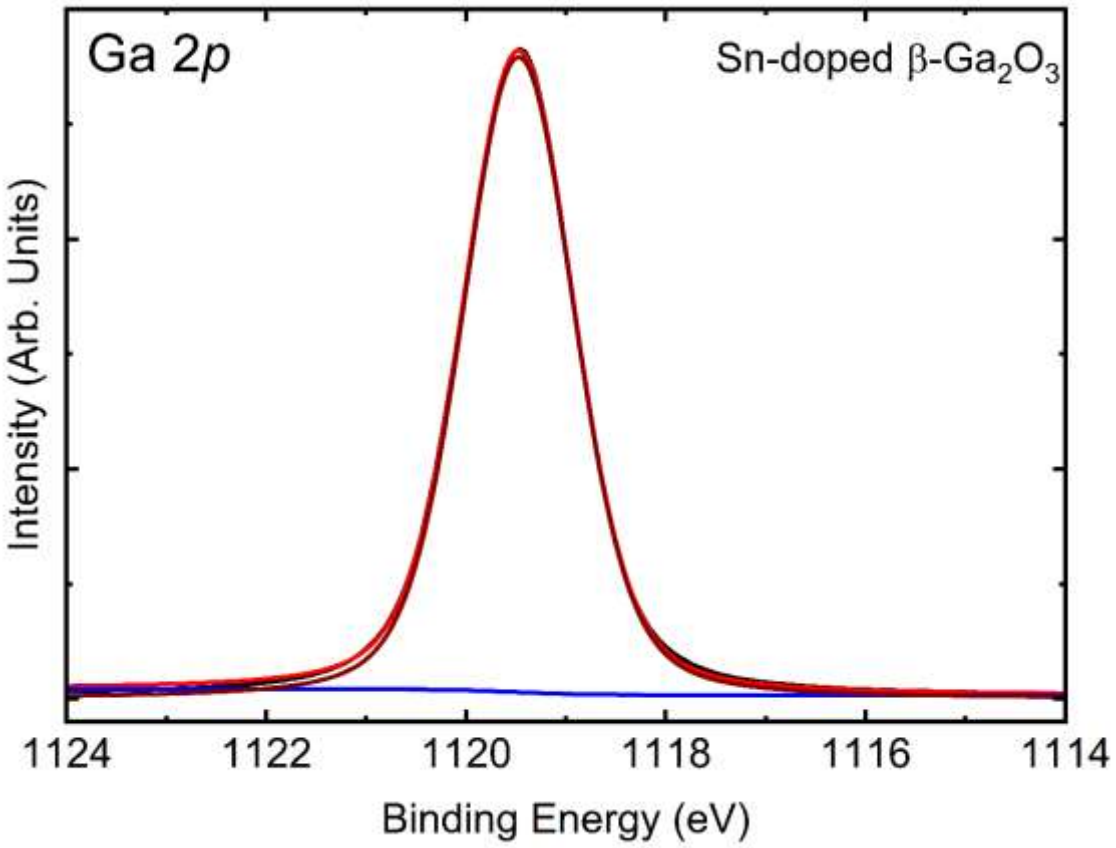

Figure 3.2. Ga 2*p* core-level HAXPES spectrum for the Sn-doped β-Ga_2O_3(001) measured at BL22XU at SPring-8. Black solid line is the experimental spectrum. Red solid line is the fitting result. Blue solid line is the Shirley background. Brown solid line is the Ga 2*p* fitting result.

Figures 3.3 (a)-(d) show the O 1*s* HAXPES spectra for the Sn-doped β-Ga_2O_3(001), the Sn metal foil, the SnO powder, and the SnO_2 powder. The Voight function (convolution of Lorentzian and Gaussian functions) was used for the peak fitting after removing the background of the Shirley function. One symmetric peak is observed at 532.6 eV for the Sn-doped β-Ga_2O_3(001) (Fig. 3.3(a)). This peak is attibuted to an oxgen atom bonded with Ga atom in β-Ga_2O_3(001) because Sn dopant

concentration is vely low (6.1×10^{18} cm^{-3}).[24] Thus, the component of O bonded with the Sn atom hardly ever contributes to the O 1*s* spectrum. For the Sn metal (Fig. 3.3(b)), no peak is observed in the O 1s HAXPES spectrum. For the SnO powder, a symmetric peak is seen at 531.0 eV (Fig. 3.3(c)). The SnO_2 powder HAXPES spectrum (Fig. 3.3(d)) shows a symmetric peak observed at 530.4 eV.

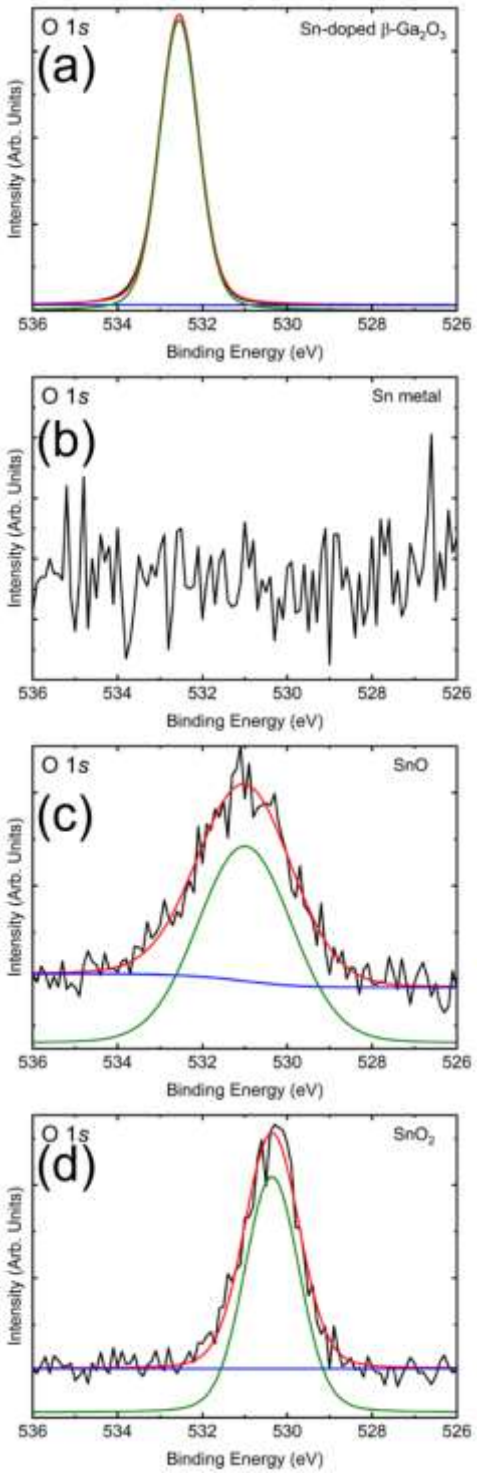

Figure 3.3. O 1*s* core-level HAXPES spectra for (a) Sn-doped β-Ga_2O_3(001), (b) Sn metal foil, (c) SnO powder, and (d) SnO_2 powder. (a) measured at BL 22XU at SPring-8. (b)-(d) measured at PHI Quantes. Black solid line is the experimental spectrum. Red solid line is the fitting result. Blue solid line is the Shirley background. Green solid line is the O 1*s* fitting result.

Figure 3.4 shows the Sn $2p_{3/2}$ HAXPES spectra for the Sn-doped β-Ga_2O_3(001), the Sn metal foil, the SnO powder, and the SnO_2 powder. The Voight function (convolution of Lorentzian and Gaussian functions) was used for the peak fitting after removing the background of the Shirley function. Note that in the case of the Sn-doped β-Ga_2O_3(001), the background structure in the Sn $2p_{3/2}$ region looks linear but not the Shirley function (Fig. 3.4(a)). This is due to the high inelastic background intensity of the core level electrons of other elements in the Sn-doped β-Ga_2O_3(001).

After the background removal in the Sn $2p_{3/2}$ HAXPES spectra, all peaks show a symmetrical peak. One peak is observed at 3932.3 eV for the Sn-doped β-Ga_2O_3(001) (Fig. 3.4(a)). In the Sn metal (Fig. 3.4(b)), a peak is observed at 3928.8 eV. For the SnO powder, a peak is seen at 3931.0 eV (Fig. 3.4(c)). The SnO_2 powder HAXPES spectrum (Fig. 3.4(d)) shows a peak at 3930.5 eV.

Since the Sn dopant for the Sn-doped β-Ga_2O_3(001), SnO powder, and SnO_2 powder exhibit a higher binding energy peak position than the Sn metal, the chemical state is attributed to an oxidation state. Note that the Sn-doped β-Ga_2O_3(001) shows a higher binding energy level than the others. Since Ga shows lower electronegatively than Sn,[25] the Sn-doped β-Ga_2O_3(001) exhibits electron-poor state compared to the SnO powder and the SnO_2 powder, shifting to a higher binding energy region. Thus, it is concluded that the peak of the Sn-doped β-Ga_2O_3(001) is attibuted to the oxdidation states. It is also noted that the SnO powder shows a higher binding energy level than the SnO_2 powder. When considering the electronegatively, the Sn atom of the SnO_2 powder exhibits a poorer electron state than that of the SnO powder, shifting to a higher binding energy level. However, the result is different. This might be due to the final state effect of the photoelectron emission process, so that the peak position of SnO has a higher binding energy than that of SnO_2.[26,27]

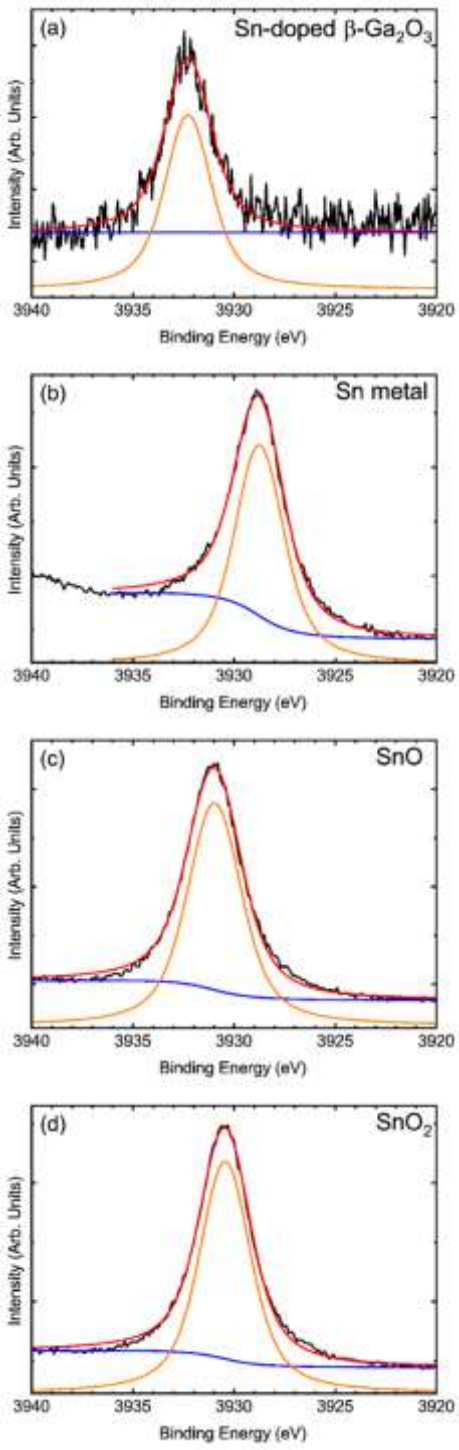

Figure 3.4. Sn $2p_{3/2}$ core-level HAXPES spectra for (a) Sn-doped β-Ga_2O_3(001), (b) Sn metal foil, (c) SnO powder, and (d) SnO_2 powder. (a) measured at BL 22XU at SPring-8. (b)-(d) measured at PHI Quantes. Black solid line is the experimental spectrum. Red solid line is the fitting result. Blue solid line is the Shirley background. Orange solid line is the Sn $2p_{2/3}$ fitting result.

Figure 3.5 shows the Sn K-edge XANES spectra for the Sn metal foil, the SnO powder, the SnO_2 powder, and the Sn-doped β-Ga_2O_3(001) before normalization.

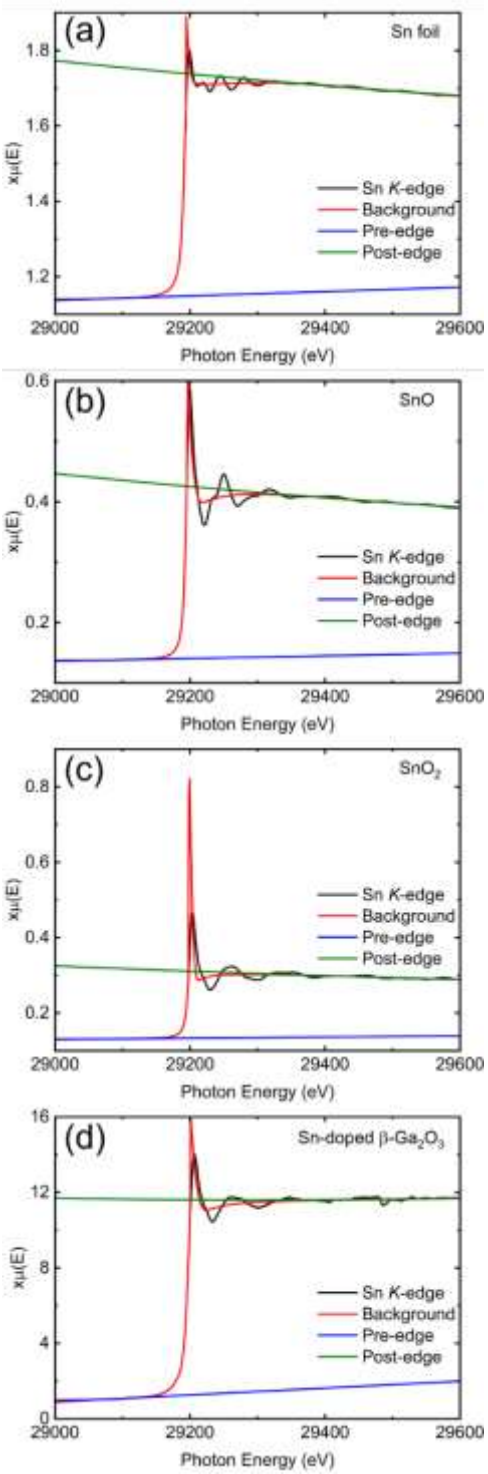

Figure 3.5. Sn *K*-edge XANES spectra before normalization of (a) Sn metal, (b) SnO, (c) SnO_2, (d) Sn-doped β-Ga_2O_3(001).

To obtain the normalized Sn K-edge XANES spectra, *ATHENA* software was used in the present study.[28-30] Before the normalization, the absorption edge position was aligned to the experimental spectrum. It is the accurate procedure to use the maximum point in the first derivative of the XANES oscillation to determine the edge position of absorption energy.[31] The pre-edge energy range was selected to create a linear function to fit the absorption coefficient before the absorption edge energy. (Blue solid line in Fig. 3.5.) Then, the post-edge line was determined. It was then fitted to the absorption coefficient after the absorption edge energy. (Green solid line in Fig. 3.5.) Then the extrapolation of the pre-edge and post-edge lines was performed. Finally, the normalized XANES spectra was able to be obtained.

Figure 3.6(a) shows the Sn K-edge XANES spectra for the Sn-doped β-Ga_2O_3(001), the Sn metal foil, the SnO powder, and the SnO_2 powder after normalization. In the Sn K-edge XANES spectra, the absorption peak at ~29200 eV is due to the Sn 1*s*→ Sn 5*p* transition.[32,33] The structures observed at higher energy than the absorption edge are attributed to the multiple scattering of several atomic shells.[34] Note that the Sn K-edge spectra do not exhibit pre-edge features because the Sn 4*d* electronic states are filled.[32] Figure 3.6(b) shows the magnified absorption edge of the Sn K-edge XANES spectra for the Sn metal, the SnO powder, the SnO_2 powder, and the Sn-doped β-Ga_2O_3(001).

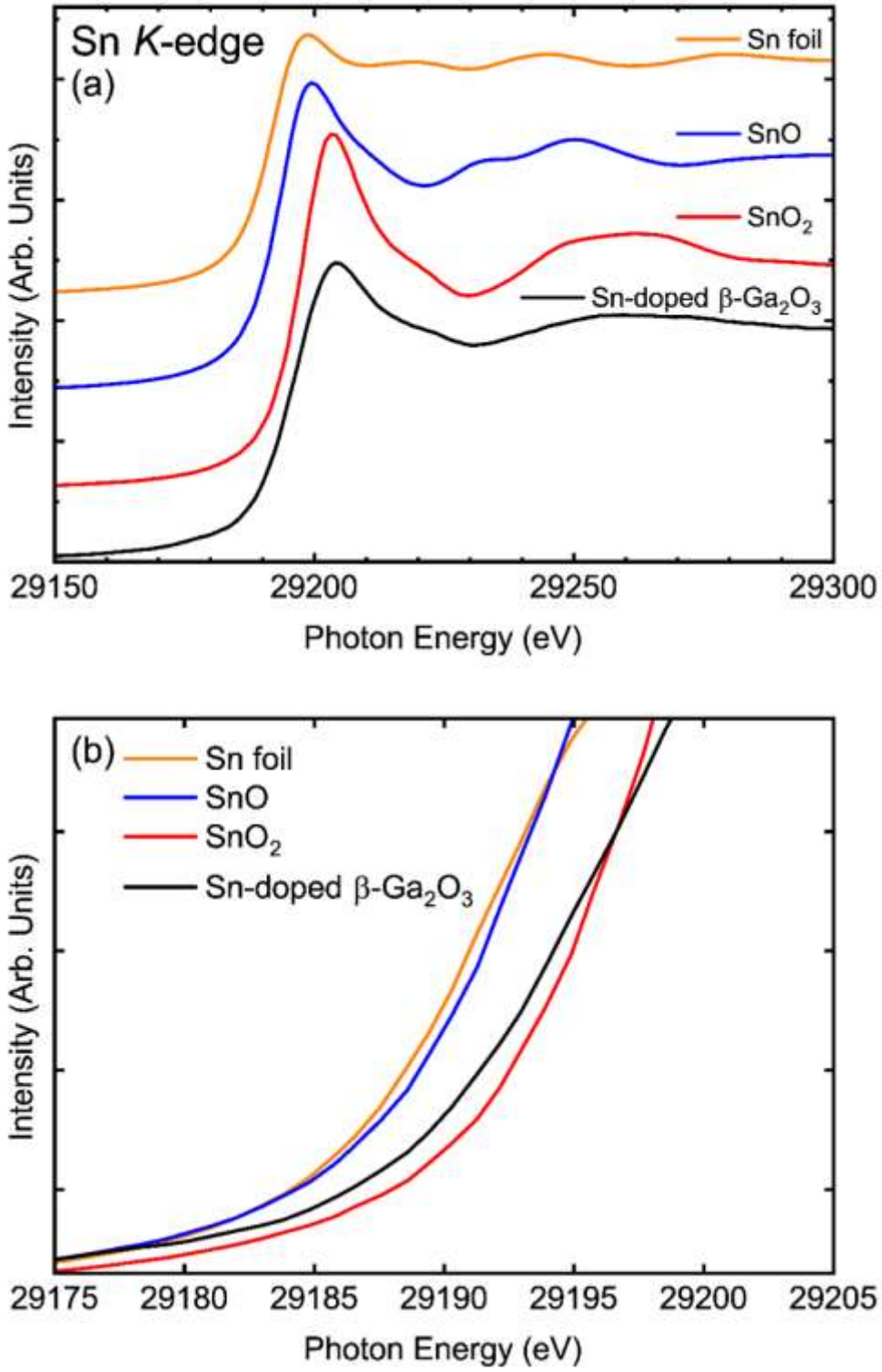

Figure 3.6. (a) Normalized Sn *K*-edge XANES spectra of Sn-doped β-Ga_2O_3(001), Sn metal, SnO, and SnO_2. (b) Magnified absorption edge of the Sn *K*-edge XANES spectra.

Figures 3.7 (a)-(d) show the first derivative peaks of the Sn K-edge XANES spectra for the Sn metal foil, the SnO powder, the SnO_2 powder, and the Sn-doped β-Ga_2O_3(001). Note that in order to estimate the edge energies, the first derivative peak of the leading edge was used.[31] The edge positions for the Sn metal, the SnO powder, the SnO_2 powder, and the Sn-doped β-Ga_2O_3(001) were estimated to be 29191.0, 29194.9, 29198.5, and 29198.0 eV, respectively.

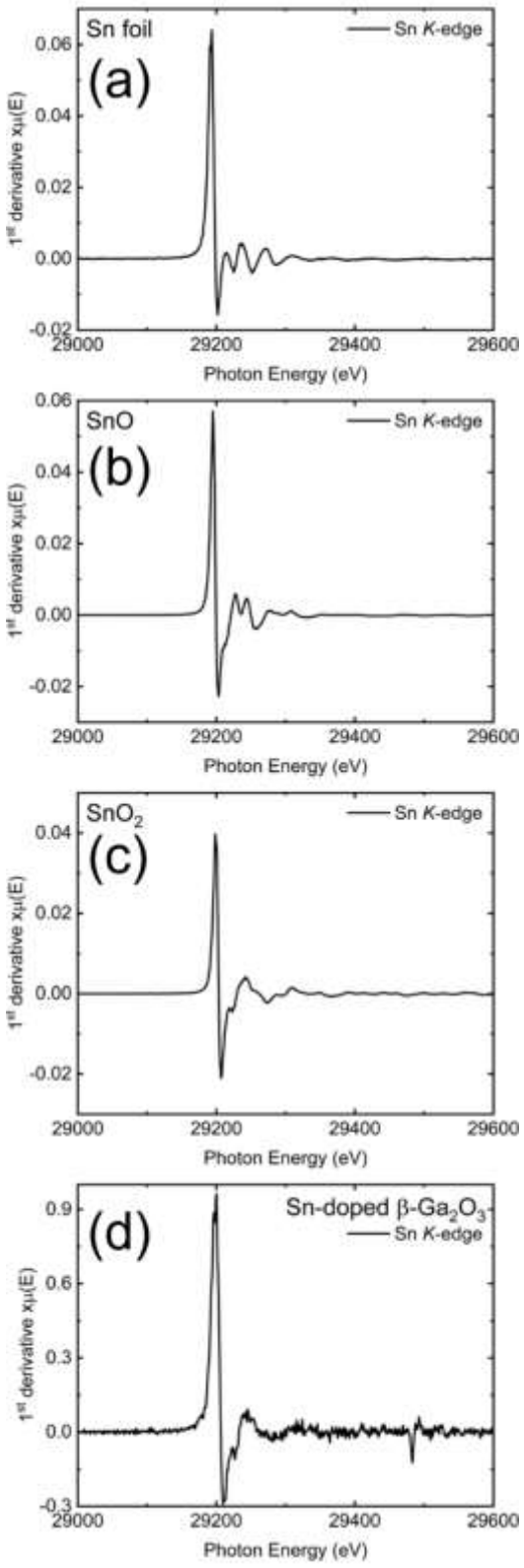

Figure 3.7. First derivative peaks of the Sn K-edge XANES spectra for (a) the Sn metal foil, (b) the SnO powder, (c) the SnO_2 powder, and (d) the Sn-doped β-Ga_2O_3(001).

Figure 3.8 shows the oxidation state as a function of the energy of the absorption edge for Sn K-edge. The liner red line was obtained from the previous studies.[35,36] The error bars were added. In the figure, the oxidation state is close to the Sn^{4+} state for the Sn-doped β-Ga_2O_3(001). Thus, the dopant Sn atom might be attributed to the tetravalent state (Sn^{4+}). Note that the Sn dopant for the Sn-doped β-Ga_2O_3(001) exhibits a little bit lower oxidation number than Sn^{4+}. This is because the Sn atom in the Sn-doped β-Ga_2O_3(001) bonds with six or four O atoms (the dopant structure)[37] exhibits a more electron-rich state than that in the SnO_2 bonds with six O atoms (the SnO_2 powder),[38] lowering the oxidation number. Thus, the Sn dopant shows a little bit lower oxidation number than Sn^{4+}. It should be also noted that from these results, the Sn dopant state in the HAXPES spectrum (Fig. 3.4(a)) is assigned to the Sn^{4+} oxidation state.

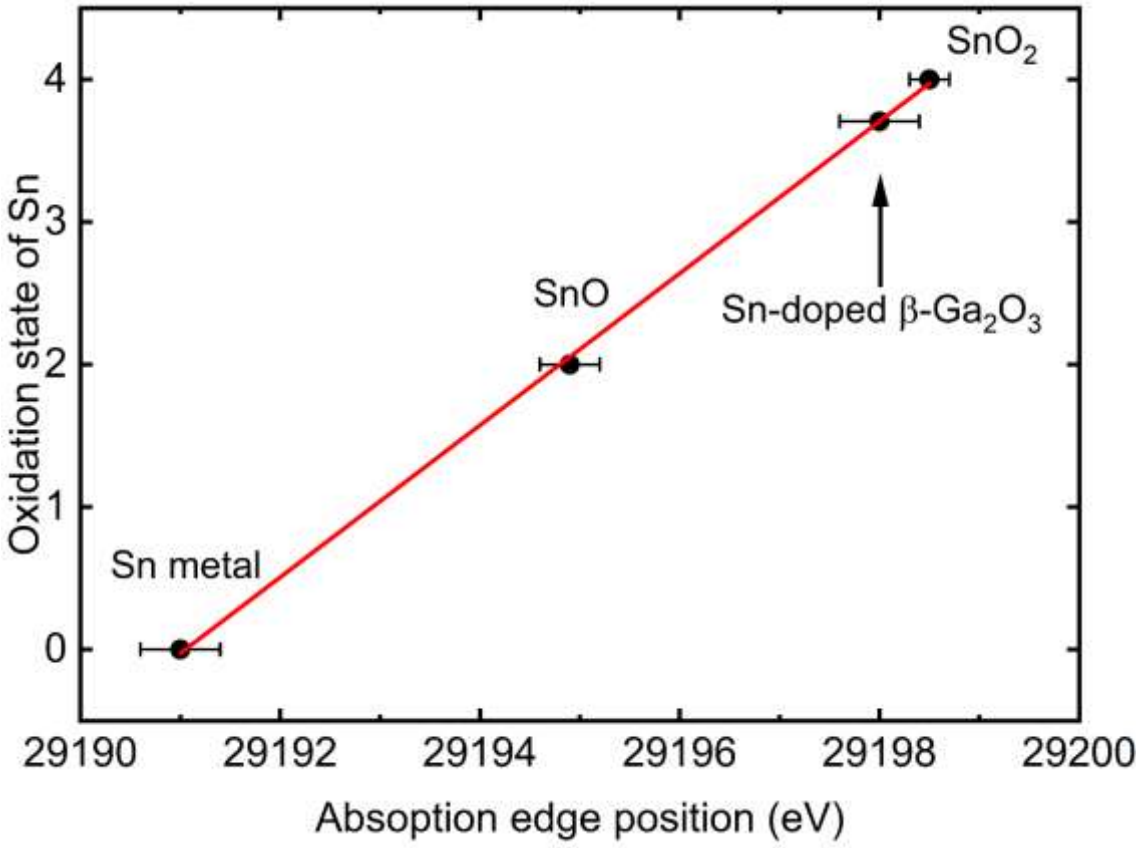

Figure 3.8. Sn oxidation state as a function of the energy of the absorption edge for Sn K-edge.

EXAFS measurements were employed to investigate the changes in the atomic

bond length of the Sn dopant for Sn-doped β-Ga_2O_3(001). Figures 3.9 (a) and (b) show the Sn K-edge XANES spectra for the Sn-doped β-Ga_2O_3(001) before (Fig.3.9(a)) and after (Fig.3.9(b)) normalization. Figure 3.9(c) shows the EXAFS oscillation for the Sn-doped β-Ga_2O_3(001). The range in the k-space was chosen at 2.5–7 $Å^{-1}$ because this range showed an adequate signal-to-noise (S/N) ratio. Figure 3.9(d) shows the Fourier transforms of the k^2-weighted EXAFS without phase shift correction. Note that since the phase shift is attributed to the scattering between the photoelectron of the absorbing atom and the neighboring atoms, shifting the amount of phase in the wave function. Thus, the peak position does not represent the real Sn-O atom distance in the Sn-doped β-Ga_2O_3(001). Figure 3.9(e) shows the Fourier transforms of the k^2-weighted EXAFS and the fitting result of the Octa Ga substitution (Sn_{Ga}) site. The fitting was performed using ARTEMIS software.[28,29] In the fitting, the reliability factor (R-factor) was set to 0.026 under k^2 weights in the 2.5–7 $Å^{-1}$ k range. The R-factor is due to the percentage of misfit. For an adequate fit, an R-factor is typically less than 0.03.[39] The fitting range was chosen at 1–2.2 Å in the r-space. The amplitude reduction factor was set to 0.8.[40] The Fourier transforms of the k^2-weighted EXAFS can be fitted well in the case of the Octa Sn_{Ga} site. On the other hand, it is unable to fit the Fourier transforms of the k^2-weighted EXAFS well in the case of the Tetra Sn_{Ga} site (Fig. 3.9(f)). The amplitude reduction factor and R-factor values for Tetra Sn_{Ga} sites was set to 0.8, 0.051. From above discussion, it is concluded that the Octa Sn_{Ga} site is the active dopant site for Sn-doped β-Ga_2O_3. Figures 3.9 (g) and (h) show the atomic structures for Octa and Tetra Sn_{Ga} in β-Ga_2O_3, respectively.

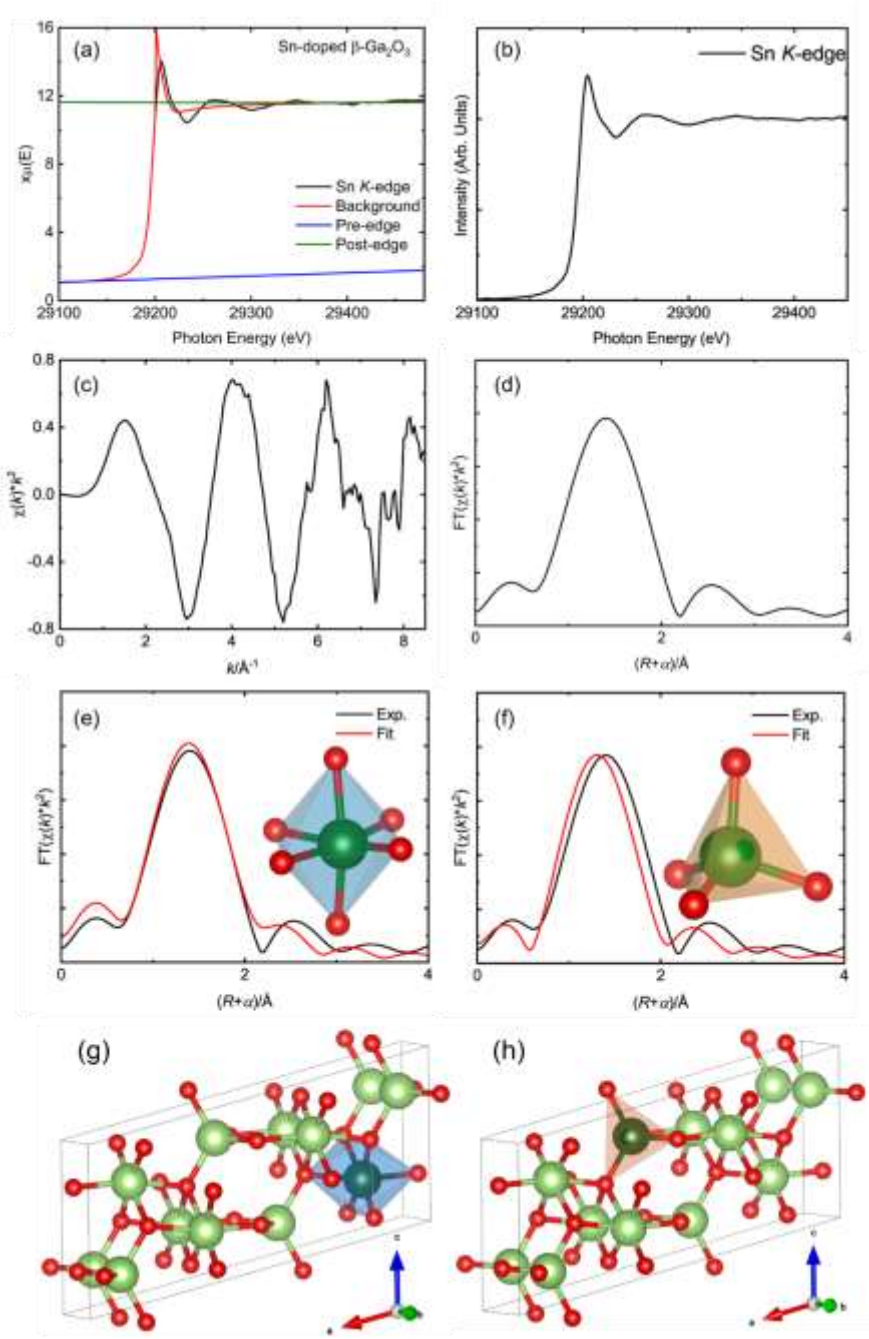

Figure 3.9. Sn *K*-edge EXAFS spectrum (a) before and (b) after normalization for Sn-doped β-Ga_2O_3(001). (c) k^2-weighted Sn *K*-edge EXAFS for Sn-doped β-Ga_2O_3(001). (d) Fourier transforms of the k^2-weighted EXAFS without phase correction. Fourier transforms of the k^2-weighted EXAFS (black solid line) and the fitting results (red solid line) for (e) Octa Sn_{Ga} site and (f) Tetra Sn_{Ga} site. The insets in Figs 3.9. (e) and (f) show local atomic structure of the Octa Sn_{Ga} and Tetra Sn_{Ga} sites, respectively. Atomic structures for (g) Octa Sn_{Ga} and (h) Tetra Sn_{Ga} in Sn-doped β-Ga_2O_3. Light green, dark green and red balls indicate Ga, Sn and O atoms, respectively.

Figure 3.10 shows the experimental (Fig. 3.10(a)) and the simulated XANES spectra using FEFF9 software[11,12] for the Octa Sn_{Ga} (Fig. 3.10(b)) and the Tetra Sn_{Ga} (Fig. 3.10(c)) sites. In the FEFF9 simulations, the many-body amplitude reduction factor was set to 1.0. The cluster size of 9.5 Å (~350 atoms) was used. The final state effect (Z+1 approximation) was employed for the simulations.[13,14]

In the experimental XANES spectrum (Fig. 3.10(a)), a main strong and sharp peak is observed at 29204.1 eV. In addition, a weak shoulder at 29221.9 eV and a broad component centered at 29252.7 eV are observed. (see arrows in Fig. 3.10(a)) For the simulated XANES spectrum for the Octa Sn_{Ga} site (Fig. 3.10(b)), a main strong sharp peak and a weak shoulder are observed at 29202.3 and 29219.5 eV, respectively. In addition, a broad component centered at 29262.1 eV is observed. (see arrows in Fig. 3.10(b)) The simulated XANES spectrum of the Tetra Sn_{Ga} site (Fig. 3.10(c)) has two broad peaks at 29204.9 and 29223.2 eV and two weak components centered at 29267.9 and 29291.1 eV. (see arrows in Fig. 3.10(c))

From the comparison of the experimental and the simulated XANES spectra, it is found that the simulated XANES spectrum of the Octa Sn_{Ga} has a similar spectrum shape to the experimental XANES spectrum for Sn-doped β-Ga_2O_3(001).

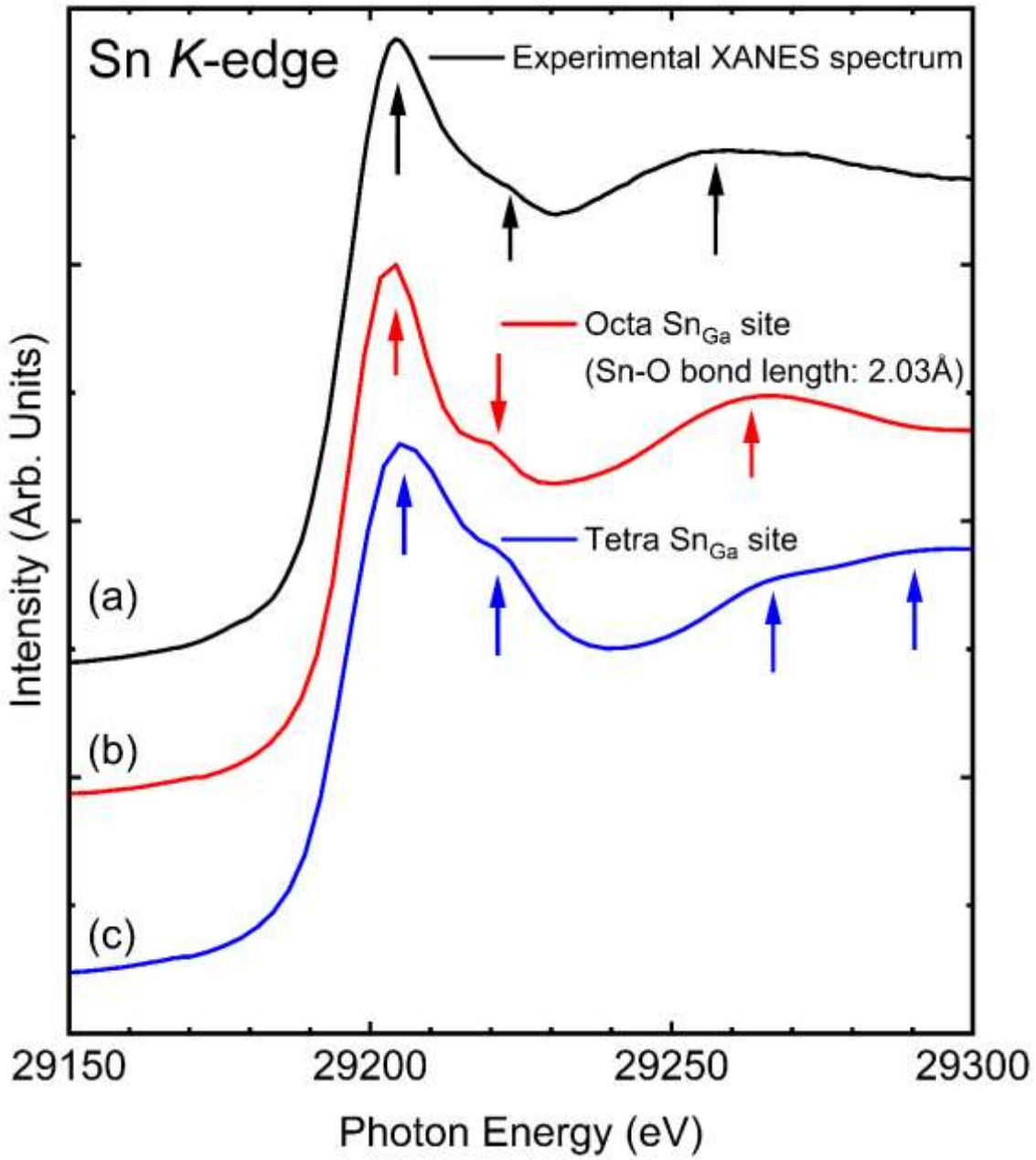

Figure 3.10. (a) Normalized Sn *K*-edge XANES spectrum for Sn-doped β-Ga_2O_3(001). The simulated XANES spectra of (b) Octa Sn_{Ga} (red line) and (c) Tetra Sn_{Ga} (blue line) sites.

Figures 3.11 shows the first derivative peaks of the Sn K-edge XANES spectra for the Sn-doped β-Ga_2O_3(001), the Octa and the Tetra Sn_{Ga} sites. The first derivative peak of the simulated Octa Sn_{Ga} XANES spectrum shows a good agreement with the experimental spectrum. On the other hand, the first derivative peak of the simulated

Tetra Sn_{Ga} XANES spectrum does not explain the experimental XANES spectrum because the simulated Tetra Sn_{Ga} XANES spectrum has two distinct peaks indicated by blue arrows in Fig. 3.11. Thus, it is concluded that the Octa Sn_{Ga} is attributed to the atomic structure of the Sn dopant site for Sn-doped β-Ga_2O_3(001).

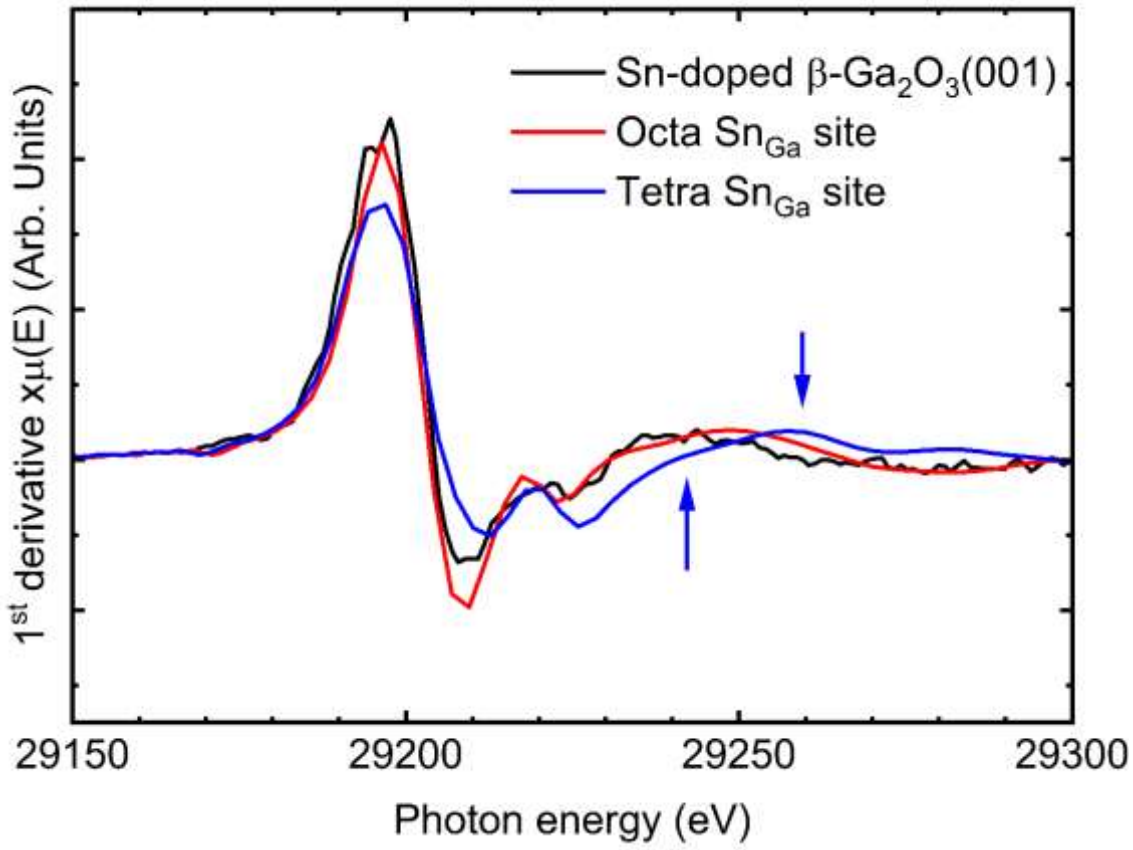

Figure 3.11. First derivative peak of the Sn K-edge XANES spectra for the Sn-doped β-Ga_2O_3(001), the Octa site and the Tetra Sn_{Ga} site.

3.4 Discussion

First of all, it is discussed why the carrier concentration exhibits higher than the Sn dopant concentration; the carrier concentration is 1.2×10^{19} cm^{-3} whereas the Sn dopant concentration is 6.1×10^{18} cm^{-3}. According to the previous studies, oxygen vacancies, H_i (hydrogen interstitial site), H_O (oxygen substitutional site), and Ga_i (Ga interstitial site) are formed in the bulk of β-Ga_2O_3.[37,41] In addition, according to the previous study, oxygen vacancy, H_i and H_O exhibit shallow donor energy levels.[41,42] When preparing the Sn-doped β-Ga_2O_3 sample, the process environment is full of N_2 gas.[3] Thus the introduction of hydrogen atoms may not be possible, excluding the

possibility of H_i and H_O formed in Sn-doped β-Ga_2O_3. Therefore, oxygen vacancy acts as unintentional donors.[3,41] Since the Octa Sn_{Ga} site shows the active dopant site in β-Ga_2O_3, the Octa Sn_{Ga} site may be fully activated (activation energy is 7.4 meV).[37,43] Therefore, it is concluded that the difference between the carrier concentration and the Sn dopant concentration is attributed to the presence of oxygen vacancies in the Sn-doped β-Ga_2O_3(001). It should be noted that metal oxide materials usually contain oxygen vacancies.[44,45]

Next, it is discussed why only the Octa Sn_{Ga} site is occupied by the Sn dopant atom in Sn-doped β-Ga_2O_3. According to the previous DFT calculations, Octa Sn_{Ga} exhibits lower formation energy than the Tetra Sn_{Ga}.[42,46] In order to estimate the ratio of the Octa and Tetra Sn_{Ga}, Maxwell-Boltzmann distribution was employed. By assuming that the ratio is determined by the Maxwell-Boltzmann distribution, the occupancy ratios for the Sn dopants can be determined. Maxwell-Boltzmann distribution equation is described as follow,[47,48]

$$\frac{N_O}{N_T} = e^{-(\frac{E_O - E_T}{kT})} \tag{3.1}$$

where N_O and N_T are the number of Octa and Tetra Sn_{Ga}, E_O and E_T are the formation energy of Octa and Tetra Sn_{Ga}. k is the Boltzmann constant, and T is the temperature. According to the DFT calculation, the formation energy difference for Octa Sn_{Ga} - Tetra Sn_{Ga} is -0.96 eV.[46] The Boltzmann constant k is 8.62×10^{-5} eV/atom·K, while T is 2073 K (the sample preparation temperature).[3] From the equation (3.1), the Octa and Tetra Sn_{Ga} ratio is estimated to be $e^{5.37} = 214$. Thus, the occupancy position is only Octa Sn_{Ga} site in Sn-doped β-Ga_2O_3.

3.5 Conclusion

HAXPES, XANES, and EXAFS were employed to clarify the chemical state and the atomic position of the Sn dopants for Sn-doped β-Ga_2O_3(001). From HAXPES, it was found that the Sn dopant shows only one chemical state. From the Sn K-edge XANES spectrum, the Sn dopant exhibited a Sn^{4+} oxidation state. From the XANES simulations and EXAFS, the atomic position of the active Sn dopant site is attributed to Octa Sn_{Ga}.

References

1. S.C. Siah, R.E. Brandt, K. Lim, L.T. Schelhas, R. Jaramillo, M.D. Heinemann, D. Chua, J. Wright, J.D. Perkins, C.U. Segre, R.G. Gordon, M.F. Toney, and T. Buonassisi, *Applied Physics Letters* **107**, 252103 (2015).
2. H. Arima-Osonoi, K. Yamazaki, R. Simura, T. Sugawara, K. Yubuta, K. Sugiyama, and A. Yoshiasa, *Journal of Crystal Growth* **570**, 126223 (2021).
3. A. Kuramata, K. Koshi, S. Watanabe, Y. Yamaoka, T. Masui, and S. Yamakoshi, *Japanese Journal of Applied Physics* **55**, 1202A2 (2016).
4. M. Kobata, T. Okane, K. Nakajima, E. Suzuki, K. Ohwada, K. Kobayashi, H. Yamagami, and M. Osaka, *Journal of Nuclear Materials* **498**, 387 (2018).
5. T. Suzuki, T. Ogata, M. Tanaka, T. Kobayashi, H. Shiwaku, T. Yaita, and H. Narita, *Analytical Sciences* **35**, 1353 (2019).
6. M. Simonnet, T. Kobayashi, K. Shimojo, K. Yokoyama, and T. Yaita, *Inorganic Chemistry* **60**, 13409 (2021).
7. T. Shobu, K. Tozawa, H. Shiwaku, H. Konishi, T. Inami, T. Harami, and J. Mizuki, *AIP Conference Proceedings* **879**, 902 (2007).
8. C. Kalha, N.K. Fernando, P. Bhatt, F. Johansson, A. Lindblad, H. Rensmo, L.Z. Medina, R. Lindblad, S. Siol, L. Jeurgens, C. Cancellieri, K. Rossnagel, K. Medjanik, G. Schönhense, M. Simon, A.X. Gray, S. Nemšák, P. Lömker, C. Schlueter, and A. Regoutz, *Journal of Physics: Condensed Matter* **33**, 233001 (2021).
9. S. Tanuma, C.J. Powell, and D.R. Penn, *Surface and Interface Analysis* **43**, 689 (2011).
10. A. Yamaguchi, N. Akamatsu, S. Saegusa, R. Nakamura, Y. Utsumi, M. Kato, I. Yagi, T. Ishihara, and M. Oura, *RSC Advances* **12**, 10425 (2022).
11. J. Tang and Y. Yamashita, *ACS Applied Electronic Materials* **3**, 4618 (2021).
12. Y. Tsai, J. Tang, and Y. Yamashita, *ACS Applied Electronic Materials* **5**, 3843 (2023).
13. I. Alperovich, D. Moonshiram, A. Soldatov, and Y. Pushkar, *Solid State Communications* **152**, 1880 (2012).
14. M. Roy and S.J. Gurman, *Journal of Synchrotron Radiation* **8**, 1095 (2001).
15. E. Bosman and J. Thieme, *Journal of Physics: Conference Series* **186**, 012004 (2009).
16. K. Nakanishi and T. Ohta, *Journal of Physics: Condensed Matter* **21**, 104214 (2009).
17. J.J. Rehr, J.J. Kas, F.D. Vila, M.P. Prange, and K. Jorissen, *Physical Chemistry Chemical Physics* **12**, 5503 (2010).
18. S. Fearn, J. Rossiny, and J. Kilner, *Solid State Ionics* **179**, 811 (2008).
19. V. Jain, M.C. Biesinger, and M.R. Linford, *Applied Surface Science* **447**, 548 (2018).
20. J. Végh, *Journal of Electron Spectroscopy and Related Phenomena* **151**, 159 (2006).
21. J.E. Castle and A.M. Salvi, *Journal of Vacuum Science & Technology A* **19**, 1170 (2001).

22. Y. Shen, H.-P. Ma, L. Gu, J. Zhang, W. Huang, J.-T. Zhu, and Q.-C. Zhang, *Nanomaterials* **12**, 4256 (2022).
23. H. Ryou, T.H. Yoo, Y. Yoon, I.G. Lee, M. Shin, J. Cho, B.J. Cho, and W.S. Hwang, *ECS Journal of Solid State Science and Technology* **9**, 045009 (2020).
24. Y. Mizokawa, H. Iwasaki, R. Nishitani, and S. Nakamura, *Journal of Electron Spectroscopy and Related Phenomena* **14**, 129 (1978).
25. J.C.A. Boeyens, *Zeitschrift Für Naturforschung B* **63**, 199 (2008).
26. E. Pehlke and M. Scheffler, *Physical Review Letters* **71**, 2338 (1993).
27. A.X. Gray, C. Papp, S. Ueda, B. Balke, Y. Yamashita, L. Plucinski, J. Minár, J. Braun, E.R. Ylvisaker, C.M. Schneider, W.E. Pickett, H. Ebert, K. Kobayashi, and C.S. Fadley, *Nature Materials* **10**, 759 (2011).
28. B. Ravel and M. Newville, *Journal of Synchrotron Radiation* **12**, 537 (2005).
29. B. Ravel and M. Newville, *Physica Scripta* **2005**, 1007 (2005).
30. B. Ravel and M. Newville, *International Tables for Crystallography* **I** (2020).
31. A.J. Berry, H.St.C. O'Neill, K.D. Jayasuriya, S.J. Campbell, and G.J. Foran, *American Mineralogist* **88**, 967 (2003).
32. E.R. Aluri and A.P. Grosvenor, *Physical Chemistry Chemical Physics* **15**, 10477 (2013).
33. H.T. Wang, M.K. Srivastava, C.C. Wu, S.H. Hsieh, Y.F. Wang, Y.C. Shao, Y.H. Liang, C.H. Du, J.W. Chiou, C.M. Cheng, J.L. Chen, C.W. Pao, J.F. Lee, C.N. Kuo, C.S. Lue, M.K. Wu, and W.F. Pong, *Scientific Reports* **7**, 40886 (2017).
34. D. Grandjean, R.E. Benfield, C. Nayral, L. Erades, K. Soulantica, A. Maisonnat, and B. Chaudret, *Physica Scripta*, 699 (2005).
35. S.T. Barlow, D.J. Bailey, A.J. Fisher, M.C. Stennett, C. Gausse, H. Ding, V.A. Krasnov, S.Y. Sayenko, N.C. Hyatt, and C.L. Corkhill, *npj Materials Degradation* **4**, 3 (2020).
36. B. Kosog, H. Pierre, M.A. Denecke, F.W. Heinemann, and K. Meyer, *Inorganic Chemistry* **51**, 7940 (2012).
37. J. Zhang, J. Shi, D. Qi, L. Chen, and K. Zhang, *APL Materials* **8**, 020906 (2020).
38. S. Das and V. Jayaraman, *Progress in Materials Science* **66**, 112 (2014).
39. Z. Chen, D.M. Chevrier, B.E. Conn, T.P. Bigioni, and P. Zhang, *The Journal of Physical Chemistry C* **127**, 20771 (2023).
40. L. Haddad, D. Gianolio, D.J. Dunstan, Y. Liu, C. Rankine, and A. Sapelkin, *Nanoscale* **16**, 5768 (2024).
41. Y. Wang, J. Su, Z. Lin, J. Zhang, J. Chang, and Y. Hao, *Journal of Materials Chemistry C* **10**, 13395 (2022).
42. J.B. Varley, J.R. Weber, A. Janotti, and C.G. Walle, *Applied Physics Letters* **97**, 142106 (2010).

43. T. Oishi, K. Harada, Y. Koga, and M. Kasu, *Japanese Journal of Applied Physics* **55**, 030305 (2016).
44. X. Pan, M.Q. Yang, X. Fu, N. Zhang, and Y.J. Xu, *Nanoscale* **5**, 3601 (2013).
45. L. Liu, Z. Mei, A. Tang, A. Azarov, A. Kuznetsov, Q.-K. Xue, and X. Du, *Physical Review B* **93**, 235305 (2016).
46. S. Lany, *APL Materials* **6**, 046103 (2018).
47. E. Kamiyama, K. Sueoka, and J. Vanhellemont, *ECS Journal of Solid State Science and Technology* **2**, P104 (2013).
48. R.H. Heist and F.K. Fong, *Physical Review B* **1**, 2970 (1970).

Chapter 4 Photoelectron Holographic Study for Atomic Site Occupancy for Si Dopants in Si-Doped κ-Ga_2O_3(001)

4.1 Introduction

For Ga_2O_3, there are six crystal polymorphs: α-, β-, δ-, γ-, ε-, and κ-Ga_2O_3.[1,2] Among them, the most thermodynamically stable is β-Ga_2O_3, which has been widely investigated.[3-6] Recently, the orthorhombic κ-Ga_2O_3 polymorph has gained attention due to its higher symmetry with respect to the monoclinic structure, its large spontaneous polarization along the (001) direction, and its ferroelectricity.[7-10] According to previous studies, this structure can be synthesized by several chemical- and physical-vapor phase epitaxial techniques (e.g., MOVPE, HVPE, MBE, and PLD) on various substrates.[11] Among them, c-plane sapphire has been so far the most frequently used substrate for κ-Ga_2O_3 epitaxy.[4,12-15]

There are three inequivalent Ga atomic sites in κ-Ga_2O_3; octahedral (Octa), pentahedral (Penta), and tetrahedral (Tetra).[8,16] For κ-Ga_2O_3, Si and Sn have been used experimentally as extrinsic donors.[4,8,13,17,18] According to electron paramagnetic resonance (EPR), Si may be attributed to an effective donor when it is positioned as a substitutional Ga site (Si_{Ga}) in the tetrahedral site.[13] In this framework, the following could all play an important role in the resulting Si dopant activation efficiency in κ-Ga_2O_3:[4] (i) the presence of a large concentration of extended defects (i.e., rotational domain boundaries and plane defects); (ii) the possible occupation of different reticular Ga sites; and (iii) the presence of a large amount of compensating defects (deep level acceptors).

In particular for points (i) and (iii), the (001)-oriented heteroepitaxy of κ-Ga_2O_3 on various substrates [e.g., c-plane sapphire, (0001)-GaN, (111)-MgO][11] results in the formation of a large density of structural defects that are perfectly vertically oriented, i.e., 3×120° rotated domains and anti-phase boundaries.[4,19,20] According to the recent work of Vyvenko et al., these vertically oriented structural defects could be electrically charged.[20] It is likely that the discrepancy between the detected level of incorporated Si in the κ-Ga_2O_3 matrix and the net doping level is in line with a high level of compensation that can be largely induced by such vertically oriented structural defects. A similar picture of large charge carrier compensation related to charged structural

defects has been reported and modeled in the case of defective β-Ga_2O_3 layers by Fiedler et al.[21]

In this chapter, the atomic positions and the chemical states of the Si dopants for Si-doped κ-Ga_2O_3 were investigated using PES, PEH, and EXAFS. Using these methods, the atomic structures of the active and inactive Si dopants for the Si-doped κ-Ga_2O_3 could be clarified. In this thesis, the 0.54% and 1.02% Si dopant atomic concentrations were selected because the 0.54% and 1.02% Si dopant atomic concentrations show a significant difference of the domain size, affecting the atomic structures of the active and inactive Si dopants.[4]

4.2 Experimental

Using the MOVPE method, κ-Ga_2O_3 epitaxial layers were grown on a c-plane sapphire substrate. A H_2-diluted mixture of 0.05% SiH_4 was employed as the Si dopant source. Using a SiH_4 flow of 5 and 15 sccm, the resulting Si concentration in the κ-Ga_2O_3 layers was 0.54 and 1.02 atom %, respectively.[4] The Si dopant concentration was measured by the atomic probe tomography method.[4] Before PES and PEH measurements, the substrates were cleaned by the RCA method so that the surface contamination was removed. Then the surface oxide layer and the particles were removed by concentrated hydrochloric acid for 1 minute, followed by washing with deionized water.

Hall effect measurements with the Van der Pauw method were performed to measure the carrier concentration. The carrier concentrations were estimated to be 3.5×10^{18} cm^{-3} (0.54%) and 2.6×10^{18} cm^{-3} (1.02%), respectively.[4] The electronic transport was dominated by a hopping mechanism.[4]

XPS and HAXPES measurements were performed using PHI Quantes (ULVAC-PHI). Monochromatic Al Kα (1486.6 eV) and Cr Kα (5414.9 eV) were used as incident x-ray sources for the XPS and HAXPES. The energy resolutions for the XPS and the HAXPES measurements were estimated to be 0.51 and 1.11 eV, respectively. The take-off angle (TOA) was 45° (the surface normal is 90°). Au film was used to estimate the Fermi level and perform the energy calibration.

PEH measurements were performed at BL25SU at SPring-8. The base pressure of the main chamber was 2.8×10^{-8} Pa. RFA was used for the PEH measurements. The RFA's energy resolution was approximately 0.5 eV.[22-24] The RFA's acceptance angle was approximately ±49°, and the angular resolution was 0.5°.[24]

PEH simulations were performed using 3D-AIR-IMAGE software (version 1.1.09).[25-28] For the simulations, an electron kinetic energy of 800 eV, a temperature of

300 K, and an inelastic mean free path of 10 Å were employed. Figure 4.1 shows the PEH schematic for Si-doped κ-Ga_2O_3.

EXAFS measurements were carried out at BL6N1 at Aichi SR. The base pressure of the main chamber was 3.1 × 10^{-7} Pa. For the EXAFS measurements, the total electron yield was employed. The spot size of the incident photon at the sample position was 2.0 mm × 1.0 mm (horizontal × vertical).[29] The energy range and the energy step for the EXAFS measurements was from 1800 to 2250 eV and 1.0 eV, respectively.

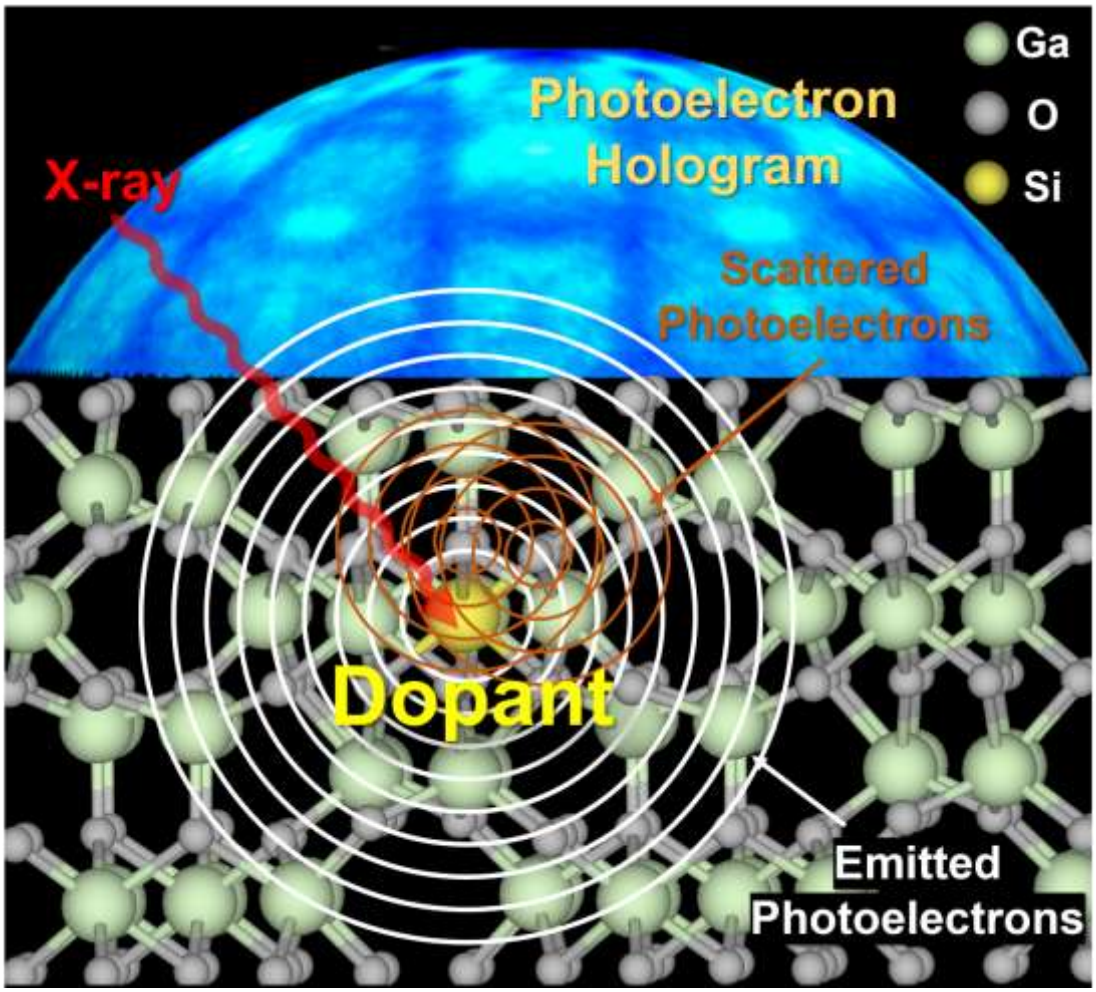

Figure 4.1. PEH schematic for Si-doped κ-Ga_2O_3. Yellow, green, and gray balls represent Si, Ga, and O atoms.[30]

4.3 Results

Figure 4.2 shows the XPS and HAXPES spectra for the Si-doped κ-Ga_2O_3(001). In the Ga 2*p* XPS spectrum for 0.54% Si-doped κ-Ga_2O_3(001) (Fig. 4.2(a)), one

symmetric peak is observed at 1118.9 eV. This peak is attributed to the Ga atom bonded to the O atoms.[31-33] In the Si 1*s* HAXPES spectrum for 0.54% Si-doped κ-Ga_2O_3(001) (Fig. 4.2(b)), a symmetric peak observed at 1842.8 eV is due to the Si bonded with four O atoms (Si^{4+}).[34,35] In the Ga 2*p* XPS spectrum for 1.02% Si-doped κ-Ga_2O_3(001) (Fig. 4.2(c)), a symmetric peak is observed at 1119.0 eV. This peak is attributed to the Ga atom bonded with O atoms.[31-33] In the Si 1*s* HAXPES spectrum for 1.02% Si-doped κ-Ga_2O_3(001) (Fig. 4.2(d)), one symmetric peak observed at 1842.8 eV is due to the Si bonded with four O atoms (Si^{4+}).[34,35]

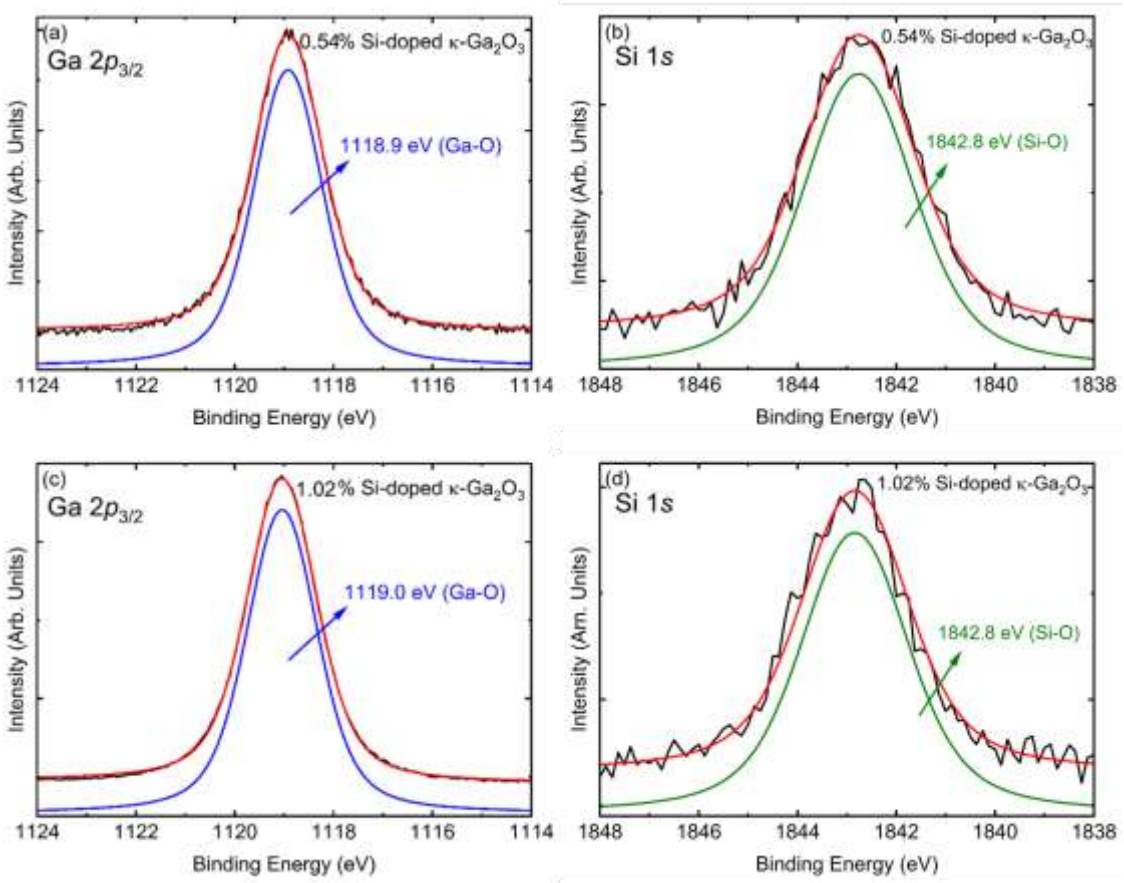

Figure 4.2. (a) Ga $2p_{3/2}$ XPS and (b) Si 1*s* HAXPES spectra for 0.54% Si-doped κ-Ga_2O_3(001). (c) Ga $2p_{3/2}$ XPS and (d) Si 1*s* HAXPES spectra for 1.02% Si-doped κ-Ga_2O_3(001). Photon energies were 1486.6 eV (XPS) and 5414.9 eV (HAXPES), respectively. Black solid line is the experimental spectrum. Red solid line is the fitting result. Blue and green solid lines represent the Ga 2*p* and Si 1*s* fitting results.

Figures 4.3 (a) shows the Ga 3*p* and Si 2*p* PES spectra for the 0.54% Si-doped κ-Ga_2O_3(001). For the peak fitting, spin-orbit splitting of 3.46 eV for Ga 3*p* and 0.60 eV

for Si 2*p* were employed.[36-39] For the areal intensity of the peak fitting, the areal intensity ratio of $p_{3/2}$ orbital to $p_{1/2}$ orbital was set to 2.0.[40] The corresponding PEHs for Ga 3*p* and Si 2*p* are shown in Figs. 4.3 (b) and (c). The PEH hologram of Si 2*p* (Fig. 4.3(c)) is similar to that of Ga 3*p* (Fig. 4.3(b)). For examples, the Si 2*p* PEH hologram has the strong photoelectron intensities indicated by the red ellipses. These strong intensities in the red ellipses are also observed at the Ga 3*p* PEH hologram, indicating that the atomic positions of the Si atoms and the Ga atoms is the same. Thus, the Si atom should be located at the Ga atomic position in the unit cell of κ-Ga_2O_3(001).

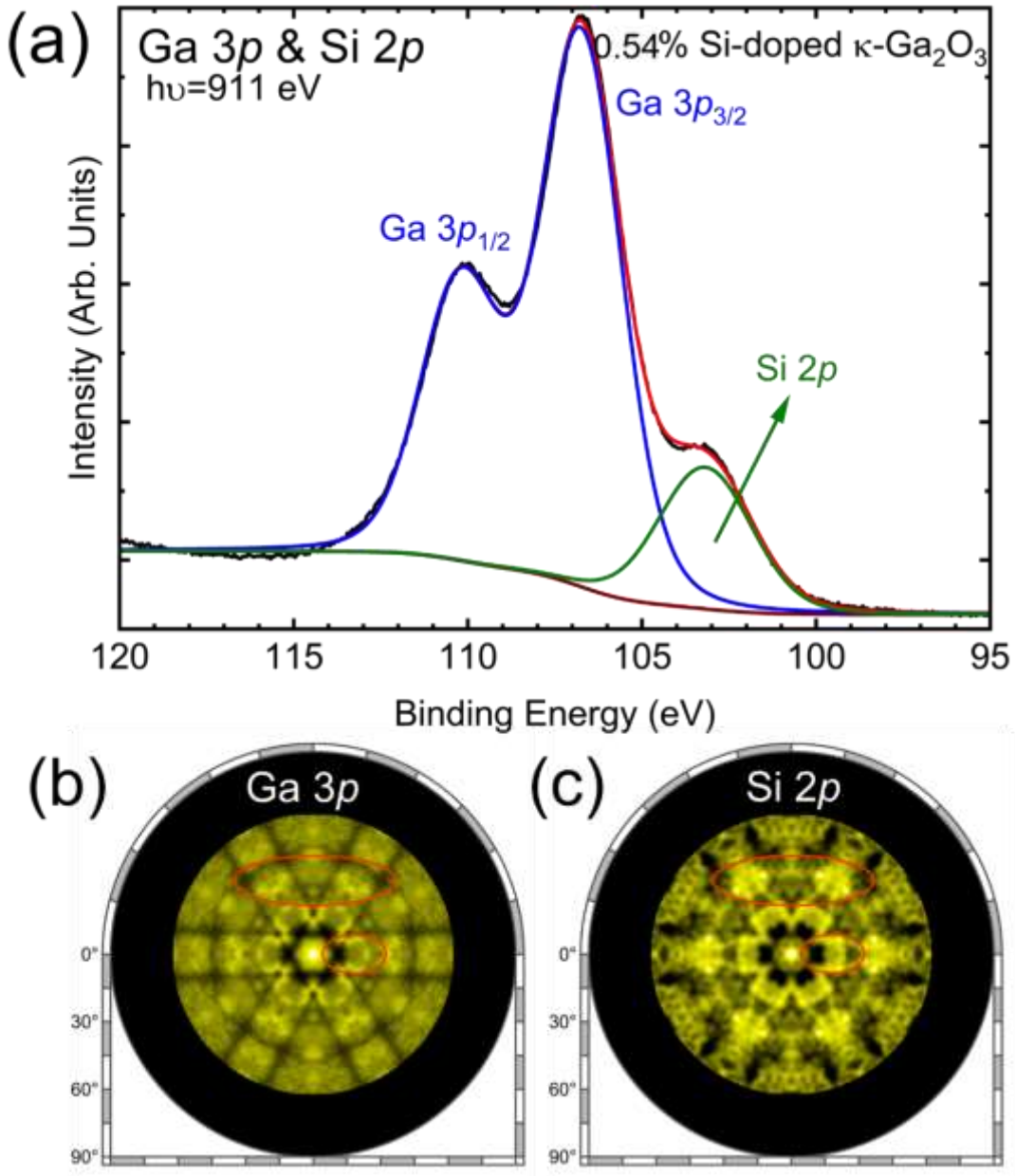

Figure 4.3. (a) Ga 3*p* and Si 2*p* PES spectra for 0.54% Si-doped κ-Ga_2O_3(001). Black solid line is the experimental spectrum. Red solid line represents the fitting result. Brown solid line is the Shirley background. Blue and green solid lines are the Ga 3*p* and Si 2*p* fitting results. PEHs of (b) Ga 3*p* and (c) Si 2*p* for 0.54% Si-doped κ-Ga_2O_3(001). The photon energy was 911.0 eV.

Figures 4.4 (a) shows the Ga 3*p* and Si 2*p* PES spectra for the 1.02% Si-doped κ-Ga_2O_3(001). For the peak fitting parameters, spin-orbit splitting was set to be 3.46 eV for Ga 3*p* and 0.60 eV for Si 2*p*.[36-39] For the areal intensity of the peak fitting, the value

of 2.0 was used for the areal intensity ratio of $p_{3/2}$ orbital to $p_{1/2}$ orbital.[40] Figures 4.4 (b) and (c) show the corresponding PEHs for Ga 3*p* and Si 2*p*. In Fig. 4.4(c), the PEH hologram of Si 2*p* is similar to that of Ga 3*p* (Fig. 4.4(b)). For instance, the Si 2*p* PEH hologram exhibits strong photoelectron intensities indicated by the red ellipses. These are also observed in the Ga 3*p* PEH hologram, suggesting that the atomic structures of Si and Ga atoms may be identical. Thus, the Si atom should be located at the Ga atomic position in the unit cell of κ-Ga_2O_3(001).

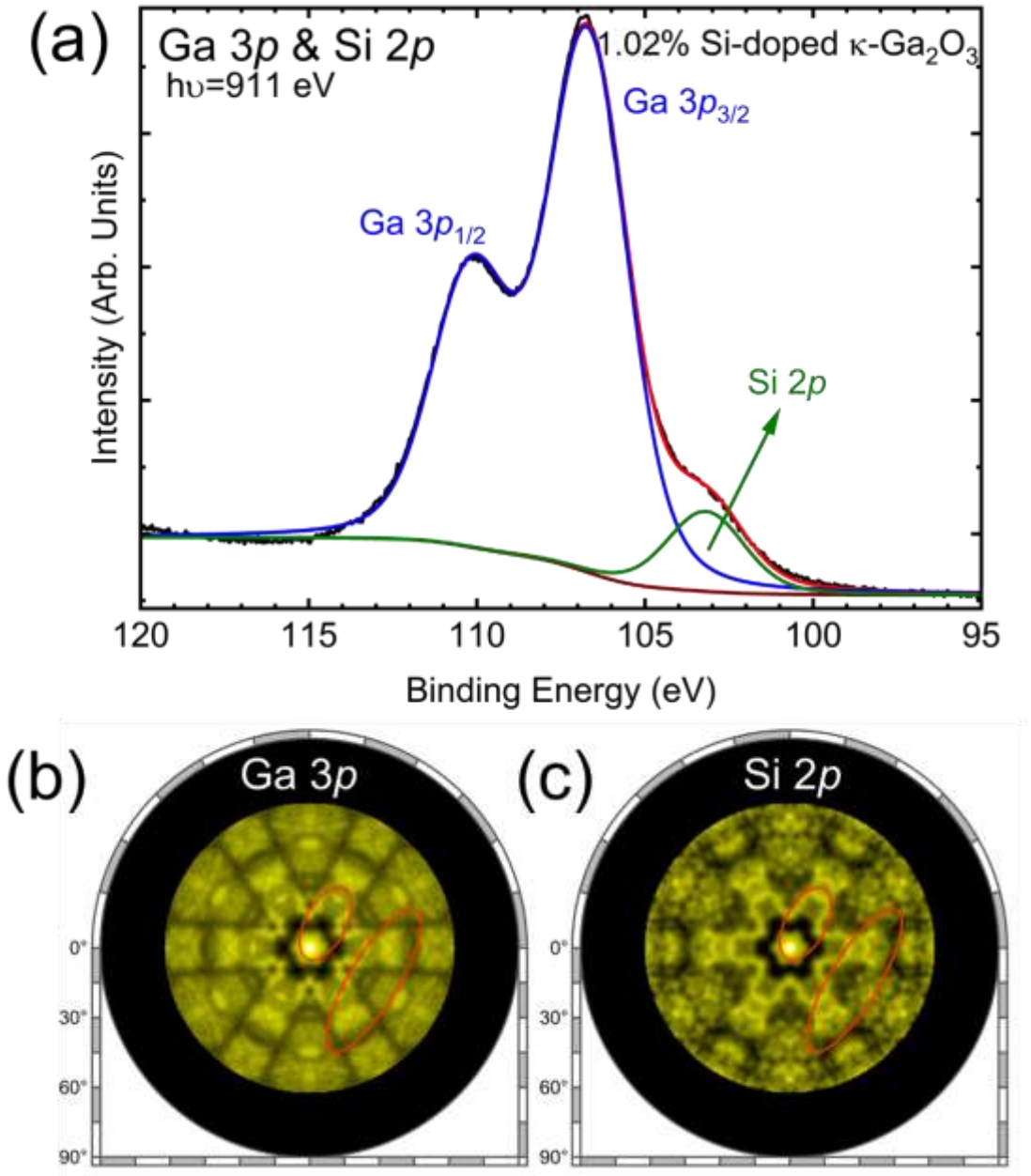

Figure 4.4. (a) Ga 3*p* and Si 2*p* PES spectra for 1.02% Si-doped κ-Ga_2O_3(001). Black solid line is the experimental spectrum. Red solid line is the fitting result. Brown solid line represents the Shirley background. Blue and green solid lines are the Ga 3*p* and Si 2*p* fitting results. PEHs of (b) Ga 3*p* and (c) Si 2*p* for 1.02% Si-doped κ-Ga_2O_3(001). The photon energy was 911.0 eV.

When the Si dopants are introduced into the κ-Ga_2O_3(001), the bond length around the Si dopant should be changed due to the relaxation effect of the atomic structure of the Si dopant. Thus, to obtain the accurate bond length of the Si dopant

structure after the dopant introduction, EXAFS measurements were performed.

Figures. 4.5 (a) and (b) show the Si K-edge EXAFS spectra before (Fig. 4.5(a)) and after (Fig. 4.5(b)) normalization for the 0.54% Si-doped κ-Ga_2O_3(001). The absorption peak at around 1850 eV is due to the Si 1*s*→ Si 3*p* transition in the Si K-edge EXAFS spectra.[41,42] Figures. 4.5(c) shows the Si K-edge EXAFS oscillation for the 0.54% Si-doped κ-Ga_2O_3(001). Figures 4.5(d) shows the radial distribution function of the k^2-weighted EXAFS without phase shift correction. Note that since the phase shift is occurred by the scattering between the photoelectron of the absorbing atom and the neighboring atoms,[43,44] shifting the amount of phase in the wave function. Thus, the peak position in Fig. 4.5(d) does not represent the real Si-O atom distance in 0.54% Si-doped κ-Ga_2O_3(001).

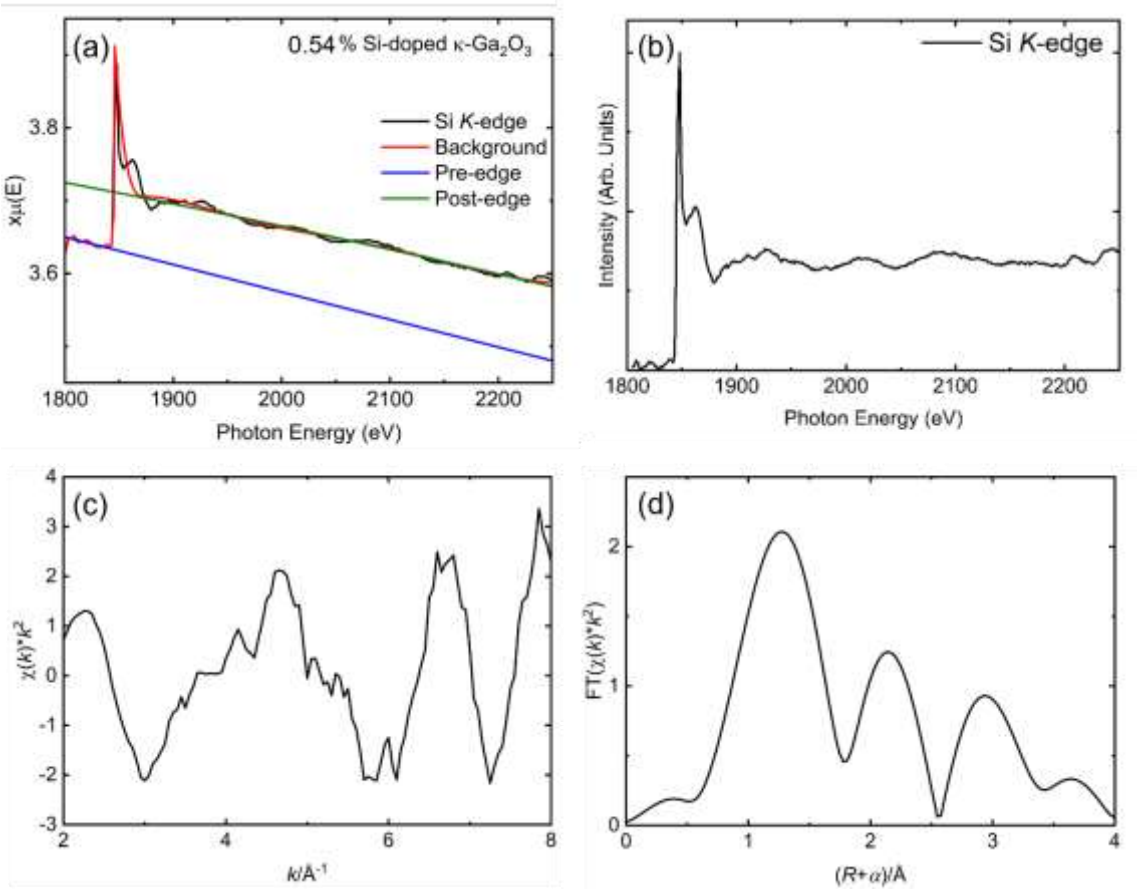

Figure 4.5. Si *K*-edge EXAFS spectrum (a) before and (b) after normalization for 0.54% Si-doped κ-Ga_2O_3(001). (c) k^2-weighted Si *K*-edge EXAFS for 0.54% Si-doped κ-Ga_2O_3(001). (d) The radial distribution function of the k^2-weighted EXAFS without phase shift correction.

Figures 4.6 (a)-(c) show k^2-weighted Si *K*-edge EXAFS and the fitting results of the Octa, Penta, and Tetra Si_{Ga} sites for 0.54% Si-doped κ-Ga_2O_3(001). The fitting range in the k-space was chosen at 2–7.0 $Å^{-1}$ because this range showed an adequate S/N ratio. Figures 4.6 (d)-(f) show the radial distribution function of the k^2-weighted EXAFS and the fitting results of the Octa, Penta, and Tetra Si_{Ga} sites. For the radial distribution function, the fitting range was 1–4 Å. The amplitude reduction factor was set to 1.[45] The fitting was performed using ARTEMIS software,[43,44] and the reliable factors (R-factors) for the Octa, Penta, and Tetra Si_{Ga} sites were set to 0.027, 0.012, and 0.006, respectively. The R-factor is due to the percentage of misfit. For an adequate fit, an R-factor is typically less than 0.03.[46] From the fitting results, the nearest Si-O distance was estimated to be 2.00 Å, 2.01 Å, and 1.83 Å for the Octa, Penta, and Tetra Si_{Ga} sites, respectively.

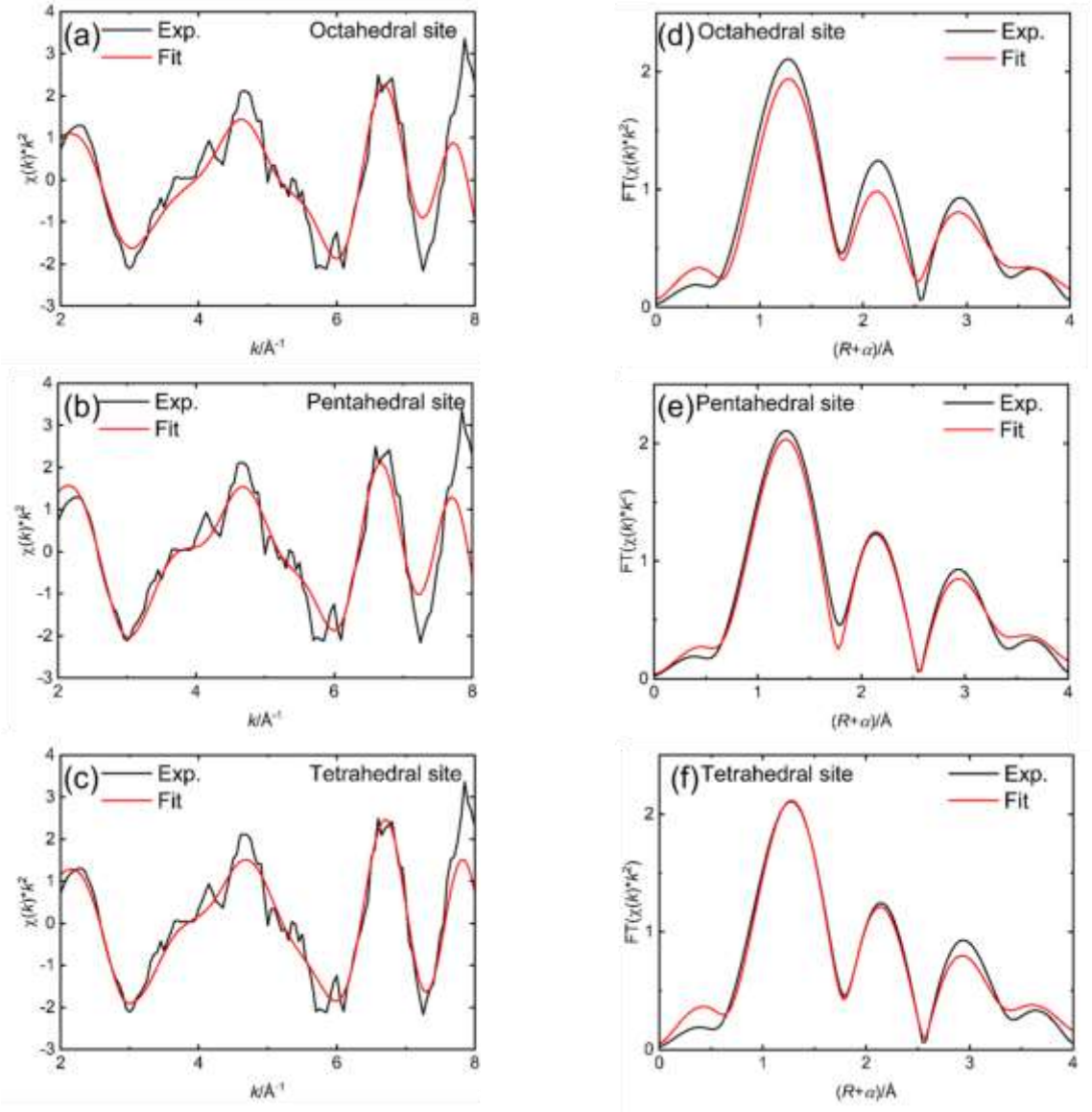

Figure 4.6. k^2-weighted Si *K*-edge EXAFS (black solid line) and the fitting results (red solid line) for (a) Octa Si_{Ga} site, (b) Penta Si_{Ga} site, and (c) Tetra Si_{Ga} site for the 0.54% Si-doped κ-Ga_2O_3(001). The radial distribution function of the k^2-weighted EXAFS (black solid line) and the fitting results (red solid line) for (d) Octa Si_{Ga} site, (e) Penta Si_{Ga} site, and (f) Tetra Si_{Ga} site.

Figures. 4.7 (a) and (b) show the Si K-edge EXAFS spectra for the 1.02% Si-doped κ-Ga_2O_3(001) before (Fig.4.7(a)) and after (Fig.4.7(b)) normalization. In the Si K-edge EXAFS spectra, the absorption peak at about 1850 eV is due to the Si 1*s*→ Si 3*p* transition.[41,42] Figures. 4.7(c) shows the Si K-edge EXAFS oscillation for the 1.02% Si-doped κ-Ga_2O_3(001). Figures 4.7(d) shows the radial distribution function of the k^2-

weighted EXAFS without phase shift correction. The peak position in Fig. 4.7(d) does not represent the real Si-O atomic distance in 1.02% Si-doped κ-Ga_2O_3(001), as described above yet.

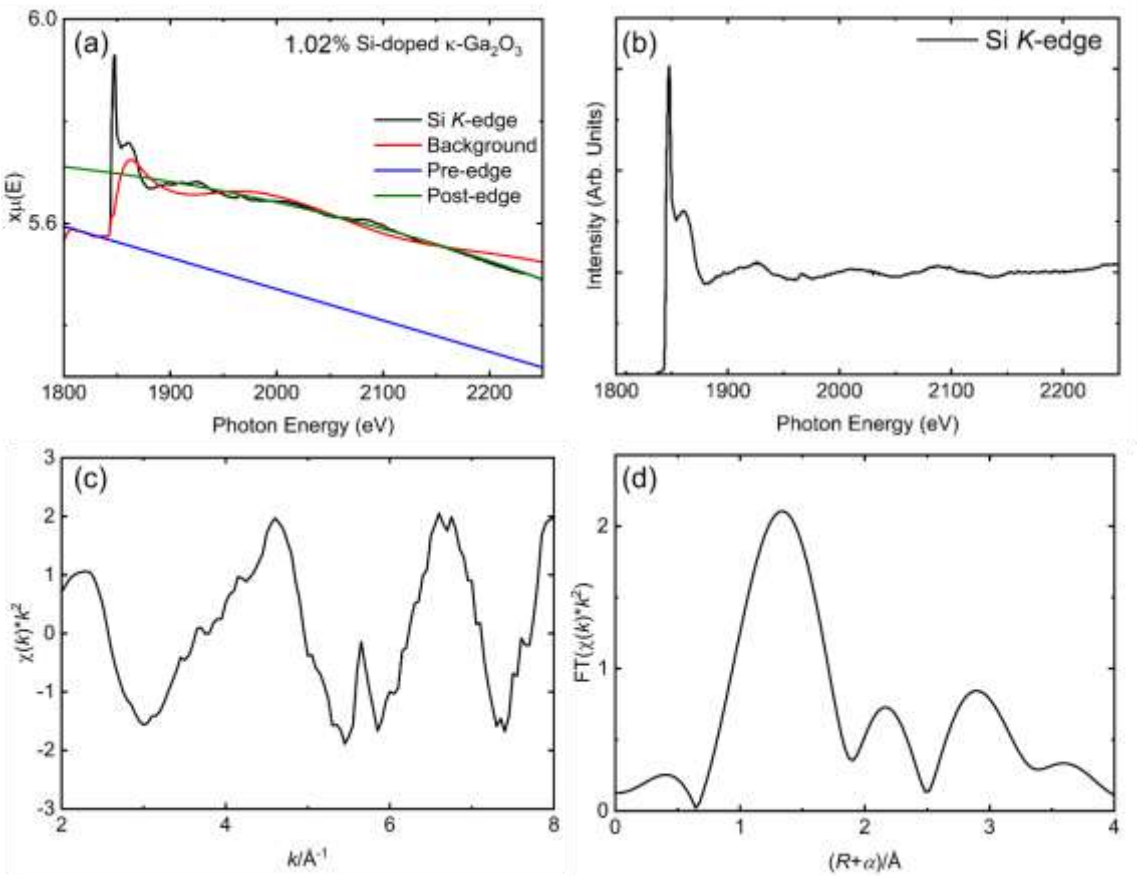

Figure 4.7. Si *K*-edge EXAFS spectrum (a) before and (b) after normalization for 1.02% Si-doped κ-Ga_2O_3(001). (c) k^2-weighted Si *K*-edge EXAFS for 1.02% Si-doped κ-Ga_2O_3(001). (d) The radial distribution function of the k^2-weighted EXAFS without phase shift correction.

Figures 4.8 (a)-(c) show k^2-weighted Si *K*-edge EXAFS and the fitting results of the Octa, Penta, and Tetra Si_{Ga} sites for 1.02% Si-doped κ-Ga_2O_3(001). The fitting range in the k-space was chosen at 2–7.2 $Å^{-1}$ because this range showed an adequate S/N ratio. Figures 4.8 (d)-(f) show the radial distribution function of the k^2-weighted EXAFS and the fitting results of the Octa, Penta, and Tetra Si_{Ga} sites. For the radial distribution function, the fitting range was 1–4 Å. The amplitude reduction factor was set to 1.[45] The fitting was performed using ARTEMIS software, and the R-factors for the Octa, Penta, and Tetra Si_{Ga} sites were set to 0.015, 0.005, and 0.005, respectively.[46]

From the fitting results, the nearest Si-O distance was estimated to be 2.01 Å, 2.02 Å, and 1.83 Å for the Octa, Penta, and Tetra Si_{Ga} sites, respectively.

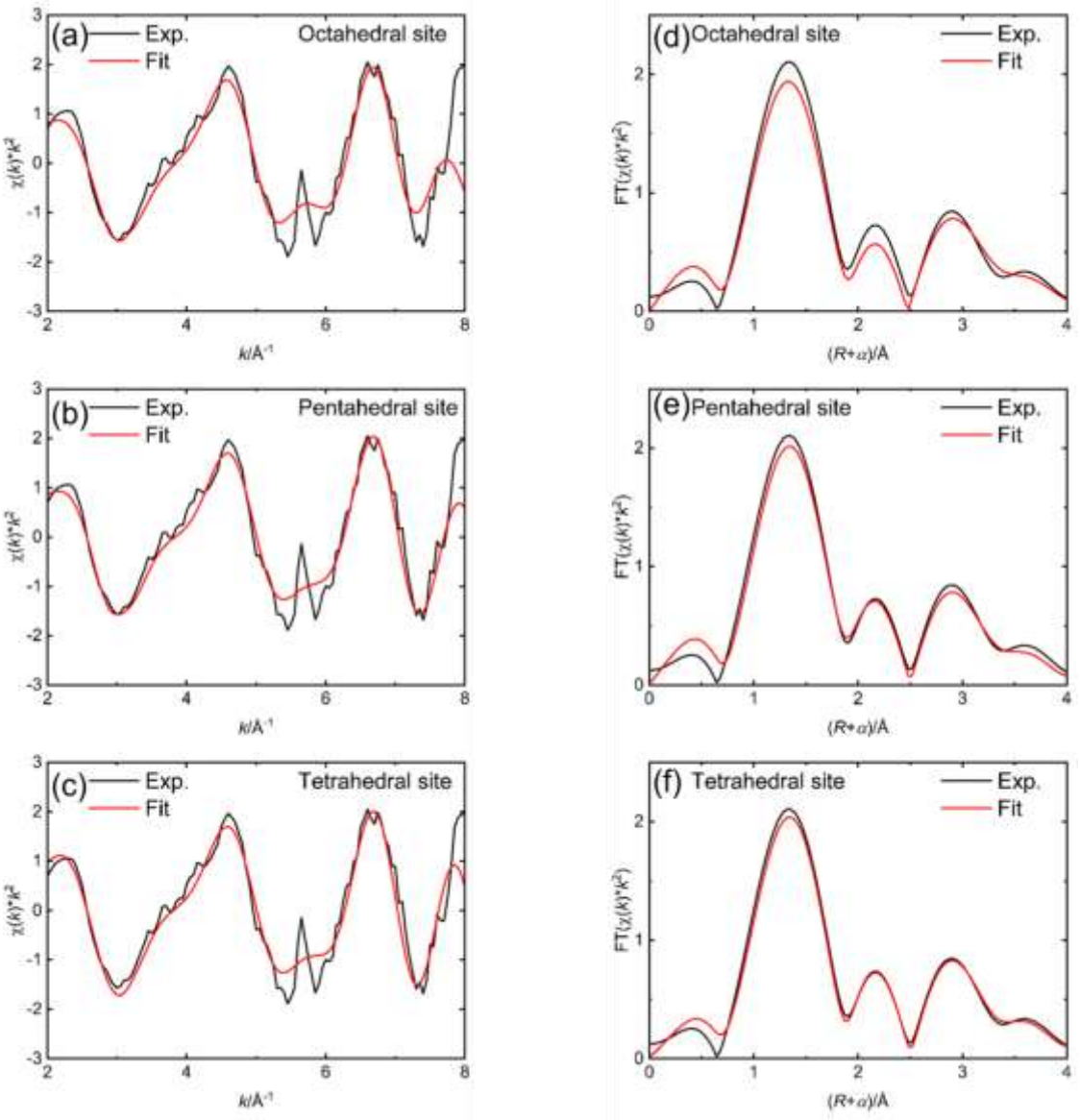

Figure 4.8. k^2-weighted Si *K*-edge EXAFS (black solid line) and the fitting results (red solid line) for (a) Octa Si_{Ga} site, (b) Penta Si_{Ga} site, and (c) Tetra Si_{Ga} site for the 1.02% Si-doped κ-Ga_2O_3(001). The radial distribution function of the k^2-weighted EXAFS (black solid line) and the fitting results (red solid line) for (d) Octa Si_{Ga} site, (e) Penta Si_{Ga} site, and (f) Tetra Si_{Ga} site.

Figures 4.9 shows the simulated Si 2*p* PEHs for the Octa (Fig. 4.9(a)), Penta (Fig. 4.9(b)), and Tetra (Fig. 4.9(c)) Si_{Ga} sites for the 0.54% Si-doped κ-Ga_2O_3(001).

The simulated PEHs were performed using the bond length obtained from EXAFS.

Figures 4.10 shows the experimental (left) and the simulated (right) Si 2*p* PEHs for the Octa, Penta, and Tetra Si_{Ga} sites for the 0.54% Si-doped κ-Ga_2O_3(001).

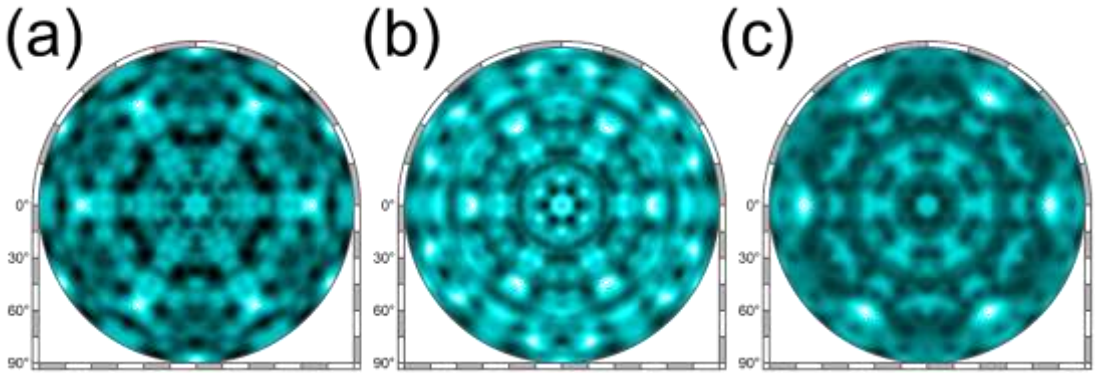

Figure 4.9. The simulated PEHs of (a) Octa Si_{Ga} site (b) Penta Si_{Ga} site (c) Tetra Si_{Ga} site for the 0.54% Si-doped κ-Ga_2O_3(001).

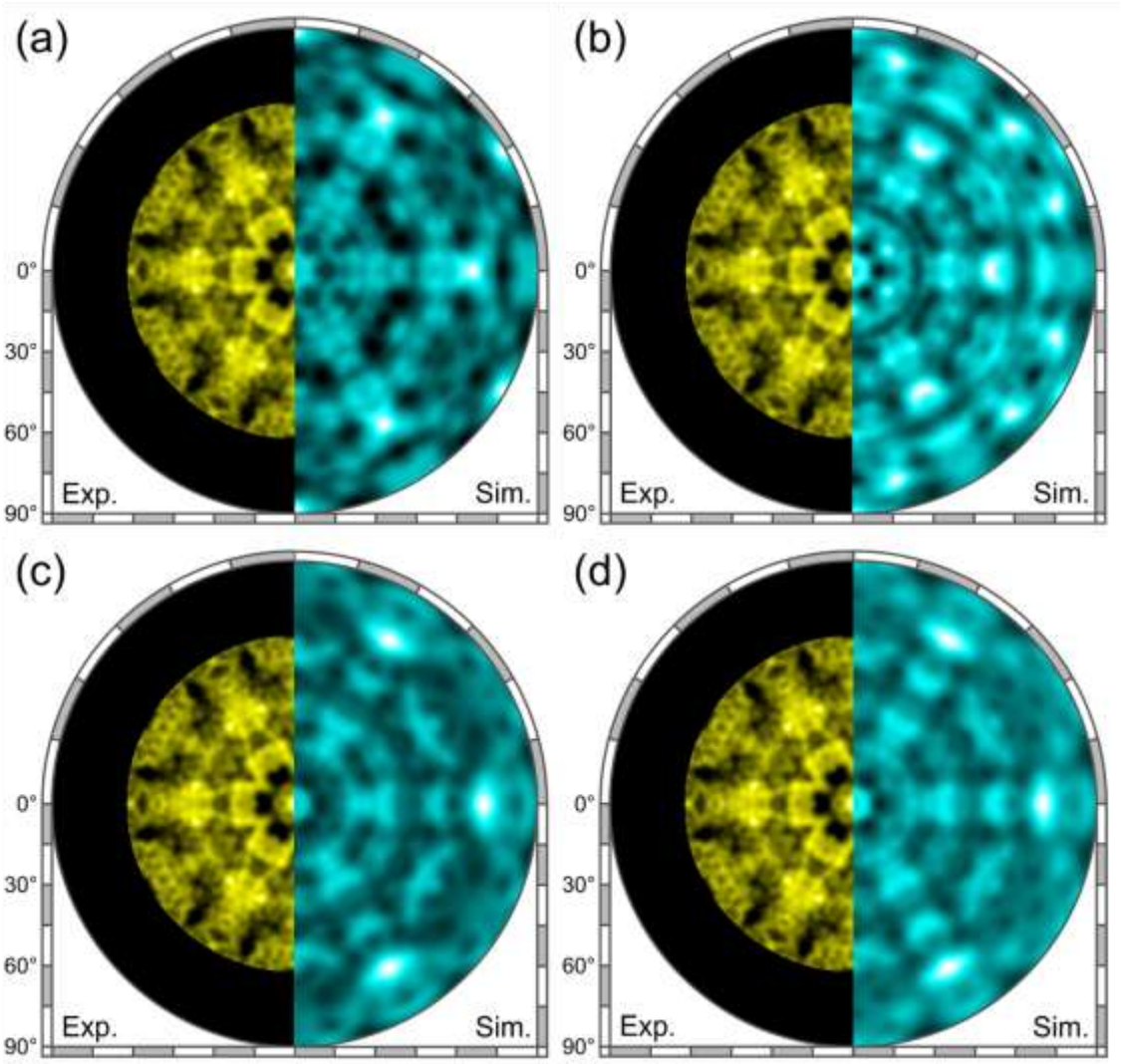

Figure 4.10. Experimental (yellow) Si 2*p* and the simulated (blue) PEHs for the 0.54% Si-doped κ-Ga_2O_3(001). The simulated PEHs of (a) Octa Si_{Ga} site (b) Penta Si_{Ga} site (c) Tetra Si_{Ga} site, and (d) their sum are 13.8% (Octa Si_{Ga} site), 35.2% (Penta Si_{Ga} site), and 51.0% (Tetra Si_{Ga} site).

Figures 4.11 shows the simulated Si 2*p* PEHs for the Octa (Fig. 4.11(a)), Penta (Fig. 4.11(b)), and Tetra (Fig. 4.11(c)) Si_{Ga} sites for the 1.02% Si-doped κ-Ga_2O_3(001). The simulated PEHs were performed using the bond length of Si-O obtained from EXAFS.

Figures 4.12 shows the experimental (left) and the simulated (right) Si 2*p* PEHs for the Octa, Penta, and Tetra Si_{Ga} sites for the 1.02% Si-doped κ-Ga_2O_3(001).

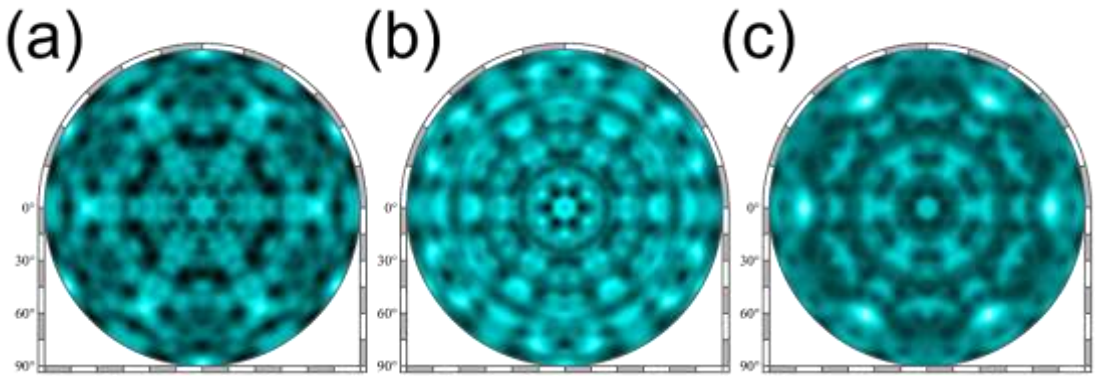

Figure 4.11. Simulated PEHs for the 1.02% Si-doped κ-Ga_2O_3(001). The simulated PEHs of (a) Octa Si_{Ga} site (b) Penta Si_{Ga} site (c) Tetra Si_{Ga} site.

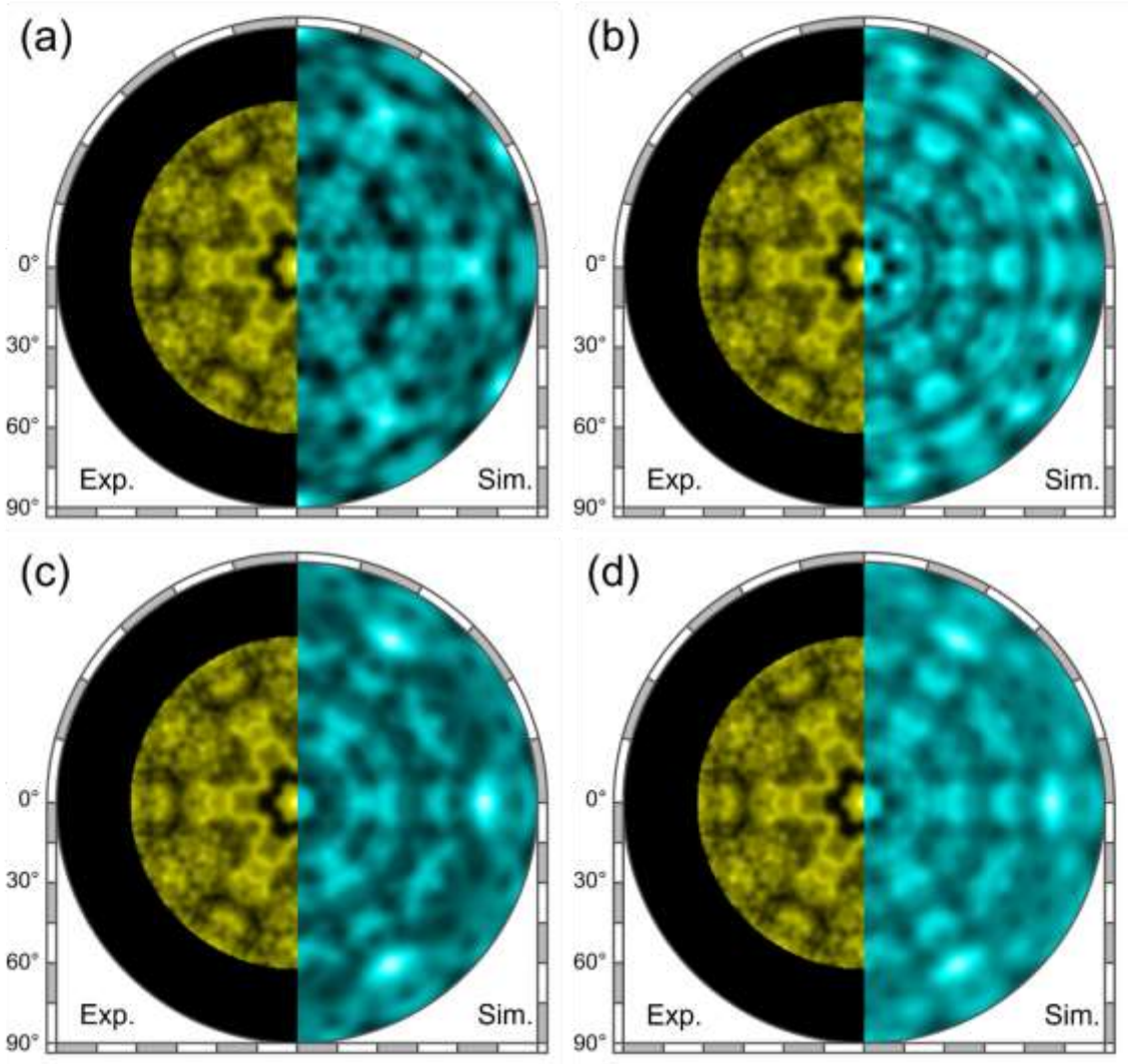

Figure 4.12. Experimental (yellow) Si 2*p* and the simulated (blue) PEHs for the 1.02% Si-doped κ-Ga_2O_3(001). The simulated PEHs of (a) Octa Si_{Ga} site (b) Penta Si_{Ga} site (c) Tetra Si_{Ga} site, and (d) their sum are 16.9% (Octa Si_{Ga} site), 28.1% (Penta Si_{Ga} site), and 55.0% (Tetra Si_{Ga} site).

4.4 Discussion

First of all, it is discussed the possibility of the presence of different oxidation states. When the different Si oxidation states (from 1^+ to 4^+) exist, the corresponding peaks in the Si 1*s* core level spectrum should be observed at lower binding energy positions from 1 to 3 eV (depending on the oxidation states),[47,48] forming an asymmetric peak structure. However, the Si 1*s* HAXPES spectra show one symmetric peak structure (Figs. 4.2(b) and 4.2(d)). Therefore, the possibility of the presence of the different Si oxidation states can be excluded. Thus, the chemical state of the Si dopant shows one

chemical state, that is, the Si atom bonded with four O atoms. This result also indicates that the atomic structure of the dopant is not due to the interstitial site because the interstitial site shows the lower oxidation state of the Si atom; Si atom bonded with two O atoms.

Next, it is discussed why the 0.54% Si-doped κ-Ga_2O_3(001) shows a higher peak intensity of Si 2*p* than the 1.02% Si-doped κ-Ga_2O_3(001). The information depth of the PEH measured by the photon energy of 911 eV is estimated to be 4.53 nm using the TPP-2M formula.[49] In this depth, the 0.54 and 1.02 % Si-doped κ-Ga_2O_3(001) show 1.55 and 1.03 % Si concentrations, respectively, by considering the areal intensity ratio of the Si 2*p* and Ga 3*p* PES spectra, and the Si 2*p* and Ga 3*p* ionazation cross section of the photon energy of 911.0 eV. The information depth for the HAXPES (the photon energy of 5414.9 eV), on the other hand, is estimated to be 14.61 nm using the TPP-2M formula.[49] In this depth, the 0.54 and 1.02 % Si-doped κ-Ga_2O_3(001) show nearly equal Si concentrations; the Si concentrations were estimated to be 1.01% and 0.96% for the 0.54 and 1.02 % Si-doped κ-Ga_2O_3(001). For the atomic probe tomography used for the Si concentration measurements in the present study, on the other hand, the Si concentration was estimated from 0.0 to 110 nm depth, and the Si concentrations were estimated to be 0.54 and 1.02 %.[4] Thus, it is found that as the depth is closer to the surface, the 0.54% Si-doped κ-Ga_2O_3(001) shows a higher Si concentration than the 1.02% Si-doped κ-Ga_2O_3(001).

According to the previous study used by transmission electron microscope (TEM), the domains are predominantly formed near the surface.[4] For the domain size, 0.54% Si-doped κ-Ga_2O_3(001) shows much smaller domain sizes than 1.02% Si-doped κ-Ga_2O_3(001); 0.54% Si-doped κ-Ga_2O_3(001) shows a domain radial size of ~50 nm, whereas the domain radial size is ~300 nm in the case of 1.02% Si-doped κ-Ga_2O_3(001).[4] A small domain size increases the number of domain boundaries.[4] According to the previous research, domain boundaries show the trap sites of dopants, indicating that 0.54% Si-doped κ-Ga_2O_3(001) shows a higher concentration of the trap sites of Si dopants than 1.02% Si-doped κ-Ga_2O_3(001) near the surface.[50] Thus, near the surface, 0.54% Si-doped κ-Ga_2O_3(001) shows a higher Si concentration than 1.02% Si-doped κ-Ga_2O_3(001) because 0.54% Si-doped κ-Ga_2O_3(001) has significant small domains that trap the Si dopants.

Next, the occupation sites of Si dopants are discussed. For the PEHs, the simulated PEHs for the Octa, Penta, and Tetra Si_{Ga} sites cannot explain the experimental Si 2*p* PEH shown in Figs. 4.10 and 4.12, indicating that the Si dopant sites may be attributed to the mixture of the Octa, Penta, and Tetra Si_{Ga} sites. To determine the ratio

of these sites, the simulated Si 2p PEHs of the Tetra, Penta, and Octa Si_{Ga} sites were mixed. An error function was used to determine the accurate occupation ratios of the Tetra, Penta, and Octa Si_{Ga} sites.[28]

The following equation was used to estimate the ratios of each hologram. Define the following error function,

$$E = \sum_s \sum_i |\chi_e(\boldsymbol{k}_i) - a_s \ \chi_s(\boldsymbol{k}_i) - b|^2 \tag{4.1}$$

Here, $\chi_e(\boldsymbol{k}_i)$ represents the measured hologram, $\boldsymbol{k}_i$ is the wave vector of the photoelectrons, and i is the index for pixel of holograms. $\chi_s(\boldsymbol{k}_i)$ represents the hologram obtained through the simulations, where s =Octa, Penta, Tetra Si_{Ga} sites. b is a constant, and a_s is the coefficient for the hologram in the simulation. The coefficient a_s is determined by minimizing this error function.

$$\frac{\partial E}{\partial a_s} = 0 \, , \frac{\partial E}{\partial b} = 0 \tag{4.2}$$

The ratio for each site is obtained from the following formula,

$$R_s = \frac{a_s}{\sum_s a_s} \tag{4.3}$$

Thus, the ratio of Octa, Penta, and Tetra Si_{Ga} sites can be estimated.

Figures 4.13 (0.54% Si-doped κ-Ga_2O_3(001)) and 4.14 (1.02% Si-doped κ-Ga_2O_3(001)) show the differential images between the experimental and the simulated Si 2p PEHs for Octa, Penta, and Tetra Si_{Ga} sites and the mixture of the Octa, Penta, and Tetra Si_{Ga} sites. The differential images were calculated using ImageJ software.[51] The intensity of the experimental and simulated Si 2p PEHs was normalized by the highest intensity in the image. In Figs. 4.13 and 4.14, the highest and the lowest thresholds in the pixels of the image were used to adjust the image contrast.

The white area in the images means differences between the experimental and the simulated Si 2p PEHs, whereas the black area indicates good agreement between the experimental and the simulated ones. As can be seen, Figures 4.13(a) and 4.14(a) exhibit the least white area among the images shown in Figs. 4.13 and 4.14, respectively.

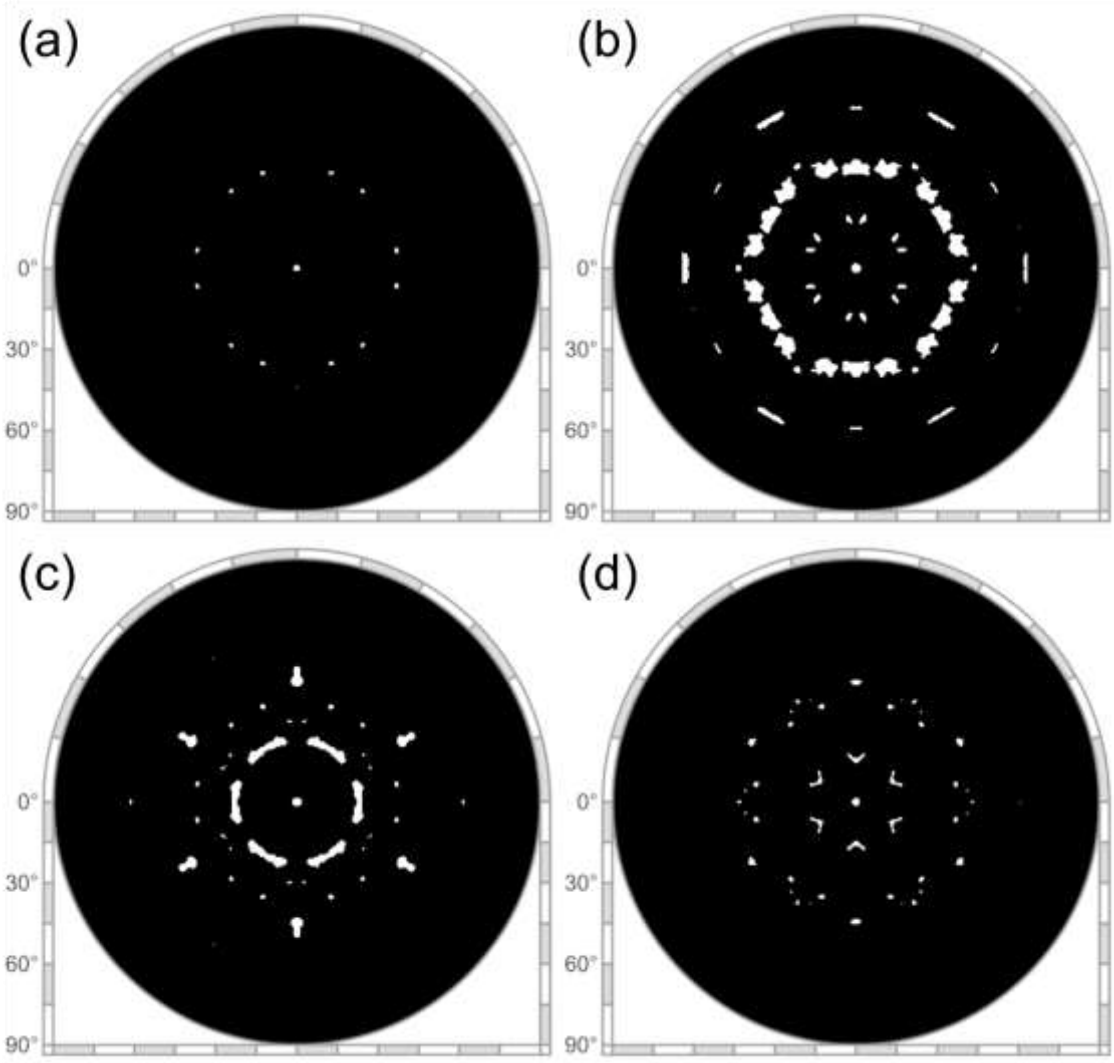

Figure 4.13. Differential images between the experimental and the simulated Si 2*p* PEHs for (a) the sum of Octa, Penta, and Tetra Si_{Ga} sites where the respective ratio of 13.8%, 35.2%, and 51.0%, (b) Octa Si_{Ga} site, (c) Penta Si_{Ga} site, (d) Tetra Si_{Ga} site for the 0.54% Si-doped κ-Ga_2O_3(001).

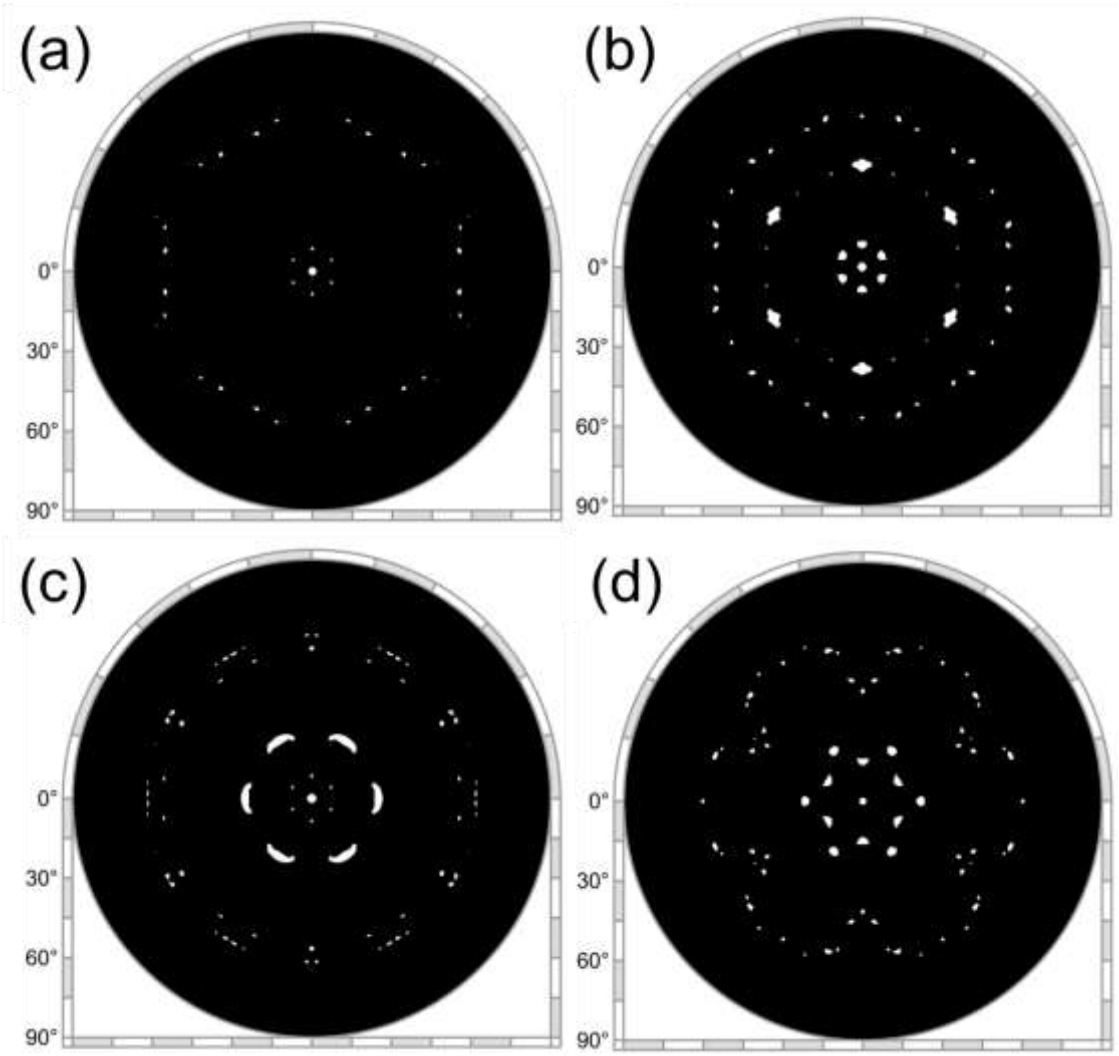

Figure 4.14. Differential images between the experimental and the simulated Si 2*p* PEHs for (a) the sum of Octa, Penta, and Tetra Si_{Ga} sites where the respective ratio of 16.9%, 28.1%, and 55.0%, (b) Octa Si_{Ga} site, (c) Penta Si_{Ga} site, (d) Tetra Si_{Ga} site for the 1.02% Si-doped κ-Ga_2O_3(001).

For the experimental PEHs, the ratios for the Tetra, Penta, and Octa Si_{Ga} sites are estimated to be 51.0%, 35.2%, and 13.8% (0.54% Si dopant) and 55.0%, 28.1%, and 16.9% (1.02% Si dopant), respectively. The 0.54% and 1.02% Si-doped κ-Ga_2O_3 show similar occupation ratios of Si_{Ga} sites. The mixture images of the PEHs are shown in Figs. 4.10(d) and 4.12(d) for the 0.54% and 1.02% Si-doped κ-Ga_2O, respectively.

For the undoped κ-Ga_2O_3, the ratios for the Tetra, Penta, and Octa sites in the unit cell are 25%, 25%, and 50%, respectively.[8,16] Therefore, based on the present results, Tetra Si_{Ga} site may be strongly favored with respect to the Penta and Octa Si_{Ga}

sites. The difference in these Si_{Ga} ratios might be due to the formation energy of three Si_{Ga} sites. In this framework, the Tetra site of the Si_{Ga} defect shows the lowest formation energy with respect to the Octa and Penta coordinations. This result is supported by the density functional theory, where the Tetra Si_{Ga} exhibits the lowest formation energy than the Octa and Penta Si_{Ga}.[52] Hence, the Tetra Si_{Ga} is the most stable site than the Octa and Penta Si_{Ga} in Si-doped κ-Ga_2O_3(001).

Von Bardeleben et al. investigated the electrically active dopant sites in Si-doped κ-Ga_2O_3 using EPR. They concluded that the electrically active and the signal-responsible dopant site was due to the Tetra Si_{Ga} site among the dopant sites.[13] Thus, it is concluded that the Tetra Si_{Ga} site is the active dopant site for the Si-doped κ-Ga_2O_3 in the present study. On the other hand, the other dopant sites, that is, the Octa and the Penta Si_{Ga} sites, are not the signal-responsible sites for the EPR measurements, indicating that they are electrically inactive dopant sites. Thus, it is concluded that the Penta and the Octa Si_{Ga} sites are due to the inactive dopants for the Si-doped κ-Ga_2O_3. Figure 4.15 shows the atomic structures for the Octa, Penta, and Tetra Si_{Ga} sites in κ-Ga_2O_3.

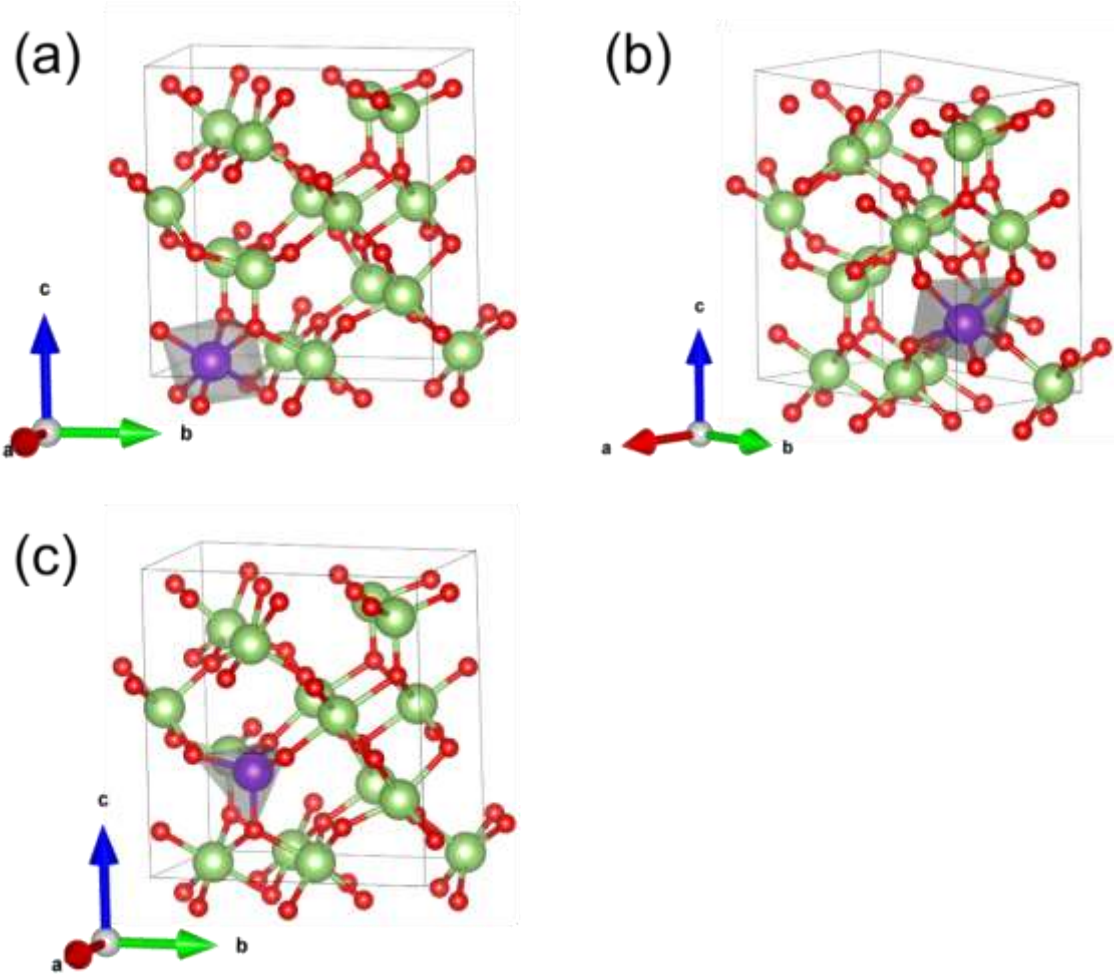

Figure 4.15. Atomic structures for (a) Octa, (b) Penta, and (c) Tetra Si_{Ga} site in κ-Ga_2O_3. Light green, purple, and red balls indicate Ga, Si and O atoms, respectively.

Finally, the relationship between the Si dopant concentration and the corresponding carrier concentrations is discussed. The Hall effect measurements showed the carrier concentrations of 3.5 and 2.6 × 10^{18} cm^{-3} for 0.54% and 1.02% Si-doped κ-Ga_2O_3 samples, indicating that 0.54% Si-doped κ-Ga_2O_3 shows higher carrier concentration in the present study. Considering that both 0.54% and 1.02% Si-doped κ-Ga_2O_3 show similar occupation ratios of Si_{Ga} sites and 0.54% Si-doped κ-Ga_2O_3 exhibits half of the dopant concentration of 1.02% Si-doped κ-Ga_2O_3, it is expected that 0.54% Si-doped κ-Ga_2O_3 should show half of the carrier concentration of 1.02% Si-doped κ-Ga_2O_3. However, 1.02% Si-doped κ-Ga_2O_3 exhibits a lower carrier concentration than 0.54% Si-doped κ-Ga_2O_3, as described above. This discrepancy may be explained as follows. In the Si-doped κ-Ga_2O_3, it is reported that disordered plane defects are formed, and they increase the density with increasing domain size.[4] In the

present study, the domain sizes for 0.54% and 1.02% Si-doped κ-Ga_2O_3 are ~50 and ~300 nm, respectively.[4] Thus, 1.02% Si-doped κ-Ga_2O_3 exhibits a larger domain size, increasing the disordered plane defect density. The disordered plane defects could be electrically charged and trap the carriers.[20,21] Therefore, some carriers may be trapped by these plane defects, decreasing the carrier concentration. As a result, 1.02% Si-doped κ-Ga_2O_3 exhibits a lower carrier concentration than 0.54% Si-doped κ-Ga_2O_3.

4.5 Conclusion

PES, PEH, and EXAFS were employed to clarify the chemical states and the atomic positions of the Si dopants for Si-doped κ-Ga_2O_3(001). From XPS and HAXPES, the Si dopant showed one chemical state, and the state was attributed to the Si bonded with two oxygen atoms. Since the experimental Si 2*p* PEH showed clear hologram patterns for the Si dopant, the Si dopant should be located at the cationic positions of κ-Ga_2O_3(001). The simulated PEHs were performed to clarify the precise occupation sites of the Si dopants in the orthorhombic lattice. It was found that the simulated PEH of each inequivalent Si_{Ga} site (i.e., Tetra, Penta, and Octa) could not explain the experimental Si 2*p* PEH. Thus, the Si dopant was found to occupy all the inequivalent Si_{Ga} sites. From the fitting results of PEHs, the ratios of the Tetra, Penta, and Octa Si_{Ga} sites were estimated to be 51.0% (55.0%), 35.2% (28.1%), and 13.8% (16.9%) for the 0.54% (1.02%) Si-doped κ-Ga_2O_3(001), respectively. It is concluded that the active dopant site in Si-doped κ-Ga_2O_3 is the Tetra Si_{Ga} site, whereas the Penta and Octa Si_{Ga} sites are due to the inactive dopant sites.

References

1. K. Kaneko, K. Uno, R. Jinno, and S. Fujita, *Journal of Applied Physics* **131**, 090902 (2022).
2. Y. Wang, J. Su, Z. Lin, J. Zhang, J. Chang, and Y. Hao, *Journal of Materials Chemistry C* **10**, 13395 (2022).
3. N.S. Jamwal and A. Kiani, *Nanomaterials* **12**, 2061 (2022).
4. P. Mazzolini, Z. Fogarassy, A. Parisini, F. Mezzadri, D. Diercks, M. Bosi, L. Seravalli, A. Sacchi, G. Spaggiari, D. Bersani, O. Bierwagen, B.M. Janzen, M.N. Marggraf, M.R. Wagner, I. Cora, B. Pécz, A. Tahraoui, A. Bosio, C. Borelli, S. Leone, and R. Fornari, *Advanced Functional Materials* **33**, 2207821 (2022).
5. H.H. Tippins, *Physical Review* **140**, A316 (1965).
6. S. Mu and C.G. Van de Walle, *Physical Review Materials* **6**, 104601 (2022).
7. F. Mezzadri, G. Calestani, F. Boschi, D. Delmonte, M. Bosi, and R. Fornari, *Inorganic Chemistry* **55**, 12079 (2016).
8. H.Y. Kang, Y. Choi, K. Pyeon, T.H. Lee, and R.B. Chung, *Journal of Materials Science* **57**, 19882 (2022).
9. S.B. Cho and R. Mishra, *Applied Physics Letters* **112**, 162101 (2018).
10. P. Ranga, S.B. Cho, R. Mishra, and S. Krishnamoorthy, *Applied Physics Express* **13**, 061009 (2020).
11. M. Bosi, P. Mazzolini, L. Seravalli, and R. Fornari, *Journal of Materials Chemistry C* **8**, 10975 (2020).
12. B.M. Janzen, P. Mazzolini, R. Gillen, V.F. Peltason, L.P. Grote, J. Maultzsch, R. Fornari, O. Bierwagen, and M.R. Wagner, *Journal of Materials Chemistry C* **9**, 14175 (2021).
13. H.J. Bardeleben, J.L. Cantin, A. Parisini, A. Bosio, and R. Fornari, *Physical Review Materials* **3**, 084601 (2019).
14. M. Girolami, M. Bosi, V. Serpente, M. Mastellone, L. Seravalli, S. Pettinato, S. Salvatori, D.M. Trucchi, and R. Fornari, *Journal of Materials Chemistry C* **11**, 3759 (2023).
15. A. Ardenghi, O. Bierwagen, J. Lähnemann, J. Kler, A. Falkenstein, M. Martin, and P. Mazzolini, arXiv:2311.13318v1 [physics.app-ph]
16. S. Seacat, J.L. Lyons, and H. Peelaers, *Applied Physics Letters* **119**, 042104 (2021).
17. A. Parisini, A. Bosio, V. Montedoro, A. Gorreri, A. Lamperti, M. Bosi, G. Garulli, S. Vantaggio, and R. Fornari, *APL Materials* **7**, 031114 (2019).
18. A. Polyakov, I. Lee, V. Nikolaev, A. Pechnikov, A. Miakonkikh, M. Scheglov, E. Yakimov, A. Chikiryaka, A. Vasilev, A. Kochkova, I. Shchemerov, A. Chernykh, and S. Pearton, *Advanced Materials Interfaces*, 2300394 (2023).

19. I. Cora, F. Mezzadri, F. Boschi, M. Bosi, M. Čaplovičová, G. Calestani, I. Dódony, B. Pécz, and R. Fornari, *CrystEngComm* **19**, 1509 (2017).
20. O.F. Vyvenko, S.V. Shapenkov, E.V. Ubyivovk, A.S. Bondarenko, A.I. Pechnikov, V.I. Nikolaev, and S.I. Stepanov, *Materialia* **32**, 101942 (2023).
21. A. Fiedler, R. Schewski, M. Baldini, Z. Galazka, G. Wagner, M. Albrecht, and K. Irmscher, *Journal of Applied Physics* **122**, 165701 (2017).
22. T. Muro, T. Ohkochi, Y. Kato, Y. Izumi, S. Fukami, H. Fujiwara, and T. Matsushita, *Review of Scientific Instruments* **88**, 123106 (2017).
23. T. Muro, T. Matsushita, K. Sawamura, and J. Mizuno, *Journal of Synchrotron Radiation* **28**, 1669 (2021).
24. T. Matsushita, Y. Hashimoto, H. Tomita, Z. Sun, S. Kawamura, M.N. Fujii, and J. Mizuno, *e-Journal of Surface Science and Nanotechnology* **21**, 183 (2023).
25. T. Matsushita, F. Matsui, H. Daimon, and K. Hayashi, *Journal of Electron Spectroscopy and Related Phenomena* **178–179**, 195 (2010).
26. T. Matsushita, *Physica Status Solidi (b)* **255**, 1800091 (2018).
27. Y. Li, Z. Sun, N. Kataoka, T. Setoguchi, Y. Hashimoto, S. Takeuchi, S. Koga, S. Demura, K. Noguchi, H. Sakata, Y. Mizuguchi, T. Matsushita, T. Wakita, Y. Muraoka, and T. Yokoya, *Journal of the Physical Society of Japan* **92**, 044801 (2023).
28. T. Matsushita, T. Muro, T. Yokoya, K. Terashima, Y. Kato, H. Matsui, N. Maejima, Y. Hashimoto, and F. Matsui, *Physica Status Solidi (b)* **257**, 2000117 (2020).
29. H. Oji, T. Murai, Y. Shibata, M. Tabuchi, Y. Watanabe, and Y. Takeda, *Journal of Surface Analysis* **26**, 228 (2020).
30. Y. Tsai, Y. Hashimoto, Z. Sun, T. Moriki, T. Tadamura, T. Nagata, P. Mazzolini, A. Parisini, M. Bosi, L. Seravalli, T. Matsushita, and Y. Yamashita, *Nano Letters* **24**, 3978 (2024).
31. A.F. Bhuiyan, Z. Feng, H. Huang, L. Meng, J. Hwang, and H. Zhao, *Journal of Vacuum Science & Technology A* **40**, 062704 (2022).
32. M. Hellwig, K. Xu, D. Barreca, A. Gasparotto, M. Winter, E. Tondello, R.A. Fischer, and A. Devi, *European Journal of Inorganic Chemistry* **2009**, 1110 (2009).
33. S.C. Ghosh, M.C. Biesinger, R.R. LaPierre, and P. Kruse, *Journal of Applied Physics* **101**, 114322 (2007).
34. A. Vanleenhove, I. Hoflijk, I. Vaesen, C. Zborowski, K. Artyushkova, and T. Conard, *Surface Science Spectra* **29**, 014014 (2022).
35. A.R. Chourasia, S.J. Hood, and D.R. Chopra, *Journal of Vacuum Science & Technology A* **14**, 699 (1996).
36. J.T. Gibbon, L. Jones, J.W. Roberts, M. Althobaiti, P.R. Chalker, I.Z. Mitrovic, and V.R. Dhanak, *AIP Advances* **8**, 065011 (2018).

37. A. Thompson, D. Attwood, E. Gullikson, M. Howells, K. J. Kim, J. Kirz, and H. Winick, *X-ray data booklet*, 2nd ed. (Lawrence Berkeley National Laboratory, University of California: Berkeley, California, 2001), Vol. 8, No. 4.
38. B. Ulgut and S. Suzer, *The Journal of Physical Chemistry B* **107**, 2939 (2003).
39. H.W. Nesbitt, G.M. Bancroft, R. Davidson, N.S. Mcintyre, and A.R. Pratt, *American Mineralogist* **89**, 878 (2004).
40. G. Silversmit, D. Depla, H. Poelman, G.B. Marin, and R. De Gryse, J*ournal of Electron Spectroscopy and Related Phenomena* **135**, 167 (2004).
41. Y.K. Chang, H.H. Hsieh, W.F. Pong, M.-H. Tsai, T.E. Dann, F.Z. Chien, P.K. Tseng, L.C. Chen, S.L. Wei, K.H. Chen, J.J. Wu, and Y.F. Chen, *Journal of Applied Physics* **86**, 5609 (1999).
42. D. Li, G. M. Bancroft, M. Kasrai, M. E. Fleet, R. A. Secco, X. H. Feng, K.H Tan, and B. X. Yang, *American Mineralogist* **79**, 622 (1994).
43. B. Ravel and M. Newville, *Journal of Synchrotron Radiation* **12**, 537 (2005).
44. B. Ravel and M. Newville, *Physica Scripta* **2005**, 1007 (2005).
45. L. Haddad, D. Gianolio, D.J. Dunstan, Y. Liu, C. Rankine, and A. Sapelkin, *Nanoscale* **16**, 5768 (2024).
46. Z. Chen, D.M. Chevrier, B.E. Conn, T.P. Bigioni, and P. Zhang, *The Journal of Physical Chemistry C* **127**, 20771 (2023).
47. K. Kobayashi, *Nuclear Instruments and Methods in Physics Research Section A: Accelerators, Spectrometers, Detectors and Associated Equipment* **547**, 98 (2005).
48. L. Zhang, N. Kuramoto, Y. Azuma, A. Kurokawa, and K. Fujii, *IEEE Transactions on Instrumentation and Measurement* **66**, 1297 (2016).
49. S. Tanuma, C.J. Powell, and D.R. Penn, *Surface and Interface Analysis* **43**, 689 (2011).
50. E.K. Salje and S. Kustov, *Physical Chemistry Chemical Physics* **25**, 1588 (2023).
51. M.D. Abramoff, P.J. Magalhães, and S.J. Ram, *Biophotonics international* **11**, 36 (2004).
52. W. Feng, X. Chen, Z. Lin, X. Lu, J. Liang, S. Yu, Z. Chen, G. Wang, and Y. Pei, *Physics Letters A* **511**, 129546 (2024).

Chapter 5 Conclusions and outlook

5.1 Summary of the important conclusions

In this doctoral thesis, the atomic structures and the chemical states of the dopants in Ga_2O_3 were investigated. For the Sn-doped β-Ga_2O_3, HAXPES, XANES, and EXAFS were used to clarify the atomic structure and the chemical state of the active Sn dopant sites. From HAXPES and XANES, the Sn dopant exhibited one chemical state, and it was attributed to the oxidation state. From the EXAFS and the XANES simulations, the chemical sate was due to Sn^{4+} state. The atomic structure of the Sn^{4+} oxidation state was attributed to the Octa Sn_{Ga} site. The Octa Sn_{Ga} site is attributed to the active dopant site for the Sn-doped β-Ga_2O_3(001).

For the Si-doped κ-Ga_2O_3, the chemical states and the atomic structures for the Si dopant were elucidated using PES, PEH, and EXAFS. From XPS and HAXPES, the Si dopant showed Si atom bonded with two O atoms. Since the experimental Si 2*p* PEH showed clear hologram patterns, the Si dopant should be located at the Ga atomic positions of the unit cell of κ-Ga_2O_3(001). The simulated PEHs were performed to clarify the occupation sites of Si dopants in the orthorhombic lattice. It was found that the simulated PEH of each inequivalent Si_{Ga} site could not explain the experimental Si 2*p* PEH. Thus, the Si dopant occupied all the inequivalent Si_{Ga} sites. Comparing to the previous studies, the active dopant site is attributed to the Si atom in the Tetra Si_{Ga} site in κ-Ga_2O_3, whereas the inactive dopant sites are attributed to the Si atoms in the Octa and Penta Si_{Ga} sites in κ-Ga_2O_3.

The results of the thesis might be useful for the improvement of Ga_2O_3-based devices. For example, the formation of high carrier concentrations in the source and the drain regions of Ga_2O_3-based MOSFETs is crucial to reducing contact resistance with metal electrodes. By using the results of the thesis, it may be possible to adjust the appropriate concentration of the dopants in the source and drain regions of Ga_2O_3-based MOSFETs. This means that the low contact resistance between Ga_2O_3 and metal in the source and the drain regions could be achieved. As a result, the performance of Ga_2O_3-based devices could be improved.

The present approaches may be applicable to the clarification of the atomic structure and the chemical states of the active and the inactive dopant sites of various semiconductor systems and will be essential for evaluating the properties of semiconductor dopants.

5.2 Outlook of the thesis

In the present thesis, the atomic structures and the chemical states of the active and inactive dopant states of Ga_2O_3 were clarified. The results of the present thesis may be applicable to the improvement of the properties of Ga_2O_3. For example, in the case of Sn-doped β-Ga_2O_3, oxygen vacancies are known as the unintentional donors, increasing the carrier concentration more than the Sn donor concentration. In this case, it may be difficult to adjust the desirable carrier concentration in Ga_2O_3-based MOSFETs due to the presence of oxygen vacancies. Therefore, when annealing the Sn-doped β-Ga_2O_3 crystal, the O_2 gas pressure should be increased to reduce the oxygen vacancies. In the case of Si-doped κ-Ga_2O_3, the Si dopant can be incorporated into not only an active dopant site but also inactive dopant sites. By optimizing depositing temperature, gas flow rate, and reaction gas pressure for the preparation of Si-doped κ-Ga_2O_3 layers, the number of inactive Si dopant sites may be reduced. As a result, κ-Ga_2O_3-based devices with high performance might be fabricated.

Acknowledgement

First of all, I want to express my sincere appreciation to my supervisor, Professor Yoshiyuki Yamashita. He provided me with valuable suggestions on my research topics and demonstrated patience and care towards me. There are not enough words to express my gratitude to him.

Next, I would like to express my sincere thanks to Professor Keiji Tanaka and Professor Kenji Kaneko. They gave me a lot of guidance and suggestions for my doctoral thesis as vice chairs in my thesis defense.

I would also thank the collaborators during my Ph.D. course; Dr. Jingmin Tang, Dr. Takahiro Nagata, Professor Tomohiro Matsushita (Nara Institute of Science and Technology & Japan Synchrotron Radiation Research Institute), Dr. Yusuke Hashimoto (Nara Institute of Science and Technology), Mr. ZeXu Sun (Nara Institute of Science and Technology), Mr. Takuya Moriki (Nara Institute of Science and Technology), Mr. Takashi Tadamura (Nara Institute of Science and Technology), Dr. Masaaki Kobata (Japan Atomic Energy Agency), Dr. Tatsuo Fukuda (Japan Atomic Energy Agency), Dr. Hajime Tanida (Japan Atomic Energy Agency), Dr. Toru Kobayashi (Japan Atomic Energy Agency), Dr. Masashi Nakatake (Aichi Synchrotron Radiation Center), Dr. Harue Sugiyama (Aichi Synchrotron Radiation Center), Dr. Hiroshi Oji (Aichi Synchrotron Radiation Center), Dr. Kohei Yamagami (Japan Synchrotron Radiation Research Institute), Professor Piero Mazzolini (Department of Mathematical Physical and Computer Sciences, University of Parma & Institute of Materials for Electronics and Magnetism (IMEM), National Research Council (CNR)), Professor Antonella Parisini (Department of Mathematical Physical and Computer Sciences, University of Parma), Dr. Matteo Bosi (IMEM, CNR), and Dr. Luca Seravalli (IMEM, CNR). They gave me a lot of help, guidance, and discussions in preparing the samples and performing the characterizations.

I would like to express my gratitude to all members of the Nano Electronics Device Materials Group and the 531 room in the MANA building of NIMS for providing a pleasant working environment. I am grateful to Ms. Michiyo Matsushita, who is the secretary of our group, for her patient and careful assistance with administrative and other private matters.

Finally, I would like to thank my family, especially my mother, father, and sisters, for their endless support, encouragement, and help throughout my studies and life.

In this doctoral study, the synchrotron radiation experiments were performed at BL22XU and BL25SU of SPring-8 with the approval of the Japan Synchrotron Radiation Research Institute (JASRI) (Proposal Nos. 2023B3742, 2023B3731, 2023B3732, and 2023A1221).